AN EXPLORATION IN MATERIALS DISCOVERY: DESIGN, CHARACTERIZATION, AND WORKFLOW OPTIMIZATION

A Dissertation Presented for the

Doctor of Philosophy

Degree

The University of Tennessee, Knoxville

Holland Hysmith Swicegood

May 2026

ACKNOWLEDGEMENTS

I would like to thank the University of Tennessee's Bredesen Center program for the opportunity to pursue my dream of becoming a scientist. I extend a great amount of gratitude to the many mentors who have helped shape me personally and professionally, none of this would be possible without your guidance along the way – Dr. Olga Ovchinnikova, Dr. Mahshid Ahmadi, Dr. Stephen Jesse, Dr. Neus Domingo, and Dr. Zhang Zhili. I appreciate the help and feedback received by the many staff members, post-docs, and fellow graduate students at both the University of Tennessee and Oak Ridge National Laboratory. The community built by these people inspire others to become the next generation of scientists that the world needs.

I also recognize the unwavering support of my husband, family, and friends throughout the process of my graduate school experience. I thank my parents, Jim and Lee Hysmith, for raising me to be outwardly curious about the world, encouraging my creativity, and supporting me throughout the rollercoaster of life. I thank my loving husband, Dallas Swicegood, who has stood by my side throughout this journey and has always reminded me of what I am capable of. I thank my brother, Parker Hysmith, for instilling confidence in me at a young age, so that I might consider pursuing something wild, like a PhD program. I thank my grandmothers, Mary Thompson and Mary Jane Hysmith, who have taught me to have pride in what I do, humility in how I act, and as a woman I can be anything I want to be. Lastly, I thank all my friends who have supported me throughout the journey with words of encouragement, support, and laughter.

ABSTRACT

Creating materials for a new wave of energy demands is met with many challenges. Huge strides have been made towards developing perovskites, tribofilms, and neuromorphic materials into commercial application. However, uncovering the roadblocks preventing their optimization is convoluted by their ability to evolve under observation. The need for improving workflows regarding their synthesis, characterization, and interpretation is required to fully understand the mechanisms that correlate to their functionality. In this work, the following principles for improving the avenue of materials discovery are as follows: synthesis and application equally relate to material functionality, materials are dynamic under measurement, and combining instrumental techniques impacts how material phenomena is observed.

Previous work in the role of ionic distribution of perovskites and additive inclusion in tribofilms reveals the importance of these principles. For the field of atomic force microscopy, it is proposed to develop a model that accurately depicts the shape of an AFM tip and simulate its interaction at the tip/surface junction of a material. Quantifying the electrostatic forces can reveal a better understanding of local effects such as Joule heating. In future work, the parameter space in which resistive switching occurs in neuromorphic materials can be defined with the aid of artificial intelligence.

TABLE OF CONTENTS

Introduction....1

Chapter One: Introduction to Energy Materials Discovery....4

1.1 Materials Discovery....4

1.1.1 Guiding Principles for Materials Discovery....4

1.1.2 The Motivation for Automation....9

1.1.3 Human-in-the-Loop....11

1.2 The Next Generation of Materials....14

1.2.1 Perovskite Solar Cells....15

1.2.2 Antiwear Tribofilms....17

1.2.3 Oxide Driven Memristors....19

1.3 Instruments for Nanoscale Characterization....22

1.3.1 Atomic Force Microscopy....22

1.3.2 Time-of-Flight Secondary Ionization Mass Spectrometry....33

Chapter Two: Developing Perovskites for Solar Cell Applications....35

2.1 Sample Preparation, Experiment Design, and Characterization Methods....35

2.2 Observing Chemistry Evolution with ToF-SIMS....39

2.3 Dynamic Light Induced Changes in Perovskites....40

2.4 Discussion: The Proposed Role of Potassium in Substrate Methods....44

2.5 Conclusion: Relationship to Principles....47

Chapter Three: Investigating Antiwear Tribofilm Formation....48

3.1 Synthesis of Antiwear Tribofilms as Evolving Dynamic Entities....48

3.1.1 Nano-IR Single Asperity Antiwear Tribofilm Preparation.....49
3.1.2 ToF-SIMS Single Asperity Antiwear Tribofilm Preparation.....50
3.1.3 ToF-SIMS Block-on-Ring Antiwear Tribofilm Preparation.....50
3.2 Characterization of Single Asperity Antiwear Tribofilms.....51
3.2.1 Nano-IR FFM of Single Asperity Prepared Films.....51
3.2.2 ToF-SIMS of Single Asperity Prepared Films.....52
3.2.3 ToF-SIMS of Block-on-Ring Antiwear Tribofilm.....54
3.3 Discussion: The Influence of Calcium Additives on Tribofilms.....54
3.4 Conclusion: Relationship to Principles.....55
Chapter Four: Neuromorphic Material Transformations.....57
4.1 Developing a Novel Method to Measure Conductivity Evolution in Memristor Materials.....57
4.2 Nanoscale Mechanical Measurements: Quantifying Forces on a Cantilever.....58
4.2.1 COMSOL Simulation of Free Cantilever Eigenmodes.....59
4.2.2 Simulation to Experiment: Comparing Shapes of Free Eigenmodes.....61
4.2.3 Eigenmodes in Contact.....65
4.3 Current Induced Joule Heating at the Nanoscale.....68
4.3.1 The Effect of Joule Heating on an AFM Tip.....69
4.3.2 Half-Resonance Band Excitation for Thermomechanical Measurements....73
4.3.3 Results and Discussion.....75
4.3.4 Nanoscale Thermomechanical Measurements on a Metallic Electrode.....76
4.3.5 Nanoscale Thermomechanical Measurements on a Diode-like Electrode...78

4.4 Nanoscale Conductivity Trends in Tantalum Oxide.....83

4.4.1 Results and Discussion.....84

Chapter Five: Recommendations for Future Material Pioneering.....88

References.....90

Appendix.....110

Vita.....152

LIST OF TABLES

Table 3.1 Summary of the Methods used for Antiwear Tribofilms.....125

Table 4.1 Comparing Contact Resonance Experimentally and through Modelling.....139

Table 4.2 Parameters for Schottky Barrier Physics Model.....147

LIST OF FIGURES

Figure 1.1 Scientific Reward System Workflow.....110

Figure 1.2 Perovskite Solar Cell Diagram.....111

Figure 1.3 Antiwear Tribofilms Diagram.....112

Figure 1.4 Memristor Oxide Diagram.....113

Figure 1.5 Atomic Force Microscope Instrumentation Diagram.....114

Figure 1.6 The Sader Method.....115

Figure 1.7 Eigenmodes & Simple Harmonic Oscillator.....116

Figure 1.8 Half-Resonance Band Excitation.....117

Figure 1.9 Forces Acting on the Cantilever.....118

Figure 1.10 ToF-SIMS Instrumentation Diagram.....119

Figure 2.1 X-Ray Diffraction of Perovskite Thin Films.....120

Figure 2.2 ToF-SIMS Depth Profiling of Pristine Thin Films.....121

Figure 2.3 ToF-SIMS Depth Profiling of Light Soaked Thin Films.....122

Figure 2.4 Isolated Ion Depth Profiles for Pristine and Light Soaked Films.....123

Figure 2.5 Conductive Atomic Force Microscopy of Perovskite Thin Films.....124

Figure 3.1 Experimental Methods for Antiwear Tribofilms.....126

Figure 3.2 Friction Force Microscopy of Antiwear Tribofilms.....127

Figure 3.3 AFM Nano-IR of Antiwear Tribofilms.....128

Figure 3.4 ToF-SIMS Positive Ion Chemical Imaging of Tribofilms.....129

Figure 3.5 ToF-SIMS Negative Ion Chemical Imaging of Tribofilms.....130

Figure 3.6 ToF-SIMS Depth Profiling of Single Asperity Tribofilms.....131

Figure 3.7 ToF-SIMS Depth Profiling of Block-on-Ring Tribofilms.....132
Figure 4.1 AFM Tip Model Built by SEM Images.....133
Figure 4.2 COMSOL Simulations of AFM Tip Model.....134
Figure 4.3 Eigenfrequency Study in COMSOL versus Experimentally.....135
Figure 4.4 Laser Position Study in COMSOL versus Experimentally.....136
Figure 4.5 Experimental Contact and Free Eigenfrequencies of AFM Tip.....137
Figure 4.6 Laser Position Dependence of Experimental AFM Tip in Contact.....138
Figure 4.7 Experimental Schematic of Memristors under HBE.....140
Figure 4.8 Concepts of Harmonics in AFM: DC, 1st, and 2nd 141
Figure 4.9 HBE Method Derived and Conceptualized.....142
Figure 4.10 Fast Fourier Transform Analysis of HBE.....143
Figure 4.11 AFM Data Plotting and Circuit Schematic for HBE Experiments.....144
Figure 4.12 Case I: Ohmic Contact.....145
Figure 4.13 Si-Ni Schottky Barrier Physics Model.....146
Figure 4.14 Case II: Schottky Barrier.....148
Figure 4.15 Schematic of Sample and Experimental Setup.....149
Figure 4.16 Case III: Memristor.....150
Figure 4.17 SEM Images of HBE AFM Tips.....151

INTRODUCTION

The future of energy materials is dependent on the workflows established to discover, understand, and optimize better solutions for years to come. This work explores the connections among material synthesis, nanoscale characterization, and interpretation of results and how they can be improved for material systems like perovskites,[1] tribofilms,[2] and memristors.[3] The subject areas of photovoltaics, friction-driven lubrication, and resistive switching materials have shown to operate reliably under difficult environmental conditions, while remaining cost effective and manufacturable at various scales.

On the other hand, these materials fall short of traits like stability, longevity, and efficiency in comparison to their less desirable counterparts, limiting their widespread commercialization. These limitations are rooted in the manner of which they are created, measured, and analyzed. Therefore, by coupling synthesis and characterization into a streamlined process, instead of sequential stages, materials discovery can be accelerated. Additionally, this creates the potential to bridge the gap between promising performance in a laboratory and large-scale industrialization.

Unique challenges are uncovered for all these material systems. For instance, perovskite solar cells are limited by their photovoltaic performance and environmental stability that is driven by interfacial chemistry and ion mobility.[4] Antiwear tribofilms are limited by their growth and evolution on the nanoscale, as well as their difficulty to be measured with one microscopy method alone to understand their structure, chemistry, and growth formation.[5] Lastly, memristors have resistive switching qualities that are dependent on local chemistry and conductive filaments that evolve under electrical and thermal stimuli.[3] Across all these materials, functionality is dependent on processes that

are local, dynamic, and sensitive to how the material is simulated and measured. By combining advanced instrumentation, targeted synthesis, and modeling techniques, these challenges can be addressed.

This work is structured to provide a comprehensive exploration of advanced materials discovery through a series of interconnected case studies and integrated instrumentation approaches. The first chapter will lay the foundation by introducing the guiding principles of materials discovery, emphasizing the intrinsic coupling between synthesis and application, the dynamic nature of materials under measurements, and the necessity of correlative characterization strategies that leverage multiple techniques to bridge length scales and capture essential phenomena. In the second chapter, the focus shifts to perovskite solar cells, where modified synthesis techniques are correlated with nanoscale characterization methods, such as time-of-flight secondary ion mass spectrometry (ToF-SIMS) and conductive atomic force microscopy (c-AFM), to identify the role of factors like potassium redistribution at the perovskite/tin oxide interface and the effects of light soaking on defect passivation and photovoltaic performance. For chapter three, an in-depth study of antiwear tribofilms the emerge dynamically at sliding interfaces is presented. Here, the integration of friction force microscopy (FFM), nano-infrared spectroscopy (Nano-IR), and ToF-SIMS reveals how lubricant additives, notably calcium, influence both the mechanical properties and chemical composition of the films, demonstrating the evolution of low-friction films under realistic operating conditions.

Lastly, chapter four addresses resistive switching in neuromorphic memristors by combining quantitative atomic force microscopy (AFM) techniques with robust finite

element modeling (FEM) of the AFM tip/surface junction. This chapter details how advanced harmonic excitation methods can isolate the second harmonic response, linked to Joule heating and electrostatics (i.e. capacitance, electrostriction), and providing new insights into the dynamic behaviors underpinning memristor performance. Recommendations for materials science discovery that pioneers' future research work is explored in chapter five. Collectively, this work constructs a cohesive narrative that not only advances understanding of individual material systems but also promotes an integrated workflow for accelerating materials discovery in energy applications.

CHAPTER ONE

INTRODUCTION TO ENERGY MATERIALS DISCOVERY

1.1 Materials Discovery

1.1.1 Guiding Principles for Materials Discovery

To improve how we approach materials discovery, moving beyond the cyclical nature of the scientific method is required. For example, materials created for energy applications must be efficient, affordable, long-lasting, and provide minimal environmental impact. To meet these criteria, scientists must consider the impact their work has beyond the laboratory. Considerations for materials discovery in this dissertation center on three tightly connected principles:

Principle One: There is an intrinsic coupling between synthesis and application, showing material functionality is equally derived from its synthesis and application. Therefore, a reverse design from application constraints back to synthesis is also possible.

Principle Two: Materials are dynamic. The dynamic nature of materials leads materials to evolve under operation and measurement.

Principle Three: Correlating complementary characterization techniques across scales is essential to deploy characterization strategies that bridge length scales, link local composition, structure, and functionality to provide a basis for automated discovery platforms.

Coupling synthesis and application emphasizes that material processing decisions are dependent upon the working environment and target performance. Material dynamics

stress that these systems evolve in time, often in response to the very fields, stresses, and probes used to study them. Correlative characterization highlights that no single instrument can capture the full picture, and that meaningful discovery requires linking structure, chemistry and function with spatial resolution appropriate to the phenomena of interest. Together, these three themes define the design space for the discovery workflows that the rest of this work seeks to optimize.

Firstly, synthesis and application must be treated as two sides of the same design problem rather than as separate stages. the way a material is synthesized influences how it behaves, yet the application of the material can require its synthesis to be "tuned" for a desired output. Instead of following a linear process where a material is processed and the results of its performance are recorded, reversing the sequence of steps is equally valid. For instance, if an environmental feature such as temperature plays a role in material functionality, its synthesis may be adjusted to withstand against a temperature range for longer periods of time. This is often seen in encapsulation of perovskite films to help withstand its longevity against high temperature and humidity.[6,7]

Applications of materials can reach beyond its environment into other spheres of science. For example, perovskites have expanded outside of the photovoltaic community into neuromorphic materials.[8,9] For perovskites to exhibit neuromorphic properties, mechanisms like defects and hysteresis are desirable for resistive switching, while they are typically avoided for solar cell use.[10] This implies that synthesis variables like substrate, additives, film thickness, annealing profiles, atmosphere should be planned and reported explicitly as "knobs" that map onto functional metrics such as power conversion

efficiency, friction coefficient, switching voltage, or retention time. In the context of this work, the perovskite, tribofilm, and memristor cases should therefore be framed as controlled explorations of how specific processing decisions shift a material's position in a multi-dimensional performance space.

In phosphorus based tribofilms, additives like calcium can help reduce friction in an environment by creating a more robust barrier. Yet, how the metal contacts create friction effects how well the tribofilm forms, building it through an atomic force microscope (AFM) tip or through a block-on-ring (BoR).[5] Environmental factors like temperature and humidity play a role as well. Finally, memristor materials are synthesized for resistive switching in neuromorphic computing, but their formation and rupture of conductive filaments is difficult to predict and therefore optimize.[3] The application used to study them to understand the behavior of these conductive filaments and how accurately the geometry can improve the parameter space in which they are studied.

Secondly, materials are not static systems and are typically modified by the characterization method used to measure them. They must be understood as dynamic entities whose structure, chemistry, and properties evolve during operation and even during measurements. Altering the material is required to induce chemical reactions and physical changes.[11,12,13] It is dangerous not to consider which mechanisms are dominated by instrumental interference when others are driven by the material itself. Developing reliable data interpretation methods to help differentiate these results is key to forming truthful scientific revelations. For example, tribofilm growth from continuous friction force applied via AFM induces the reduction of friction between two metal contacts

bonded by lubrication. Time-of-flight secondary ionization mass spectrometry (ToF-SIMS) sputters ions to observe ionic distribution spatially and through the depth of material. To this extent, sputtering through the material causes deformation due to ionic bombardment starting at the surface and along its depth profile. Additionally, the ion used for sputtering must be accounted for in the magnitude of ionic dispersion in the material.[14] If a cesium (Cs) ion beam is sputtering through a Cs-based perovskite film, Cs distribution is dependent on both the sputtering and chemical make-up of the material.

In perovskites, mobile ions migrate under illumination and electric fields, altering interfacial band alignment and defect densities over time; in tribofilms, sliding and thermal loads continuously rebuild and restructure the reaction layer; in oxide memristors, conductive filaments form, rupture, and reorganize with each switching cycle.[4,5,3] These processes mean that a single static measurement is often an incomplete or even misleading representation of the working material. Moreover, characterization itself via applied bias, mechanical contact, or high photon flux can drive additional evolution. Therefore, it is essential to design experiments that track material responses as a function of time, cycle number, or dose, and that treat the interplay between driving forces and microstructural change as a primary object of study. In the forthcoming cases, this translates into viewing light soaking, sliding wear tests, and repeated resistive switching not as nuisances to be minimized but as controlled perturbations that reveal the mechanisms governing stability and failure. Recognizing this dynamic character is essential for building workflows that can anticipate degradation pathways and inform more robust material and device design.

Thirdly, advancing materials discovery requires correlative characterization strategies that bridge length scales and link local composition, structure, and functional response. No single technique can capture, for instance, both the nanometer-scale distribution of ions at a buried interface and the device-level performance of a solar cell, or both the nanoscale friction behavior at a single asperity and the macroscopic wear rate in a component.[4,5] This motivates an integrated use of tools such as atomic force microscopy, nano-infrared spectroscopy, and time-of-flight secondary ion mass spectrometry, each contributing complementary information about topography, mechanical response, chemistry, and evolution under external stimuli. Moreover, the way instruments are utilized to measure a material affects the results of the experiment.

During observation of tribofilm formation, both the AFM Nano-Infrared (Nano-IR) and ToF-SIMS are used to measure chemical differences throughout the material, providing a uniqueness to each approach.[5] Both methods can measure the surface chemistry of the material but are deployed in a different manner. The Nano-IR observes chemical changes based on IR spectral excitation of the material.[15] On the other hand, the ToF-SIMS sputters with an ion beam to record the collection of ionic scattering from the material's surface.[16] Results from both surface techniques may show different observations due to the limitations of each tool and the changes the tool employs on the material. For studying the performance of perovskites, combining ToF-SIMS and conductive-AFM (c-AFM) can give insight to its chemistry profile, morphology, and conductivity.[4]

In understanding switching trends in memristors, joining finite element modeling (FEM) simulations in COMSOL to AFM experimental results can exhibit higher levels of understanding for comparing the dynamics of an AFM tip to the switching parameter space. Therefore, combining characterization techniques is ideal for forming a more cohesive study and results must be treated with their respective instrument to define material behavior.

In the framework of this dissertation, the perovskite case leverages structural probes and depth-resolved chemistry to explain performance trends; the tribofilm case combines friction mapping, vibrational fingerprints, and 3D chemical profiling to uncover how additives shape film growth; and the memristor case links realistic tip–cantilever modeling with harmonic AFM readouts to quantify nanoscale Joule heating and switching behavior. However, the power of these workflows lies not only in using multiple techniques, but in designing experiments and analyses so that measurements can be directly cross-compared and interpreted through shared models. Such correlative, workflow-centered approaches form the backbone of scalable, partially automated discovery platforms that can be generalized beyond the specific material systems studied here.

1.1.2 The Motivation for Automation

One aspect that led to the creation of the materials science field is that materials could be created, not just mined. Using sources of heat, light, material types and phases, and pressure all play a role in synthesis technique. Laboratories across the world are dedicated to material synthesis, and many are making steps to automate their

workflows.[17] Increasing utilization of machine learning (ML) has the capability to streamline certain synthesis pathways and provide opportunity to produce more materials with less human effort.[18] Additionally, artificial intelligence (AI) for automated synthesis is creating the ability to explore a vast parameter space, not confined to traditional synthesis workflows. Therefore, through automating both synthesis and characterization pathways, experiments can be created to explore material evolution as it occurs with live observations and feedback.

Automating material synthesis is met with many challenges. For instance, if using ML to select material components for perovskite synthesis, a robust model is needed for training.[19] While there are many elements that can be used in perovskite composition, there are limitations for which structures are possible. Contributions like human motor skills to the synthesis process can also create barriers for incorporation of robotics to make materials.[20] However, these techniques are already being applied to characterization techniques with much success. In areas such as microscopy, ML is a helpful tool to identify areas of interest in a material for further study. There are many strengths and weaknesses in incorporating this developing technology for material discovery. Development of ML and AI has inspired a recent emergence of self-driving laboratories (SDLs) for materials discovery.[21] SDLs use machine learning algorithms to automate experiments and reduce the occurrence of human error. These labs can interpret large datasets and indicate patterns that might be useful for future experimentation.[22,23] The benefit of AI-drive systems is that experimental parameters can be adjusted in real time, minimizing downtime between targeting new materials. There are many complex and

high-throughput experiments in the field of energy storage or nanotechnology. Identifying the right material for its application sooner rather than later is a significant benefit for the scientist.

On the other hand, there are many limitations to SDLs. Drawbacks to implementing SDLs into traditional lab spaces include high initial investment, difficulty automating human tasks, and rigid manufacturing of instruments.[24] Creating a space to conduct all experiments spanning from synthesis to characterization has many challenges. Large institutions have constructed SDLs with promises of future success, but many are skeptical if the benefits outweigh the drawbacks. Regardless, SDLs show the ability to collect large amounts of data, improve data reproducibility, reduce time-intensive tasks, and promote a safer laboratory environment.[25]

1.1.3 Human-in-the-Loop

Despite the nature of complicated workflows, scientists have traditionally been wholly responsible for the design and execution of material discovery. Scientists of different experience levels and research background collaborate on experiment design to ensure greater success. During the experimental phase, the need for human motor skills and logical thinking is crucial. Making informed decisions from scientific observations often involves a level of trial and error, problem-solving, and the reliance on a scientist's experience. Additionally, sharing and discussing results among others can help pivot the research in meaningful direction. Although computational tools are helpful, they cannot currently replace the human's ability to analyze data and draw conclusions moving forward.

Relying on human labor for most experiments slows down progress in research. Limitations like human error, variability in experimental techniques, and fatigue can affect the reproducibility of data. The inability of a researcher to perform multiple experimental tasks simultaneously also creates delays. Recent efforts to accelerate materials discovery have been aimed at pushing the limits of human led science by including non-human but capable and intelligent agents in the process. The first is to include automation in hardware platforms capable of physically executing experiments.[26,27] Second, is to create data management systems that optimize sharing data across different platforms and to train machine learning (ML) models.[28,29] Third, is to design workflows to run hardware that incorporates data, theory trained on physical laws to and incorporation of human expertise in the decision-making process.[26,27]

The materials discovery process typically begins with hypothesis formulation that is inspired from a conceptual idea. This hypothesis can offer multiple experiments that explore material properties and functionalities. Material synthesis and characterization are two common paths used for materials discovery. Seen in **Figure 1.1**, synthesis and characterization results can inform each other, and further provide a basis for creating theoretical models to help with future work in a positive feedback loop. Material laboratories have tools that can synthesize unique classes of materials through equipment like gloveboxes, wet-lab benches, pipettes, etc. Many material recipes can be revised through trial and error from synthesis and characterization instruments that help to image and quantify the material properties and functionality.[4,30]

After formation of the material, characterization can be used to aid in proving or disproving the initial hypothesis. Methods like atomic force microscopy (AFM), X-ray diffraction (XRD), and time-of-flight secondary ionization mass spectrometry (ToF-SIMS) can assess many structural and chemical properties.[31,32,33] For example, the ToF-SIMS enables the connection between compositional and functional properties, as well as the evolution in fields, environment, operation, and time. Real world applications can also be simulated by varying a number of parameters including temperature, humidity, and light excitation. Programming tools such as Python, MATLAB and COMSOL can be used for data interpretation and modeling material behavior for understanding performance and efficiency.[34,35]

Moreover, reinforcement learning (RL) is a type of machine learning that aims to remedy the lack of experience that an AI agent is likely to have by supplying training data through controlled simulations.[36] Real world scenarios offer complexity and reward functions that are not easily defined, making it difficult to directly develop an effective RL approach. Scientists must design reward functions that align with real-world goals, such as reducing climate change or developing a more cost-efficient design, but make them in such a way that a machine can use them. A key element driving RL is a reward function that is available to the algorithm during the training process.[37,38] As featured in Snapp et al.,[39] Bayesian optimization was effectively integrated into SDL environments. Yet, for many real-world problems, the reward functions aren't available until the end of the experiment and are typically motivated as long-term objectives.

1.2 The Next Generation of Materials

The workflow in which materials are researched is derived from centuries old methodology found in the scientific method – observation, hypothesis, experiment, data, and result.[40] Research fields are specialized to focus on certain aspects of materials science including its synthesis, characterization methods, and optimization of workflows used to produce materials. However, specialists of these fields must collaborate with one another and consider all steps in the material fabrication process to determine the impact of their findings. Following this design, many scientific breakthroughs have been achieved in the energy field: transmission lubrication, solar panels, and memristors, which will all be expanded upon throughout this work.[41,2,1,3, 42]

All materials are defined by their structure, processing, properties, and performance.[43] Furthermore, they are evaluated by the characterization in which we use to study them. Material applications in the field of energy science are becoming heavily scrutinized, given their potential contribution to our modern-day energy crisis. The need for cost efficient, sustainable, materials with long lifetimes is critical for the success in reducing our carbon footprint on the planet and powering future generations.

Despite the creation of innovative materials used in the current energy landscape, improvements are needed to achieve the longevity required for sustainable applications. For example, phosphorus-based lubricants are commonly used in car transmissions improve the lifespan of the vehicle. The growth of tribofilms, or lubricating friction barriers between the moving metal components, depends on the formulation of the lubricant, and therefore needs to be optimized for strong and long-lasting films.[44]

The invention of silicon solar cells is a novel discovery for transforming the sun into an electricity source. However, silicon requires costly manufacturing, high temperatures, and only has a lifespan of 15-20 years after panel installation, making solar energy an unpopular choice for many regions across the world.[45]

Lastly, the development of the memristor, or a device that changes its resistance state based on voltage passed through, was discovered as the missing component linking together the relationships of voltage, current, and resistance in a way that the other three basic circuit elements (the resistor, capacitor, and inductor) do not. Memristors have the potential to provide new options for including memory more directly and more energy efficiently into electronic systems and may be one way to realize neuromorphic components.[46] These three energy areas are prime examples of the importance of materials exploration and how the workflows through which we understand, fabricate, and produce can be improved.

1.2.1 Perovskite Solar Cells

Developed in the 1940's, perovskites are known for their photovoltaic properties and applications in solar energy.[47] Dieter Weber synthesized a class of Hybrid Organic Inorganic Perovskites (HOIP), demonstrating their ability to be fine-tuned to alter their electro-chemical reactions that drive energy conversion.[48] Alongside HOIP's, many different perovskite designs (2D, 3D, single crystal, thin film) and compositions have been created to become the next replacement for silicon solar cells.[49,50,51,52] As previously mentioned, silicon solar cells have their drawbacks that define a gap between clean

energy and affordability.[45] Therefore, the motivation for studying perovskites lie in their capability to efficiently create solar energy and be cheaper to implement.

Methylammonium lead iodide ($MAPbI_3$) gained popularity as one of the first perovskite solar cell materials.[53] Their structure follows a simple ABX_3 crystallographic format, featured in **Figure 1.2** located in the appendix where all figures and tables are listed, a cubic unit cell with the following: organic or inorganic cation (A), metal cation (B), and halogen anion (X). 2D perovskites follow a similar format but with the addition of an organic spacer cation to increase hydrophobic properties.[54] There are many ways to synthesize perovskites – thin films, bulk crystal growth, and tandem built with silicon cells.[55,56] There are strength and weaknesses for each method, yet perovskite thin films show promise for their versatility.

The drive for smaller and thinner electronics is growing, and perovskite thin films can be used as an efficient battery or computing chip. Thin films are created by recipes that dictate how each layer in the perovskite cell is dispersed onto the substrate. Hundreds of techniques include spin-coating, chemical bath deposition (CBD), inkjet printing, chemical vapor deposition (CVD), ligand-assisted reprecipitate (LARP), hot injection method, etc.[57,4,58,59] More commonly, perovskite films are produced via a two-step method: perovskite precursor deposition followed by an antisolvent. After deposition, the films are heated at an annealing temperature to initiate the crystallization process of the perovskite. There are many variables that can be fine-tuned in perovskite recipes inspiring hope that the right combination can provide the needed performance. This

promise coupled with adjustable bandgap attributes create a great avenue for making solar energy a much larger fraction of global energy production.

Although significant strides have been made for developing perovskites for commercial application, the highest reported efficiency in 2025 for a single-junction cell is only 27%.[60] There are many challenges for scaling perovskites from laboratory grade research to industrial installation. The nature of their organic components are sensitive to humidity and extreme temperature fluctuations, creating difficulty in weatherproofing them while keeping costs lower than silicon.[61,62] Additionally, due to the nature of their synthesis, defects can form that reduce power conversion efficiency (PCE).[63] There are many potential pathways to overcome these limitations, rooted in better understanding the nature and role of defects. For example, the distribution of ions throughout perovskite film interfaces can affect mechanisms like ion migration, recombination, and defect passivation. How ions are distribution before, during, and after operation as a photovoltaic, impact the overall performance. To further develop perovskites, understanding their behavior after they are synthesized is equally as important as to how they are synthesized. Like perovskites, tribofilms are another outlet that requires observation of their evolution, in addition to their composition.

1.2.2 Antiwear Tribofilms

While striving towards greener energy alternatives, efforts are being made to reduce the use of fossil fuels like gasoline, until better modes of transportation are implemented like electric vehicles (EV's) or hybrids. Antiwear (AW) tribofilms are designed in transmission fluids to increase the efficiency and lifetime of a vehicle.[64] Using effective

tribofilms can help automakers reach the goal of achieving a future of net-zero carbon emissions, until a better fuel replacement is discovered.[65] In 2007, David Philippon formed phosphorus based tribofilms via gas phase lubrication, which was later confirmed by De Barros-Bouchet to reduce the friction coefficient in transmission fluids.[66] Introducing tribofilms studies in transmission fluid synthesis will ultimately lead to a better product for the consumer and the environment.

The term tribofilm refers to the very thin and dynamic interface where the friction force mechanics of a lubricant interact with a solid surface. For a vehicle's transmission, lubricants are required in maintaining to prevent the many moving parts of the transmission from locking up or overheating during use. Tribofilms are developed by the force and thermal energy evolved when metal mechanical components move in contact with each other in the presence of lubricant additives. As these lubricants and additives are heated above a defined temperature threshold, shown in **Figure 1.3**[67], the products from reactions are deposited onto the metal, described as a thermal film. Over time, friction forces continue to interact with the thermal film in the presence of oxygen, evolving the thermal film into a tribofilm that creates a long-lasting lubricant barrier.[68] Compositions of tribofilms often have phosphorus-based AW additives, creating films with the following additives: iron phosphide, trimethyl phosphite, tributyl phosphate, and iron oxide.[66,69] However, tribofilms have been created with other AW agents as well like zinc dialkyldithiophosphate.[64,44]

To study the growth of tribofilms in real time, cross-correlated techniques are needed that measure its appearance, chemical composition, deterioration, and the impact of additives on friction forces. Understanding the formation of tribofilms can lead to improving their additive composition for reducing friction forces at the metal and lubricant interface. The need for observing how tribofilm effectiveness is correlated to additive chemistry is required to understand what changes are required to the synthesis of transmission lubricants.[5] Additionally, this ideology extends to other material classes like neuromorphic materials, that contain unique ionic properties not easily evaluated due to their volatility.

1.2.3 Oxide Driven Memristors

With the rise of big data in the computing industry, the traditional Von Neumann approach to computing begins to run into bottlenecks because the energy requirements for computing grows with the demand for computational resources. Our dramatically increasing need for compute power demands that we seek solutions to achieve similar levels of information processing but with dramatically higher efficiency.[70] High energy consumption in modern day computing is a growing problem, requiring a change in perspective of how it is designed. Insufficient data storage and increasing fabrication costs are limiting factors to implementing many technological breakthroughs.[71] In this regard, neuromorphic computing offers and alternative solution by processing and storing information in parallel.

A memristor illustrated in **Figure 1.4**, or “memory resistor”, can help fill the gaps current memory materials, devices, and architectures cannot fulfill by controlling

conductance using voltage, and also using voltage to read the state.[3,72,73] This makes for a potentially spatially and energy efficient memory device because fewer control/readout lines are needed and the memory state can be maintained without consuming electricity (i.e. it is non-volatile). Some memristor materials are used as resistive random access memory (RRAM) that can be continually switched between two states via external stimuli. RRAAM materials are promising for scalable, low-power, alternatives for computing memory.[74] Furthermore, the non-linear current-voltage relationship exhibited in memristors can match the non-linear transfer functions at the nodes in Artificial Neural Networks (ANN's). Therefore, ANN's which form the foundation of many artificial intelligence technologies may be realized more efficiently in memristive materials. Overall, neuromorphic computing is a promising avenue for a future of energy efficient computing.

RRAM materials switching is thought to be driven by two possible mechanisms – electrochemical metallization (cation migration) or valence charge memory (anion migration).[75] Both processes create conductive filaments that form and rupture, causing the effect of resistive switching.[76] In electrochemical metallization (ECM), migration of metallic cations derived from electrodes create conductive filaments (CF's), like silver (Ag) or copper (Cu). For example, a positive voltage is applied to the top electrode (Ag), where Ag atoms are oxidized to Ag^+. The silver cations then migrate across the material towards a counter electrode containing an inert metal (e.g. Pt or Au). The Ag^+ are then reduced to Ag atoms and deposit onto the counter electrode surface. CF's continue to grow in this process, creating a bridge between the cathode and anode.

Valence charge memory (VCM) operates in a similar manner but its CF's are formed by anions, or positive charged oxygen vacancies. A positive voltage applied to the top electrode causes O_2^- vacancies in the filament to migrate towards it and switching it to an ON state. After a negative voltage is applied, O_2^- ions then recombine with oxygen vacancies or oxidize the cation precipitates, allowing the device to switch to an OFF state. Two-terminal and three-terminal memristors are possible, two-terminal more commonly oriented for RRAM devices.[76] Different voltages are applied through each of the two electrodes that varies the conductance of the device emulating biological synapse functions. Three-terminal memristors create tunable channels between a source and a drain, the gate acting as a pre-synapse transferring stimuli to the insulator.

A memristor material which has shown potential for RRAM applications is tantalum pentoxide (Ta_2O_5) or commonly referred to as tantalum oxide (TaOx). TaOx has many desirable traits for its use as a memristor: synaptic capabilities, low power consumption, non-volatile at high temperatures, and enduring long cycling times.[77] TaOx operates under the VCM mechanism, claiming to survive up to 1×10^{10} cycles,[78] a maximum temperature of 800 K,[79] and can SET/RESET at 0.61 V/-0.49 V respectively.[80] In RRAM applications, TaOx forms conductive filaments that drive resistive switching. A drawback to optimizing filament formation in RRAM devices is that CF's cannot be easily tracked due to their random spawning locations and ability to stop functionality at any cycle.[46]

Due to their random nature, some CF's can continue to operate under cycling while others fail prematurely. Ultimately, once a saturation threshold is reached, the material can no longer function as a memristor. Many external stimuli can dominate resistive

switching in TaOx – voltage and heat, creating difficult in differentiating which is more effective for inducing RRAM.[81,82] Due to the complexity required for improving advanced materials like perovskites, tribofilms, and memristors, reaching conclusions and next steps takes time. Efforts to automate processes in the scientific method are desirable in hopes of expediting the use of advanced materials.

1.3 Instruments for Nanoscale Characterization

The instrumentation techniques that will be key elements in the material characterization workflows for this work are atomic force microscopy (AFM) and time-of-flight secondary ionization mass spectrometry (ToF-SIMS). AFM enables high resolution spatial mapping of functional properties on the nanoscale and can apply external stimulation to the material to measure local effects. On the other hand, ToF-SIMS provides a snapshot of ion distribution in materials both spatially and through its depth, covering the x, y, and z, dimensions, and can also apply excitation to the material during measurement. Together, these techniques can be coupled to provide a more wholistic viewpoint of material functionality.

1.3.1 Atomic Force Microscopy

The optical microscope, invented in the early 1600s, revolutionized our understanding of physics and especially nature at the micron scale. However, due to the diffraction limit of optical photons and other imperfections and aberrations in optical components, it is not possible to extend optical microscopy much below the micron scale. This made studying, interacting with, and understanding the world at the fundamental length-scale of matter, i.e. that atomic scale – which is 5 orders of magnitude smaller, much more difficult. One

class of microscopes, which was developed to address this shortcoming, is the scanning probe microscope (SPM), which resulted from asking the question, "What if instead of using optics to guide light to and from the surface of a material, a microscope used direct physical contact with a material? An atomic force microscope (AFM) was invented in 1985 to do just that, measure topography of a material through touch via a very sharp tip and force-sensing and feedback mechanisms.

The capabilities of the AFM would soon expand beyond this original scope, to create images on the scale of 10's of nanometers of not just the shape of a surface but also insights into the mechanical, electrical, magnetic and other important physical properties.[83] Illustrated in **Figure 1.5**, the basic components that make up an AFM are the following: cantilever, tip, laser, photodiode, and feedback detector that's connected to readout and control electronics. As the tip attached to the cantilever moves across the material surface, the laser reflects to the photodiode to track its movements in the X, Y, and Z direction. This general approach is often referred to as contact or tapping mode, dependent on what the feedback system is set to measure and control for: cantilever deflection, in the case of contact mode, and oscillation amplitude, in the case of tapping mode.[84]

Common applications of an AFM include visualizing structures on the nanoscale and therefore better understanding material properties. During measurements, a series of channels are typically recorded – topography (changes in height), deflection (change in the deflection angle of laser due to bending of the cantilever), amplitude (oscillation magnitude of the cantilever), and phase (relative change in timing between the oscillation

signal driving the cantilever and the response of the cantilever).[84] Before beginning an experiment, a procedure is implemented to calibrate the tip. The techniques used for calibration is not easily quantifiable but provides estimates for properties of the cantilever and the tip-surface junction. For example, a force-distance curve is taken estimate the relationship between the tip and surface contact during scanning, shown in **Figure 1.6**.[85] This point-based measurement observes the behavior of the tip approach and lift-off from the sample. First, the tip approaches the sample while attractive forces cause the lever to bend downward towards the surface. Next, attractive forces exceed the cantilever's spring constant, causing a snap into contact. Then, the lever and sample displacement continue to be reduced until a repulsive contact arises that pushes the tip up against the externally applied load. Then the direction of the tip-base motion is reversed. The tensile load becomes negative and pull-off forces snap the tip out of contact with the sample. As a result, the force-distance curve shows the lever and sample displacement as a function of force and distance.

Complementary to the force-distance curve, the Sader method is often used quantify the spring constant of the cantilever.[86] Cantilevers are made by a wide range of manufacturers that possess different qualities – tip coating, shape, stiffness, adhesion, and elasticity with certain cantilevers aimed at fulfilling specific purpose. For example, if setting up a conductive atomic force microscopy (c-AFM) experiment, an AFM tip with a conductive metal coating is typically required. During the evolution of scanning, the tip naturally changes shape and so sometimes selecting the appropriate cantilever is not straight forward.[87] When selecting a cantilever, it's important to consider the experiment

it is being used for and what factors, like spring constant, will impact the tip/surface interactions.[88] Therefore, despite manufacturers listing the average spring constant on AFM tip boxes, there is still variability from cantilever to cantilever. Featured in **Figure 1.6**, the Sader method considers the cantilever model (shape), resonant frequency in air, and quality factor in air to calculate the spring constant. During the calculation, optical lever sensitivity (inVOLS) can be estimate by measuring the magnitude of oscillation driven by random thermal motion. Since the driving force inherent to thermal vibration is easily estimated, one can subsequently estimate how the AFM's photodetector responds to cantilever bending (i.e., the sensitivity).[89]

Likewise, the alignment of the AFM's laser is important component to consider during calibration. As mentioned before, a laser is aligned along the AFM cantilever to track its movement during scanning. Ensuring that both normal and lateral deflection are calibrated it's pertinent to understand how the tip changes height and twisting motion across the surface.[90,91] Laser alignment is typically done through an optical microscope, with care given to the potential reflection of the AFM tip or sample surface, distorting the position of the laser point. After calibrating the AFM through measuring the spring constant, calculating the Sader method, and aligning the laser, quantitative measurements are still difficult capture due the geometry of the probe. In addition, the sensitivity that is measured using the Sader Method is only valid for the first "free mode" when the tip is far away from the surface. Therefore, it is difficult to extrapolate that information to higher free modes or contact modes of oscillation.

Traditionally, functional imaging via AFM oversimplifies or completely ignores the actual geometry of the AFM tip. This is critically important, especially in contact mode, since the properties of the tip-surface junction define the boundary conditions that govern the dynamics of the cantilever. Understanding the cantilever dynamics is crucial for interpreting what is occurring between the tip and material surface.

To create a mechanical oscillation in the cantilever during scanning, a driving signal composed of one or more frequencies are sent to the AFM cantilever. If the frequencies correspond with an eigenfrequency of the tip-cantilever system, then the cantilevers will oscillate with the shape of the corresponding eigen modes.[92] The eigen modes of a cantilever, seen in **Figure 1.7**, each correlate to a frequency range that excites the tip either at or above resonance. As higher eigenmodes are applied, more inflections points where the cantilever bends are present, impacting how the material is measured. Typically, measurements are conducted on or around the cantilever resonance for a better signal-to-noise ratio since the cantilever acts as a built-in amplifier, but there are drawbacks.[86] Overall, operating on resonance is useful for amplifying the measurable signal (laser beam deflection) as it transduces the vibration of the tip on a material surface.

Since the cantilever vibrates like a spring-mass damper system, a single eigenmode is well represented by the simple harmonic oscillator (SHO) model.[93] So, it is often reasonable to describe the behavior of a single oscillatory mode of the cantilever by the SHO where the fitting parameters are: amplitude (amplitude of the force/displacement driving the cantilever); resonance frequency (center of the resonance peak); the quality

factor (or Q-factor) of the cantilever which is inversely proportional to the width of the resonance peak and directly proportional to the mechanical amplification afforded by operating on resonance, and phase (the phase lag between driving and response signals).[86]

The AFM cantilever has multiple eigenmodes that can be investigated in a practical laboratory setting. For a single AFM cantilever, the shape and eigen or resonant frequencies of these modes can vary substantially depending on the mechanics of the tip-surface junction.[92] If the cantilever is far away from the sample and the tip does not experience any interaction with the surface, then it is one of its "free modes". It is usually possible to access the first three vertical (bending) free modes and the first two torsional (twisting) free modes.[86,94] From modeling, one can see that there are also lateral bending modes, but these are usually not detectable as they do not affect the angle of the reflected laser beam from the cantilever.[86]

As the tip is brought into contact, the interaction of the tip with the surface will change the eigenmodes and frequencies of the cantilever. This is easily understood if we consider the tip-surface junction to be composed of linear springs which generate force proportional to displacement from an equilibrium position. As we approach the surface, the effective spring constant of the junction increases which reduces the displacement of the end of the cantilever (thus changing the mode shape) and results in an overall stiffening of the system and, thus, an increase in resonant frequencies.[86] The surface may also introduce damping and energy dissipation which reduces the Q-factor of the resonances.[95] These trends hold true for vertical and torsional modes. Notably, the lateral bending mode, which is not easily detected away from the surface, can, because of

pinning of the tip, result in beam twisting and therefore show up as a torsional response.[86] This sea of changing resonance can be complicated, but importantly, offer multiple windows into nanoscale forces and dynamics.

One can also use a clever combination of driving frequencies to investigate a range of couplings and non-linearities of nanoscale forces and dynamics. One notable example is examining multiple harmonics. Here, one can measure and amplify the first (primary) harmonic of a response by driving and measuring at the resonance frequency of a mode. However, to amplify the second (or higher) harmonic response, one can't simply expect the second harmonic to align with a cantilever resonance. So, to overcome this, one can shift the drive frequency to *half* (or other fraction) the resonance frequency of the cantilever.[96] In this case, the second harmonic will then align with the resonance and experience the sample amplification as the first harmonic. Using this approach, one can systematically and reliably measure and amplify the harmonic components of a response. Higher harmonics response is particularly important for the studies here where a significant component of tip-surface interaction force is relevant in the 2nd harmonic. This is true for electrostatic interactions where the electrostatic forces go as the square of the driving voltage and in Joule heating where the heat generation goes as the square of the current passing through the tip-surface junction.[97] This "quadratic effect" can generate forces at zero frequency (DC forces), at the first harmonic, and at the second harmonic.

Given the complexity of a material's surface, the tip-surface junction can change substantially from one location to the next causing the resonance frequency to shift. This can give useful insights into studying the mechanical properties of materials, but this is

only true if the resonance can be properly tracked. Traditional AFM relies on the lock-in amplifier to efficiently, quickly, and reliably measure the amplitude and phase of a response at a specified frequency.[98] The lock-in is excellent at providing good signal to noise in measurements, if one is off-resonance or if one can guarantee that the resonance will not shift. If it does shift, then various properties of the resonance (the amplitude, resonance, Q-factor, and phase) convolute. One method to combat this is to implement a phase-locked loop alongside the lock-in to feedback on the phase signal to shift the drive frequency so that it follows the resonant frequency.[98] This is often used in non-contact or tapping modes AFM where the variations in stiffness (and hence resonance frequency) are relatively small and slow thus allowing the feedback loop to adjust properly.

However, in the investigation here, the AFM is used primarily in contact mode where the frequencies shifts and phase changes (especially in piezo-response force microscopy) can be very abrupt thus making phase-locked-looped approaches infeasible. One fix that has been implemented to address some of these issues is the Dual AC Resonance Tracking (DART) method.[99] The DART method utilizes two parallel lock-in operating at slightly different frequencies with the goal to set the frequencies to operate on both sides of the resonant frequency equally spaced from that central point. A feedback loop is set up to adjust the drive frequencies of the two lock-ins so that the amplitudes of the responses at those frequencies match. If the amplitudes match, then one can safely assume that the resonant frequency is exactly between the two drive frequencies. If one amplitude is larger than another, then the drive frequencies are adjusted until they match. This overcomes all reliance on phase, but does still require an active feed-back loop

(which can ail under large frequency shifts). Furthermore, one is never driving the system on the resonant peak (only on either side) and therefore doesn't receive the full benefit of resonant amplification.[99]

An alternative method, and the one adopted in the studies here, is an open-loop method (meaning it does not use a feedback loop to track anything) that drives and measure at many frequencies simultaneously. This band excitation (BE) AFM technique works by the user defining a center and width for the equally spaced frequencies of the band in the Fourier domain.[100] This Fourier representation of the signal is then converted into a signal in the time-domain. An arbitrary waveform generator is used to create the signal as a voltage varying over time. The signal is sent to the AFM cantilever as a "chirp" which drives oscillations in the cantilever. The response is measured simultaneously and compared to the drive signal to recover the transfer function of the cantilever, which is the resonance peak. The nonlinearities between the tip-surface interactions produce higher harmonic signals as mentioned previously.

The BE method can be altered to make it sensitive to the harmonics as well. This extension, which will be named half-resonance band excitation (HBE) in this work, is designed to project the second harmonic signal to match up with a resonance to amplify and observe mechanisms like Joule heating.[96] HBE operates via a two-fold approach, shown in **Figure 1.8** – (1) centering the band of excited frequencies on a resonance and measuring the response at that resonance, and (2) halving the frequencies of the original excitation band so that so that the second harmonic of the response falls on the cantilever

resonance and is amplified as well. These two signals are sent sequentially in time and their responses are analyzed separately as well.[96]

A few techniques commonly used in the AFM for materials characterization are piezo force microscopy (PFM),[101] Nano-infrared spectroscopy (Nano-IR),[15] and conductive-atomic force microscopy (c-AFM).[32] Besides being used in conjunction with BE, PFM is a technique implemented for understanding the material's polarization direction, useful for materials that can hold charge like ferroelectrics. The sign (positive or negative) of the voltage sent to the tip determines the dipole orientation of the tip contacting material surface, which will result in the material's dipole orientation to be measured as opposite. Therefore, the AFM can act as a tool for switching polarization in materials to study a wide variety of mechanisms like ferroelectric domains and ionic mobility.[101] Nano-IR is another technique that can unveil the changes in surface chemistry throughout scanning. This method works through exciting the material surface with user determined IR-bands to assign IR signatures to topographical regions, correlating ionic bonds with surface morphology.[15] Lastly, c-AFM measures a material's conductivity through grounding the AFM tip and sending voltage to the sample during measurements.[32]

When considering the AFM tip, a variety of forces are interacting on the cantilever mechanics and dynamics – mechanical forces, electrostatic forces, and chemical forces, to name a few. Short range and long range forces act on the AFM tip that impact its movement. Van der waals, repulsive and adhesion forces (i.e. electrostatic) and chemical interactions all dominate close to the tip-surface junction.[102,103] Van der waals forces are responsible for intermolecular forces between molecules that impact their polarity. The

AFM tip is a charged source contacting a material's surface and can switch polarization orientation in experimental setups like piezo-response force microscopy. As mentioned in the force-distance curves, close-up electrostatics cause a "push-and-pull" effect of the tip as it scans across the material's surface. Chemical interactions between a material and AFM tip are possible too.

For example, organic materials like perovskites are susceptible to interactions with certain metal coatings that can cause movement of ions and surface charges led by the tip. Long-range interactions like mechanical and capillary forces are equally as important, as they consider the movement of the tip attached to the cantilever.[104,105] Oscillation of the tip in tapping mode or lift-off in two-pass kelvin probe microscopy (KPFM) are examples of mechanical forces that influence how the tip moves across a sample surface.[106] Capillary forces refer to the formation of the water meniscus that occurs on the tip contact that changes shape dependent on sample and environment.

When bias is applied to the cantilever during measurements, forces occur at the tip-surface junction and elsewhere, demonstrated in **Figure 1.9**. For example, if the tip-surface junction can be visualized as a stack of parallel plates, electrostatic forces are often derived from this area. Electrostatics are produced by AC bias because electrostatics forces are generated by a difference in bias between each parallel plate.[107,106] The magnitude of these forces is scaled by the capacitance gradient (dC/dz). Additionally, forces can cause the cantilever to bend, changing its deflection. Similar forces can act on the sides of the cone-like shape of the tip, pushing the tip into the material surface. Bias acting on the conductive cantilever can cause the cantilever to

behave as if there is a surface displacement.[104] However, there is a need to mitigate these effects, and therefore a major part of this work will introduce the following: creating a detailed geometric model that replicates the mechanical and dynamic behavior of an AFM tip, refining this model through experimental measurements, and modeling electrostatic forces on the cantilever to determine its response due to just electrostatics and displacement.

1.3.2 Time-of-Flight Secondary Ionization Mass Spectrometry

The introduction of mass spectrometry (MS) allowed for the observation of a material's mass to charge ratio, or guide to a material's elemental proportions. A mass analyzer, ion source, and detector work together to remove the surface ions from a sample, and therefore detect the number of ions with respect to their composition present on the surface. By knowing ion counts, one can have a better idea of the materials' composition.[108] Secondary ionization mass spectrometry (SIMS) was invented later with the capability to detect even lower counts of ions through detecting secondary ionization emission.[109] The concept of time-of-flight (ToF), featured in **Figure 1.10**, rounds out the invention of the ToF-SIMS by measuring the time for travel of secondary ions across a set distance. The ToF-SIMS can work at a high resolution and sensitivity to detect chemistry in the XY and Z direction of a material.[110]

By pulsing ions like bismuth, cesium, and oxygen, the ToF-SIMS can remove secondary ions from a material surface to accelerate them in a flight tube were mass is determined. This can result in analysis through two modes: chemical imaging and depth profiling. Chemical imaging observes the spatial resolution of ions in the XY direction by

creating a map that showcases concentration of respective ion counts.[15] Depth profiling sputters through the material surface, measuring the ionic distribution in the XZ direction, providing an image of the ionic map with each material layer.[4] For each ToF-SIMS method, consideration is given to the type of pulsing ion used and excitation energy since they directly affect both the image resolution and material integrity.

CHAPTER TWO

DEVELOPING PEROVSKITES FOR SOLAR CELL APPLICATIONS

Hybrid perovskite solar cells have rapidly emerged as a leading candidate for the next generation of photovoltaics. However, their performance and stability remain strongly constrained by how they are synthesized and how their interfaces are engineered. This chapter investigates perovskite films as a model system for understanding the tight coupling between processing routes, interfacial chemistry, and functional response at the nanoscale. Focusing on variations in the electron transport layer (ETL) and its associated processing, such as different tin oxide deposition methods, the work examines how these choices control micro-strain, crystallite size, and defect landscapes in the perovskite stack. By combining X-ray diffraction, depth-resolved chemical analysis, and local current mapping, the chapter builds a coherent picture of how specific interfacial ion distributions, especially of potassium, correlate with reduced recombination and enhanced power conversion efficiency. In doing so, it demonstrates how correlative nanoscale characterization can be used not only to explain device behavior, but also to inform synthesis strategies that more directly target stable, high-performing solar cells.

2.1 Sample Preparation, Experiment Design, and Characterization Methods

A series of metal-halide perovskites (MHPs) are synthesized to better understand the influence of substrate processing methods on solar cell performance.[4] The composition of each film has the following layers: glass, fluorine-doped tin oxide (FTO), tin oxide (SnO_2), potassium chloride (KCl), and formamidinium lead iodide-methylammonium lead bromide $(FAPbI_3)_{0.97}(MAPbBr_3)_{0.03}$. The perovskite layer is spin coated onto the

substrate (SnO_2) acting as the electron transport layer (ETL) in the film, prepared with the following four methods: chemical bath deposition (CBD), nanoparticles, and two hybrid approaches of CBD and nanoparticles reacted to produce different SnO_2 thicknesses. KCl was deposited on the substrate before the perovskite layer to help reduce defect formation at the perovskite/SnO_2 interface.[111] Films are therefore notated throughout his work via their substrate processing technique: film A (CBD), film B (hybrid, 70-80 nm thickness), film C (130 nm thickness), and film D (nanoparticles). The timescale for which nanoparticles are reacted with the film during substrate synthesis is different, 4 hours for film B and 12 hours for film C. In comparison, SnO_2 thickness for films A and D is 30-60 nm.

Power conversion efficiency (PCE) is calculated via J-V curves for each of the films to help quantify the performance of their photovoltaic properties. J-V curves are measured to determine the order of PCE from highest to lowest: B, C, D, and A. It should be noted that films A and D have similar I-V behavior, likely due to their similar morphology and makeup, contrasting what is observed in films B and C.

The connection between substrate processing and defect formation in SnO_2 if further investigated through measuring strain behavior on bare substrates, via X-ray diffraction (XRD) patterns. Featured in **Figure 2.1**, each peak profile is plotted with the same peak locations and broadening behavior among all the films. A Williamson-Hall (W-H) plot analysis is conducted to quantify the micro-strain behavior in the substrates with their respective crystallite sizes.[112] The W-H method is an analysis technique used for XRD

data to separate peak broadening effects from crystallite size and lattice strain. The following equation is used to plot this model:

$$\beta_{hkl}cos\theta = \frac{K\lambda}{D} + (4sin\theta \times \varepsilon) \quad (2.1)$$

Where the variables are the following:

β_{hkl} = Full width half maximum (FWHM)

θ = Bragg angle

λ = wavelength of X-ray radiation

K = shape factor

D = crystallite size

ε = microstrain

The following constant were assumed from the experimental setup:

k = 0.94

λ = 1.5406

Firstly, the Bragg angle and full width half maximum (FWHM) is acquired for each peak from the XRD data. Using these values, points are plotted from the Williamson-Hall equation calculating the y-axis ($\beta_{hkl}cos\theta$) and x-axis ($4sin\theta$). After a line of best fit is drawn through these points, the y-intercept can be extracted, and the crystallite size can be solved for. The slope of this line can also be calculated, solving for the microstrain. The W-H calculation is ideal for materials that have small crystallite sizes (< 10 nm) and therefore is used for this study since the average SnO_2 nanoparticles size is between 3-5 nm. The limitations to using the Williamson-Hall method on XRD of thin films is that it provides a linear fit. For a case where a linear fit is not optimal, this analysis is not

recommended. XRD data trends where this method is not useful would be when the peak shapes are mixed (neither purely Gaussian or Lorentzian), or when crystallite size and strain vary irregularly with the Bragg angle. Anisotropic crystalline structures or extremely large grain sizes would also not be ideal for this method.

Both XRD and W-H plot analysis identify the SnO_2 substrate from film B methods to have the lowest micro-strain at 2.98 x 10^{-3} and average crystallite size of 16.06 nm. Film C, also prepared with hybrid substrate methods to produce a layer thicker than B, has the second lowest micro-strain at 3.35 x 10^{-3} and average crystallite size of 17.86 nm. Therefore, films with smaller crystallite sizes in the hybrid prepared SnO_2 layer can reduce lattice spacing of the *hkl* planes and contribute to less defect formation at the perovskite/substrate interface. Fewer pinholes and better uniformity throughout the film is possible with both B and C films. External stress causing mis-matched alignment from the micro-strain in the SnO_2 layer can create residual tensile strain in the perovskite layer, weakening overall lattice integrity.[113] With film B having the highest PCE performance, the correlation of lower strain can allow greater distribution of ions (like potassium, K^+) at the perovskite/substrate interface to assume the position at defect sites. This is further explored during the time-of-flight secondary ionization (ToF-SIMS) measurements mentioned later.

Furthermore, radial distribution function (RDF) models are constructed to observe how lattice spacing between ions in the perovskite layers of the films change with respect to different compositions and environmental factors like tensile strain.[114] The results of the RDF models highlight decreased distances between cations and anions in the

$MAPbBr_3$-$FAPbI_3$ perovskite composition, in comparison to their standalone composition counterparts (i.e. $MAPbBr_3$, and $FAPbI_3$). This decreased distance can lead to better electronic structure and ion mobility pathways in the hybrid perovskite formulation.[115] Therefore, exploring how the chemistry changes across all surfaces in the film can show how ion distribution changes with respect to all substrate processing methods.

2.2 Observing Chemistry Evolution with ToF-SIMS

Time-of flight secondary ionization mass spectrometry (ToF-SIMS) is used to chemically capture the effects of substrate processing methods on each of the films. Depth profiling, a method in which ion beam sputtering "mills" through layers of a sample, provides ion count information from mass spectra as a function of z-direction. By pursuing this method, demonstrated in **Figure 2.2**, we can observe the changes in chemistry with respect to each interface among the different substrates. We identify the perovskite/substrate interface in ToF-SIMS depth profiles where tin (Sn^+) surpasses lead (Pb^+) in counts intensity. To help with the spatial complexity of the data, we further defined these interfacial regions through non-negative matrix factorization (NMF) analysis using four components: (1) perovskite surface, (2) perovskite layer, (3) perovskite/KCl interface, and (4) KCl/SnO_2 interface. The equation used for NMF analysis of the ToF-SIMS data, seen in **Figure 2.2**(f), is defined as follows: "x", the fraction of individual ions, "m", individual ion mass, and "z", the cross section of the film surface through the depth profile. One-dimensional maps plotted as a function of depth are extracted from this calculation that correspond to NMF endmembers. These endmembers are ions that are featured with the highest intensity counts at each interface.

Depth profiling experiments track both positive and negative ion distribution, featuring ions with high counts such as lead (Pb^+), tin (Sn^+), and potassium (K^+). Films B and C, with the hybrid substrate processing approach, show a strong presence of potassium (K^+) ions in the perovskite/SnO_2 interface. In film B, the potassium (K^+) intensity surpasses that of lead (Pb^+) and tin (Sn^+) at the interface. As seen in films A and D, where exclusive methods of either CBD or nanoparticles are used to form the substrate, such a phenomena does not occur at the interface. Considering SnO_2 is acting as the electron transport layer (ETL) in this system, seeing the migration of potassium (K^+) at this site is particularly interesting, originating from the potassium chloride (KCl) processing step before perovskite layer deposition. Greater distribution of potassium (K^+) in hybrid films B and C could indicate higher diffusion capabilities and the ability to passivate defects at this interface, corresponding to the reduction in micro-strain behavior as seen in the W-H analysis. However, further investigation in the distribution of other ions needs to be explored. It is important to consider that film B has greater potassium (K^+) mobility at this interface compared to film C, likely due to the SnO_2 layer being ~80 nm thinner for film B.

2.3 Dynamic Light Induced Changes in Perovskites

Another ToF-SIMS analysis is conducted, in **Figure 2.3**, to observe the stability these films and how their ion distribution changes after light soaking. The process of light soaking involves exposing perovskite films to illumination for long periods of time before using them for photovoltaic applications. Depending on the intensity of light and time in which the film is exposed can be equivalent to the number of suns the film is

exposed to. For example, the light-soaked films in this study were exposed to 120 suns. The utilization of light soaking can initially enhance efficiency, however it reduces the film's optoelectronic stability and long-term reliability. The latter factors accelerating aging in the perovskite films.[116] For this work, pristine and light soaked films for all substrate processing methods were explored to reveal if the mechanisms observed in pristine films are present in light-soaked films, and if the light soaking process had an impact on the trends that are noticed.

Films B and C show a similar trend with potassium (K^+) distribution at the perovskite/SnO_2 interface, potassium again surpassing the lead (Pb^+) and tin (Sn^+) interface in film B, highlighted in **Figure 2.3**b and **Figure 2.3**c. A similar magnitude of ion counts is observed for prominent ions like lead (Pb^+), tin (Sn^+), and potassium (K^+) after sun exposure, demonstrating stability of the film during operation and withstanding ionic mechanisms that have been observed. After exposure to light soaking, potassium (K^+) distribution is now observed at the perovskite/SnO_2 interface for film D, its substrate formed with nanoparticles. Therefore, nanoparticle preparation may allow for greater potassium (K^+) diffusion, since this is not observed in film A, where its substrate is formed with only the chemical bath method (CBD).

Other ions with smaller counts like sodium (Na^+), calcium (Ca^+), formamidinium (FA^+), and methylammonium (MA^+) are also observed in these films. In **Figure 2.4**, individual ions are plotted separately to adequately observe their distribution among the different films, due to the stark differences in ion count intensity when plotted altogether. Migration of ions like sodium (Na^+) and calcium (Ca^+) is seen throughout films B and D,

likely originating from the soda lime glass (SLG) layer. Previous work has demonstrated the capability of Na^+ and Ca^+ passivating defects in perovskites and resisting illumination degradation respectively. However, caution is used to make assumptions of these roles in this system, considering their low ion counts. Therefore, the role of potassium (K^+) ions aiding to passivate defects at the perovskite/SnO_2 interface is still considered the primary mechanism to changes seen in both strain and power conversion efficiency (PCE) among the films.

Greater distribution of formamidinium (FA^+) is seen near the perovskite surface, while methylammonium (MA^+) has more distribution closer to the SnO_2 layer in the light soaked films. This ionic disparity could contribute to the differences in potassium (K^+) distribution in these films due to ionic radius. Methylammonium (MA^+) has a smaller ionic radius compared to formamidinium (FA^+), allowing more sites for K^+ to distribute within the perovskite layer. Both lead (Pb+) and tin (Sn+) have maintained their consistent distribution profiles before and after light soaking, making it a reliable marker for the transition of the perovskite layer into the SnO_2 layer.

When observing chloride (Cl^-) in negative ion mode, its distribution is seen at the perovskite/SnO2 interface as expected, yet does not follow a similar trend compared to potassium (K^+) after light soaking. This further reinforces the role of potassium (K^+) compared to chloride (Cl^-) in this mechanism, originating from the potassium chloride (KCl) layer. Similar counts are observed in negative ions like bromide (Br^-), iodide (I^-), SnO^-, and I_2^-, with no substantial changes before and after light soaking. Therefore, it seems only positive ion distribution influence the substrate processing technique in these

films. All these observations coincide with previous reports, indicating that passivation ions can reduce defects without the need to change the electron transport layer (ETL) composition. This opens possibilities to use more cost-effect and sustainable methods to synthesis thin film substrates.

Investigating changes in conductivity behavior before and after light soaking can further reveal if passivating defects at the perovskite/SnO_2 interface can produce higher current in the hybrid films. Conductive-atomic force microscopy (c-AFM) experiments are performed to compare the morphology and spatial distribution of both photocurrent and dark current in these films. Seen in **Figure 2.5**, These experiments are measured under illumination and dark conditions, while measuring current simultaneously. For illumination conditions, a white LED light source is positioned above the film. Topography is measured simultaneously with current, to compare the film morphology to the current response.

c-AFM results reveal that the morphology is similar among all films, regardless of their substrate processing methods. In films prior to light soaking, a higher current is observed when illuminated, in comparison to dark conditions as expected. Higher current is seen within the grains, versus at the grain boundaries. Lower current at defect sites like grain boundaries is typical, some speculating that grain boundaries can function as a recombination site. Yet, this theory is still highly debated, and out of scope for this study. Orientation of crystallographic grains can cause inter-heterogeneity in the morphology of perovskites, reflecting the inhomogeneous current response seen within the grains across

all films. Likewise, distribution of potassium at defect sites across the perovskite/SnO_2 interface can also contribute to this inhomogeneity in current.

Overall, a higher magnitude of current is observed for hybrid films B and C in both light and dark illumination conditions. This correlates well to the PCE behavior previously discussed, in which film B is the highest performing solar cell in the series. Film B produces photocurrent up to 300 pA and up to 120 pA in dark conditions. After exposure to light soaking, films B and C still demonstrate higher magnitudes of current. Light soaked film C shows the greatest the increase in production of current, producing up to 500 pA under light and 90 pA under dark illumination conditions. These results indicate that hybrid films are less susceptible to breakdown under illumination conditions, at the the perovskite/SnO_2 interface. As one may recall, films B and C have lower micro-strain, allowing for greater distribution of potassium (K^+) to passivate defects acting as recombination sites shown in the ToF-SIMS analysis, increasing overall current production.

2.4 Discussion: The Proposed Role of Potassium & Substrate Methods

Recalling the previous considerations of materials discovery for this case, impacts of synthesis, material dynamics, and characterization techniques all serve a purpose. Ion migration, or the movement of ions through the crystal lattice, is triggered by external stimuli like light or an electric field in perovskites. Ion migration can harm the performance of perovskites due to many reasons. The mechanism of ion migration is impacted by the lattice structure and defects like vacancies and grain boundaries.[117] Therefore, the inclusion of an electron transport layer like tin oxide in this system,

reduces ion migration at the perovskite interface by reducing the accumulation of halide migration that can lead to insulating layers causing chemical degradation.[118]

The addition of additives like potassium chloride (KCl) between the perovskite and electron transport layer (ETL) enhances compressive strain, which tightens the crystal lattice at the perovskite/ETL interface, making it more difficult for ion migration to occur. Introducing KCl leads to the formation of alkali metal defects (i.e. K^+) at interstitial positions. This presence of K^+ at these sites leads to a compressive surface strain, reducing tensile strain that causes degradation. When KCl is applied to a perovskite/tin oxide interface, the presence of KCl strengthens that interface, promoting better crystal growth resulting in a more uniform interfacial layer that reduces the number of interfacial defects generated. As seen in the ToF-SIMS results, hybrid films have greater potassium distribution at the perovskite/tin oxide interface that originates from the KCl layer. Therefore, hybrid films likely have more potassium at interstitial positions at this interface, increasing compressive strain, in agreement with XRD results that state they have less microstrain. All these attributes allow for less ion migration to occur in the hybrid films.[119]

Smaller microstrain is indicative of less non-uniform stress or distortion in the crystal lattice, reducing the amount of ion migration channels. Therefore, tin oxide films prepared with both CBD and nanoparticles exhibit lower microstrain than their counterparts that helps reduce the impact of ion migration in the perovskite film. For the hybrid films, lower microstrain also results in smaller crystallite size due to the W-H method extracting microstrain from slope and crystallite size from the y-intercept.

Typically, larger crystallite size allows for less ion migration due to less grain boundaries present in a film. However, in these films, smaller microstrain indicates better lattice alignment at the perovskite/substrate interface. Therefore, the strain information extracted from this model tells us its relation to reducing ion migration and the crystallite size simply provides information on the tin oxide morphology. Additionally, hybrid films exhibit less hysteresis in their J-V curves and produce more current. These features are linked to reduced microstrain lessening ion migration, increasing charge collection efficiency and increasing current production.

Distribution of potassium after synthesis of the perovskite cells and throughout their operation of a photovoltaic, had a direct contribution on its overall power conversion efficiency. Specifically, ions like potassium, can assume defect sites to help reduce defects, driving better photovoltaic efficiency in the film. This trend in distribution changes after light soaking or implementing the device into operation. Exposure to light and darkness during AFM conductivity measurements simulates how conductivity changes as a function of light. Finally, correlating techniques like XRD, ToF-SIMS, and AFM showcase how substrate processing affects the strain, interfacial chemistry, morphology, and conductivity.

2.5 Conclusion: Relationship to Principles

This work highlights how the control of processing the electron transport layer in perovskites impacts the development of interfacial defects and ion distribution in the film, playing a role in the power conversion efficiency (PCE) as photovoltaic. Recall, that principle one focuses on the symbiotic relationship between synthesis and

characterization. Different techniques used to deposit tin oxide in these films modified properties like micro-strain, crystallite size, interfacial quality, and overall altered their PCE ranking in comparison to one another. Films synthesized with the hybrid approached reduced micro-strain to allow for a more defect tolerant perovskite growth in comparison to pure chemical bath deposition or nanoparticles.

These results also connect to the second principle, highlighting how materials are innately dynamic, the ToF-SIMS profiles show how potassium redistributes to the perovskite/tin oxide interface in hybrid films. This distribution is maintained or enhanced after light soaking, showing stable defect passivation under operational conditions. Other mobile ions, not potassium, show more subtle or secondary trends, reinforcing potassium as the dominant defect passivating species in this system. Finally, the third principle, emphasizing the need for complementary characterization techniques, is shown through the combination of XRD, ToF-SIMS, and c-AFM in this work. By utilizing all instrumentation, a collective research finding is uncovered: reduced strain in hybrid tin oxide deposition allows for potassium to potentially occupy interfacial defects sites that reduce recombination and yield higher and longer lasting photocurrent. This study on perovskite materials is a template for using correlative nanoscale tools to tune interfaces in other thin-film energy materials.

CHAPTER THREE

INVESTIGATING ANTIWEAR TRIBOFILM FORMATION

Antiwear tribofilms formed in lubricated mechanical contacts offer a complementary perspective on materials discovery, where the material of interest is not deposited in a conventional process but emerges dynamically at a sliding interface. This chapter uses tribofilms as a case study in how local chemistry and mechanics co-evolve under realistic operating conditions and how lubricant additives can be treated as synthesis parameters. Through controlled single-asperity experiments, this work tracks the nucleation and growth of low-friction films, revealing how sliding and thermal loading transform base oils and phosphorus-containing additives into chemically distinct tribofilms. Nanoscale friction mapping and nano-infrared spectroscopy are combined with time-of-flight secondary ion mass spectrometry to link changes in topography and mechanical response to the formation and spatial distribution of phosphorus and calcium-rich species within the film. By connecting these nanoscale observations, this chapter shows how specific additive chemistries and operating conditions can be used to deliberately engineer robust, low-friction tribofilms, illustrating a workflow in which dynamic film growth is treated as a tunable, designable materials process.

3.1 Synthesis of Antiwear Tribofilms as Evolving Dynamic Entities

Antiwear (AW) tribofilm growth in oil with phosphorus-based additives are measured with a variety of techniques to uncover how certain additives help reduce friction and maintain a long-standing lubrication barrier.[5] Calcium-phosphate materials were originally used as surface films for repairing human teeth and bones because of their

antiwear and strengthening properties in the medical field. After success in this application, calcium-phosphate additives were expanded to automatic transmission fluids (ATF) to strengthen antiwear properties to tribofilms in transmissions. A series of experiments are conducted with the following instrumentation: friction force microscopy (FFM) via an atomic force microscope (AFM), AFM with Nano-IR capabilities, and time-of-flight secondary ionization mass spectrometry (ToF-SIMS). Each method, shown in **Figure 3.1**, is utilized to uncover the chemical landscape of the tribofilm formation on the surface and through its depth. The development of tribofilms is prepared uniquely for each instrumentation method as described below. The oil composition dioleyl hydrogen phosphite (DOHP) was measured, along with DOHP and calcium additive, both notated in **Table 3.1** with their corresponding instrumentation methods.

3.1.1 Nano-IR Single Asperity Antiwear Tribofilm Preparation

Prior to oil deposition, stainless steel disks are sonicated in isopropyl alcohol for 15 minutes and dried under nitrogen. The oil to be deposited is then diluted in hexane at a 1:10 ratio, thinly applied via spin coating to the surface of the disks in 100 microliters. Afterwards, the disc is dried in a fume hood for 2 hours to allow the hexane to evaporate, leaving behind a uniform film of oil. A tribofilm is formed via a sliding contact between the AFM probe and oil surface during raster scanning, allowing for nanoscale growth over time. Information about the sample surface like morphology and ionic distribution can be acquired simultaneously in the AFM Nano-IR. An area of 50 x 50 microns was continuously scanned at room temperature under a pressure of 1.6 GPa to reach a film growth at 50 scans. Nano-IR spectra is recorded for wavenumber ranges of 1867 – 1504,

1410 – 1310, and 1147 – 917 cm^{-1}. The range of 1100 – 1150 cm^{-1} was thoroughly observed give the nature of the antiwear (AW) tribofilm and steel surface that would produce expected ionic compounds.

3.1.2 ToF-SIMS Single Asperity Antiwear Tribofilm Preparation

SA AW discs prepared for ToF-SIMS measurements follow a similar preparation approach as for the Nano-IR, however the oil is diluted in hexane at a 1:100 ratio with only 1 microliter applied to the surface. This logic is used to reduce the amount of oil solution present in the vacuum chamber of the ToF-SIMS. The oil solution is not spin-coated, due to its small volume, but still left to evaporate the hexane for 2 hours. After formation of the tribofilm in an AFM (not the Nano-IR), the remaining oil is rinsed with 100 microliters of hexane and then dried before transport into the ToF-SIMS.

3.1.3 ToF-SIMS Block-on-Ring Antiwear Tribofilm Preparation

Block-on-ring (BoR) experiments are constructed to mimic testing conditions run at Infineum USA LP. The block and ring test parts are imported from Falex Corporation and cleaned by sonication in heptane upon arrival. The same oil formulation is used from previous experiments with no dilution of hexane. Testing is run for 5 minutes, at a speed of 0.5 m/s, load of 100 N, and oil temperature of 110 C. The parts are then sonicated in heptane again to remove the residual oil, and then mounted onto a ToF-SIMS top mount holder for analysis. Depth profiles are measured on the leading edge of the sliding contact to showcase the bulk AW film.

3.2 Characterization of Single Asperity Antiwear Tribofilms

3.2.1 Nano-IR FFM of Single Asperity Prepared Films

Friction Force Microscopy (FFM) measurements are performed to understand how the antiwear (AW) tribofilm evolves under scanning conditions in the atomic force microscope (AFM). The AFM provides useful information regarding its changes in morphology over time with respect to the treated regions (scanned, with force to induce friction) and untreated regions (scanned, not inducing a friction-force contact). In **Figure 3.2**, a topography image is captured in a 80 x 80-micron area, with a centralized box previously scanned of 50 x 50 microns, representing the treated region with DOHP oil and calcium additive. A transition from a darker color in the outer box to a lighter color in the inner box in **Figure 3.2**a, shows a sharp increase a height, indicating a buildup of oil around the edges. The friction map in **Figure 3.2**b, demonstrates a corresponding sharp decrease in friction transitioning from the untreated to treated region, decreasing in value. The magnitude of volts (V) represents the load acting on the AFM tip, a higher value meaning more pressure applied to the tip/sample contact area during scanning. Plots featured in **Figure 3.2**c and **Figure 3.2**d, show the height increase and friction decrease in the highlighted region, as well as the average friction signal decrease as a function of the scans. Although it is confirmed that DOHP with calcium aids in reducing friction, it is uncertain how the ions in the oil are distributed under friction and what role they might play to induce this effect. Therefore, chemical differences are monitored through the AFM nano-IR system and time-of-flight secondary ionization mass spectrometer (ToF-SIMS).

The FFM methodology previously shown, is now combined with the AFM nano-IR measurements to understanding how local chemical changes occur spatially on the tribofilm surface. The IR signal corresponding to the Yubase 4 Plus base oil occurs at 1370 cm^{-1} during film formation. A unique IR signature is observed between 1111 and 1122 cm^{-1}, detected repeatedly, indicating different phosphite ions occurring in the treated areas of low friction. All these IR maps are showcased in **Figure 3.3**, featuring 1111 cm^{-1} represented by the phosphate ion (PO_4^{3-}) absorption band range, originating from the P-O stretching vibrations. When comparing chemical maps to the plotted spectra, it is evident that there are distinctive absorption differences between the treated and untreated regions. For example, unreacted phosphorous additive (1155 cm^{-1}) and the Yubase 4 Plus base oil (1370 cm^{-1}) is more dominant in the untreated region, compared to the treated region. It should be noted that while scanning in the treated region, oil could be pushed out of the scanning area and may cause accumulation in the untreated region, further explaining the higher absorption base oil IR signatures. Additionally, the reduction of the unreactive phosphorus additive could contribute to the conversion of free phosphite to the species identified in the phosphate ion (PO_4^{3-}) absorption band range.

3.2.2 ToF-SIMS of Single Asperity Prepared Films

A time-of-flight secondary ionization mass spectrometry (ToF-SIMS) study is conducted to observe the formation of the antiwear (AW) film in DOHP prepared with calcium. Both positive ion mode, featured in **Figure 3.4**, and negative ion mode, shown in **Figure 3.5**, are explored to further understand the chemical profile in treated and untreated regions. Surface imaging via ToF-SIMS of these films can serve as a secondary

method to confirm ionic compounds in the oil that may play a role in reducing friction. Both positive and negative ion analysis are conducted in the same area. It is evident that calcium is localized inside the scanning area during the single asperity (SA) experiment, while ions corresponding to hydrocarbons show a sharp reduction in intensity transition from the treated region to untreated region. The trend causing this transition for certain ionic species can be explained by a few possibilities – the solvent-rinsed films used for this experiment can conceal the components in the Yubase 4 Plus base oil since they are localized on the surface, these species undergo chemical transformations during the single asperity (SA) experiment, or are affected by the matrix effect in the SIMS instrumentation (i.e. inaccurate readings of ionic intensity due to the nature of the ToF-SIMS relaying on secondary ionization yields in comparison to the surrounding scanning area).

Analysis of key negative ion components in **Figure 3.5**, show localization of PO_x^-, calcium, phosphorus compounds, and oxidized species in the treated area. Although the intensities of these ions are lower, they are presently and likely affected by the solvent rinsing process. Depth profiling measurements are also scanned in **Figure 3.6**, to observe changes in chemistry throughout the film over time. Phosphorus based compounds peaks show the sharpest increase in the SA region over time. Calcium compounds face the opposite trend, decreasing as depth profiling approaches the bottom of the film. Therefore, it is interpreted that calcium is incorporated into the deposited film, yet how it is distributed across the film surface is still unknown.

3.2.3 ToF-SIMS of Block-on-Ring Antiwear Tribofilm

Block on ring (BoR) experiments are performed at an elevated temperature (110 C), to simulate realistic working conditions with DOHP and calcium additive oil. ToF-SIMS analysis for positive and negative ions is collected separately, allowing for use of different sputtering beams, O_2^+ and Cs^+ respectively. Previous ToF-SIMS analysis has shown there are many oxygen-based components in the oil, that differentiating signals from the O2+ beam is difficult. Seen in **Figure 3.7**, like before, phosphorus and calcium components show a higher intensity at the surface, gradually declining throughout the depth of the film. Depth profiling further confirms that calcium based compounds have relatively even surface distribution.

Overall, the oxygen containing components do not seem to show any major differences to the structure across the formulations. Slight variations are seen throughout the films for the phosphorus based compounds. Calcium based components are relatively uniform but their overall role is uncertain due to limited sensitivity of the instrumentation. The SA prepared films with the FFM and BoR methodology shows a great replication of what is measured via industry standard, providing helpful information on the full chemical profile for these oil formulations.

3.3 Discussion: The Influence of Calcium Additives on Tribofilms

When observing trends of tribofilm formulation through the lens of material considerations, instrumentation optimization is apparent for the evolution of chemistry during these experiments. For the DOHP with calcium oil, ToF-SIMS chemical imaging confirmed the presence of calcium in the treated area (i.e. location of antiwear tribofilm)

and depth profiling demonstrated localization of calcium ions distribution at the film surface. Calcium contributes to tribofilm formation due to its reaction to phosphorous and localization to the treated area. Additionally, calcium modifies surface chemistry by being localized near the film surface. Calcium also alters properties of the tribofilm interface by reinforcing antiwear effects of the film. Comparisons of DOHP and DOHP with calcium's reduction in friction from FFM were not measured, therefore it is still uncertain what mechanism allows calcium additives to reduce friction and wear, other than its chemical reaction with phosphorus. However, it seems to have influenced the mechanical properties of the tribofilm in terms of hardness or modulus, confirming previous results on calcium-phosphate automatic transmission fluids.

Measuring the tribofilm evolution on a steel disc versus the BoR had an impact on the ionic intensity in the ToF-SIMS, however trends agree with one another from both experiments. Tribofilm formation at the AFM tip-surface contact area was able to be achieved at around 50 scans. To maintain a uniform, thin layer, that could withstand the vacuum of the ToF-SIMS, it often needed to be diluted. Using both the AFM Nano-IR and ToF-SIMS, the chemical profile of the tribofilm is revealed cohesively for both steel discs and BoR industry standards.

3.4 Conclusion: Relationship to Principles

The work showcased in this chapter on antiwear tribofilms shows deep insight into how they form and evolve chemically and mechanically against friction forces under the influence of a calcium additive. The first principle shows how the combination of FFM, Nano-IR, and ToF-SIMS demonstrate that calcium additive not only reduce friction but

also change the chemistry and spatial distribution of tribofilm components. This illustrates how additive selection is a synthesis-level lever for engineering nanometer scale lubrication barriers. With the inclusion of the second principle, single asperity FFM results show nanoscale formation of a tribofilm with calcium rapidly produces a film with significant reduction in friction in the treated regions. Additionally, the Nano-IR shows how treated areas with lower friction are chemically distinct, the base oil and unreacted phosphite IR signatures diminish while phosphate-like bands emerge, indicating a tribo-chemical conversion driven by sliding force and heating.

Lastly, the third principle highlights how the ToF-SIMS results for both single asperity and BoR show enrichment of phosphorous and calcium containing species near the surface of the tribofilm, linking nanoscale AFM observations to the industry standard BoR tests. Depth profiling suggests that calcium is incorporated into the upper tribofilm regions while phosphorus rich species grow with depth and time, supporting that calcium modified phosphate networks underpin durable films with lower friction.

CHAPTER FOUR

NEUROMORPHIC MATERIAL TRANSFORMATIONS

4.1 Developing a Novel Method to Measure Conductivity Evolution in Memristor Materials

Resistive switching in oxide-based memristors is driven by highly localized redox reactions, filament formation, and Joule heating, all occurring on nanometer length scales and evolving over repeated electrical cycling.[3,120,96] This chapter examines tantalum oxide devices, focusing on how advanced scanning probe methods can be developed into quantitative tools for probing these dynamic processes. Central to this effort is the development of more accurate and realistic models of the AFM tip–cantilever system, informed by direct imaging of tip geometry and implemented in finite-element and other simulations to obtain accurate model of cantilever dynamics, electrostatic force distributions, and the effect of current flow through the tip-surface junction.[92] These models are used to interpret to experiments that leverage band-excitation and half-resonance excitation schemes, which enable the measurement of higher-harmonic responses such as those associated with local Joule heating into frequency windows with improved sensitivity and interpretability.[100,96] By systematically varying excitation conditions and laser position, this chapter establishes guidelines for using harmonic AFM measurements to map local thermal- and electro-mechanical behavior in operating memristors. In doing so, it highlights how carefully modeled and optimized measurement workflows can unlock new, insights into dynamic, field-driven material transformation at the nanoscale and provide a template for studying other emergent electronic systems with

a higher degree of quantitative manner. A workflow is designed to measure sensitive nanoscale phenomenon only detected in the second harmonic signal in AFM, like joule heating of the tip-surface junction as a new way to probe high frequency AC current flow. Ideally, following this development, a path to understanding and predicting the evolution of complex dynamic behavior such as resistive switching properties can be defined.

4.2 Nanoscale Mechanical Measurements: Quantifying Forces on a Cantilever

AFM is a surface science technique that is based on detecting the flexural changes of a cantilever. Often, these cantilevers are operated “on-resonance”, in order to take advantage of the intrinsic amplification of small forces and displacements that this affords. That is, an oscillating cantilever with one end held solidly and the other end fabricated with a sharp tip can be a sensitive probe, of physical interaction predominately emerging between the tip end and the sample when one brings the tip close to or in contact with a sample surface. As such, any quantification effort relies on a sufficiently detailed understanding and calibration of our resonator system, the cantilever. Since the cantilever is changed for every experiment, one must devise a workflow that incorporates calibration as a starting routine within the workflow without interfering with the experiment, and this is not a trivial task. One approach, is to design twin systems using modelling, that upon introduction and adjustment of the necessary geometrical and material parameters, allows us to create a “digital twin” of cantilever mechanics and dynamics, thus paving the way for accurate and reliable quantification. By creating this twin model in the COMSOL finite-element environment study, the dynamics, changes in

eigenfrequencies and eigenmodes, to effects of tip-surface forces and displacements arising from different phenomena including local heating, and interpret data from changing experimental parameters like laser position and tip-surface separation to test and refine models and improve calibration create and streamlined workflows to enable better AFM measurements and material insights.

4.2.1 COMSOL Simulation of Free Cantilever Eigenmodes

The first stage towards creating a digital twin of the experimental set-up is to calibrate cantilevers and tips is to create an accurate geometric model of the AFM cantilever and tip geometry, to estimate beyond the limitations of a simple harmonic oscillator (SHO) simplification what are the mechanical bending modes of a cantilever and how they evolve due to its interaction during interaction with a material surface.[93] The geometric modelling begins with obtaining a series of orthogonal SEM images of the AFM tip, showcased in **Figure 4.1a**, capture its 3D shape prior to or after scanning.

Additionally, tips can be made with different coatings that affect the structure of the tip itself. After use in an experiment, the shape of the tip can change significantly depending on this coating and can show slight changes among tips of the same make. When considering chemical changes that might occur during scanning, sample debris left behind on the tip can also influence the result. Energy-dispersive X-ray (EDX) can be used in conjunction with scanning electron microscopy (SEM) to help identify the chemical components of debris on the tip, which may be related to artifacts recorded in the images. Using SEM images and their magnitude of scale will serve as a base on which the AFM tip model can be built on.

A MATLAB software interface was developed to allow users to extract the key parameters from the experimental SEM images to create a digital model of the cantilever. For this workflow, a user loads SEM images and has tools to assign vertices. In MATLAB, the user is prompted to convert the micron scalebar from the SEM image into pixels. By simply clicking both ends of the scale bar, a new scale bar is created to translate the distance into pixels, while displaying the units in microns for the user. A tip position is identified, where the user selects the outermost point of the AFM tip and extracts the coordinates of this position for reference. Even though each of the orthogonal images in the set can be measured across the same scale, each image perspective will slightly vary in the x, y, z location of the tip. These points are then stored in a matrix as tip position coordinates that can be utilized as vertices locations for constructing the geometry of the model.

Once assigning the scale and tip position from the images, the user is prompted to select more vertices to outline the AFM tip shape. The more vertices and faces that are assigned, the more accurate the geometric model. The user is then prompted to select the same point in all image's perspectives to the best of their ability. Given that not all images can show the same vertex because of the perspective angle, axis guidelines are overlayed on all images. Once the same vertex is selected in all images, a matrix stores the x, y, z coordinates as a single point and assigns it numerically. As an example, point 1 has a location of x, y, and z microns. After the user assigns all points on the AFM tip, the software window closes, and the final vertices matrix is stored. To account for the missing axis location for each point, i.e. x and y can be located for a point but not z, all

points from all images are combined. At this stage, all points are assigned, and it is up to the user to use another interface to connect points to define faces as seen in **Figure 4.1b**. For example, points 1, 2, and 3 may make up face 1. Finally, to define a controlled tip-sample contact area, the last step in the MATLAB program is to truncate the tip so that well defined blunted tip is created. By truncating the AFM tip, the model demonstrates a more reliable and standardized way to implement a virtual simulation of the cantilever. Once completed, one can export a computer aided design (CAD) file to be used for analysis in COMSOL, shown in **Figure 4.1c**.

Once the cantilever model is defined, a series of COMSOL simulations using the eigenfrequency and parametric sweep studies are run to obtain the cantilever bending and twisting modes, and the associated characteristic frequencies. In order to simulate the dynamic response of a free ended cantilever (corresponding to the resonator away from the surface), the model uses a tip-sample contact stiffness of 0 N/m. Seen in **Figure 4.2** are the cantilever's first three vertical eigenmodes (i.e. fundamental, first, and second) and torsional eigenmode of a free oscillating cantilever. The obtained results from the simulations, were then compared with AFM experiments designed to test the accuracy of the model built using a realistic cantilever and tip geometry.

4.2.2 Simulation to Experiment: Comparing Shapes of Free Eigenmodes

To test the validity of the COMSOL model, a comparison is made against experimental measurements in the atomic force microscope (AFM). While the COMSOL model gives us a full picture of the mechanical bending of the cantilever, during experimental measurements the AFM typically captures the vibration/deflection of a

single point on the cantilever using the reflection of a laser that is detected by a 4-quadrant photodiode, under the so-called optical beam deflection (OBD) configuration, and provides information to track the resonance frequency of the cantilever (which is independent of the laser position) and the amplitude and phase at the particular laser spot position. When setting up a typical experiment, the laser is positioned on the cantilever approximately above the tip location (which falls underneath, facing the surface). This is somewhat arbitrary tradition but typically can give a high signal-to-noise ratio measurement of surface displacement. Location of the laser spot matters significantly, considering each eigen mode displays different z oscillation amplitudes along the length of the cantilever.[121], and there are sections across the cantilever that are considered "blind spots" (which can be seen as white fringes on the cantilever bending graphs in Figure 4.2). On these locations the OBD detects the cantilever position as fixed on the z-axis, despite the cantilever is vibrating. Thus, despite for regular AFM imaging one only needs to track the cantilever oscillations under one single laser spot, the whole cantilever bending shaped can be experimentally imaged by moving the laser spot along the x-axis while vibrating the cantilever. Recording the "deflection" signal from the OBD photodiode enables to measure the vertical displacements of the cantilever while the torsional vibrations of the cantilever can be tracked using the "lateral" signal of the OBD photodiode. Together they can build a picture of various mode shapes.

Designing this initial experiment requires use of the MacroBuilder program provided by Asylum Instruments. The macro is programmed to conduct an AC tune on the cantilever in free mode (i.e., it scans the excitation frequencies along a certain range and

records the amplitude of cantilever movement at the specific point under laser spot for each frequency). Next, it records the spectrum of frequencies acquired for each eigen mode, as a function of laser spot location, while moving the laser spot from the base of the cantilever to the free end. Ideally, the resulting resonance frequencies closely resemble those captured in the COMSOL model from the eigenfrequency study previously mentioned. Featured in **Figure 4.3a**, showcases the results for the laser spot located at the very edge of the cantilever and its corresponding AC tune. Three peaks are captured corresponding to the following eigenmodes: fundamental (~75 kHz), first (~461 kHz), and second (~1298 kHz). **Figure 4.3c** – **Figure 4.3e** compares each frequency peak from the experimental data set and its corresponding peak from COMSOL, while also demonstrating the eigen mode shape. When comparing the frequency values, the difference is only 0.3%-7.5%, the latter frequency values with greater error due to being recorded with the tip in free mode. In a separate experiment demonstrated in **Figure 4.3b**, a comparison is made of the vertical and torsional eigenmodes from a single laser spot position. These results show the vertical displacement of the first eigenmode and the torsional displacement of the second eigenmode. Overall, this step provides adequate verification that the simulation conducted in COMSOL shows the eigenmodes corresponding to those of a real cantilever.

After considering results at laser position on the cantilever free end, in order to compare the experimental measurements as a function of laser spot position along the cantilever with the simulations, revisions are made to the COMSOL model to calculate the amplitude and phase map at the multiple laser spot positions across the cantilever

(equivalent to looking at different x-axis points) via a parametric sweep study. As shown in **Figure 4.4a**, OBD laser position is varied to 10 different points along the length of the cantilever. A sinusoidal drive signal with a frequency sweep ranging from 0 MHz – 2 MHz is applied to cantilever as before to capture the eigen modes. In addition to the OBD positions, a boundary load is applied near the base of the cantilever simulating the blueDrive available in some AFM systems. The function of blueDrive is to focus a laser near the base of the cantilever to photothermally drive the cantilever.[122] For this purpose, a boundary load was applied in this area to act as a fixed load to help stabilize the tip vibration. The calculated amplitude and phase of the oscillation within this frequency range is then plotted as a color map and shown in **Figure 4.4.b**. This color maps are to be compared with the experimental values of amplitude and phase of oscillation in the same frequency range measured along the cantilever axis as explained above, and shown in **Figure 4.4.c.** It is to note that while the laser position was moved from the free end towards the base of the cantilever for the simulations, the experiments were run by shifting the laser position from the base of the cantilever towards the free end (so simulated and experimental data are mirrored on the y-axis).

In both data sets, the following resonance peaks are shown: first (75 kHz), second (~500 kHz), and third (~1240 kHz). As the laser position changes for both cases, the intensity of amplitude and phase change. Zero nodes are observed for the 75 kHz resonance, one node is indicated at 500 kHz, and two nodes are shown at 1240 kHz, and identified as red crosshairs in **Figures 4.4.b** and **4.4.c**. At these node locations, amplitude goes to zero and the phase shifts, indicating an inflection point. Observing zero nodes

represents the freely oscillating cantilever. Note that exact alignment of these nodes is not seen between experimental and COMSOL data, due to the difference in laser spot spacing since experimental data set acquired more points, which is not identically achieved in the COMSOL model.

4.2.3 Eigenmodes in Contact

To study the free cantilever bending modes shown in the previous sections, in the simulations the free end of the cantilever has been represented by virtually null tip-sample elastic interaction force, using k_z = 0 N/m, and experimentally, measurements have been performed by placing the tip away from the surface. However, the mechanical bending behavior of the cantilever changes if the free end starts to interact with the surface and eventually enters into contact, which can be modelled as a linear spring on the end of the cantilever such that $F_z = k_z \cdot \Delta z$. Although building a macro within the AFM software is helpful for initial experiments of cantilever calibration of the free mechanical bending modes, there are limitations when one aims to explore the evolution of the modes when bringing the tip into contact. For example, experimentally, laser position cannot be changed once the tip is in contact with the sample surface: the AFM feedback loop uses the deflection measurement to control the tip force (and position) when the AFM tip is in contact, so if the laser spot position changes and its deflection changes accordingly, the system can no longer detect if the tip is in contact. Additionally, AC tunes send a large range of frequency values (i.e. 0-2 MHz) to oscillate the tip, and thus design wise, these large frequency bands in the AC tunes limit the signal output of each resonance peak and thus low signal-to-noise. Therefore, in order to study the

evolution of the resonances of the cantilever when it is brought into contact with the surface, it is better to optimize this workflow by designing an experiment using external electronic and control hardware that enables changes the laser spot position while the tip is in-contact and sends a series of smaller frequency bands bounding the eigenfrequencies of the cantilever. Since the position of the cantilever in the z-axis can be changed at will, the workflow includes a parametric sweep of the z-scanner to observe the evolution of the mechanical bending modes from contact to free resonance.

To complement previous analysis of observing free eigenmodes, the results upon changing the z-position of the cantilever while measuring the resonance of the eigenmodes is shown in **Figure 4.5**. A wide band excitation from 20 kHz to 2000 kHz is applied through the BlueDrive laser to generate a thermomechanical excitation of the cantilever. The OBD laser spot is focused near the tip position at the cantilever end while the BlueDrive laser excitation is placed near the base of the cantilever. Starting from an initial contact position, with the tip applying an initial force on the surface F_0, vertical and torsional channels are tracked while the AFM tip moves away from the surface, in the upward Z direction for 50 steps, and then back downward for 50 steps. Thus, the tip begins in contact with the material surface and moves out of contact into a free oscillating mode in the first 50 steps as depicted in **Figure 4.5.1**. By changing the z-position of the cantilever, eigenmodes with different characteristic frequencies are observed while the tip is in contact as captured in **Figure 4.5** for both vertical and torsional channels.

To expand these findings experimentally, and obtain a mechanical bending map of the cantilever by varying the laser spot position in contact, a workflow in MATLAB is built

to do the following: record the position of the laser spot, send an excitation waveform to the AFM tip, record the response waveform, and move the laser to the next fixed location. In **Figure 4.6**, an excitation waveform is sent in contact mode with the following chirp ranges: 15 kHz sine wave, 140.5-179.5 kHz BE waveform, 359-389 kHz BE waveform, 557.5-572.5 kHz BE waveform, and 1115-1145 kHz BE waveform. While the resonance frequency of the cantilever is observed as almost constant in free oscillating modes, the resonance frequency peak in contact naturally shifts upon slight changes of force or tip-sample contact area as it often happens during scanning. By sending chirps of frequency bands to the tip, not only is the signal enhanced for that mode, but it is also more likely to be adequately captured within the window of excitation. To interpret the response signal from the measurements, a Fast Fourier Transform (FFT) is calculated to convert the time domain of the signal into the Fourier domain.[123] The response spectra recorded as amplitude of the tip as a function of time (i.e. chirp on/chirp off) are instead represented as amplitude of the tip as a function of frequency after FFT. Naturally, with AFM measurements, external vibrations and noise in the measurement electronics occurring in the environment create a "noise floor" that must be accounted for to differentiate peaks that indicate signal from the tip and other noise. A filtering process was applied to subtract the maximum intensity threshold of peaks within the response spectra to enhance observation on the peaks of interest (i.e. frequency peaks correlating to response modes). In **Figure 4.6** a 2D histogram of the response signal from the sine wave showcases the oscillation of amplitude at a sinusoidal vibration. The magnitude of amplitude is greatest at the tip and minimum at base of the

cantilever, and a central node corresponding to cantilever inflection while in contact is observed. When observing the other 2D plots of the amplitude as function laser spot position and excited frequency bins (i.e. frequency ranges of interest from modes), the response of the 2nd and 3rd modes are shown. As the laser moves from the tip (position #0) to the base (position #20) and back to the tip, a path of maximum amplitude values is formed. Maximum amplitude is shown at the tip that is contact with the surface and otherwise maintains a somewhat fixed value along the cantilever in the 2nd and 3rd modes. The width of the amplitude is kept within a confined frequency range in these modes, indicating that the frequency is not shifting much upon laser spot displacement while in contact. The dark blue columns in the 2D maps indicate blind spots along the cantilever, where the amplitude value goes to zero when the laser spot is in that location.

To validate the eigenmode shapes simulated for each mode of the cantilever, a comparison was made against a 1D finite element model (FEM) in **Table 4.1**. Considering the complexities involved with simulating movement accurately in x, y, and z directions, the 1D model simplifies the cantilever shape across a single axis. As demonstrated in the table, the eigenmodes achieved in COMSOL are close to those recorded from the 1D model, validating the accuracy of the COMSOL simulation.

4.3 Current Induced Joule Heating at the Nanoscale

Joule heating, also called resistive or Ohmic heating, is the process where electric current flowing through a conductor converts electrical energy into heat due to the material's resistance. This happens as electrons collide with atoms, transferring kinetic energy to heat. Joule heating thus occurs as well when current passes through the AFM

tip/material junction and can turn into a thermomechanical response which can be used as a means to measure AC current flow and help understand the functionality of materials like those in memristors. Using an AFM, a memristor material known as tantalum oxide (TaOx), will have its electrical behavior measured with a mechanical approach via the electrical into thermal energy conversion.

4.3.1 The Effect of Joule Heating on an AFM Tip

The concept of joule heating is defined as local heating that occurs from an electrical current, also known as resistive or Ohmic heating. This can be quantified through the relationships established in Ohm's law. For example, if determining the power output (or heating produced) in a circuit, the equation goes as follows:

$$P = I \times V; P = I^2 \times R; P = \frac{V^2}{R} \quad (4.1)$$

Where power (P), current (I), and voltage (V) are all components considered in an electrical circuit. For the case between a metallic AFM tip and conductive material, when a DC voltage is applied to the tip, a high current density passes through the tip-surface junction since the contact area is reduced to few hundreds of nm^2, which can cause local heating to occur. Consequently, tip thermal expansion can happen as a result. If an AC voltage is applied to the tip and current flows through the tip-surface junction, a heating-cooling cycle occurs that causes the tip to expand and contract, which can be detected through the very sensitive displacement measurements of AFM.

To understand this in more detail, let's consider the system formed by a metallic tip in contact with and electrode as an electronic circuit described in **Figure 4.7b,** where R_1 is

the resistance at the tip-surface junction. If we apply an AC voltage and a DC voltage to the circuit, the current *I* is the following:

$$I = \frac{V_{AC}(t) + V_{DC}}{R_1} \quad (4.2)$$

If solving for P_1 to determine joule heating at the tip-surface junction, a substitution in the relationship of power to current and resistance can be made:

$$P_1 = I^2 \times R_1 \quad (4.3)$$

$$P_1 = \left(\frac{V_{AC}(t) + V_{DC}}{R_1}\right)^2 \times R_1 \quad (4.4)$$

$$P_1 = \frac{(V_{AC}(t) + V_{DC})^2}{R_1} \quad (4.5)$$

Since the AC voltage is time dependent, the power conversion at the tip-surface junction will also show a time dependence as follows:

$$V(t) = V_{DC} + V_{AC} \sin(\omega t) \quad (4.6)$$

where:

$\omega = AC$ frequency (rad/s), t = time (s)

$$P(t) = \frac{\left(V_{DC} + V_{AC} \sin(\omega t)\right)^2}{R_1} \quad (4.7)$$

Therefore, with further expansion, the power converted into thermal energy as a function of time turns into:

$$P(t) = \frac{1}{R_1}[V_{DC}^2 + 2V_{DC}V_{AC} \sin(\omega t) + V_{AC}^2 sin^2(\omega t)] \quad (4.8)$$

which using the trigonometric substitution:

$$sin^2 x = \frac{1 - \cos(2x)}{2} \quad (4.9)$$

turns into:

$$P(t) = \frac{1}{R_1}\left[\left(V_{DC}^2 - \frac{V_{AC}^2}{2}\right) + 2V_{DC}V_{AC}\sin(\omega t) - \frac{V_{AC}^2}{2}\cos(2\omega t)\right] \quad (4.10)$$

Simplified further into:

$$P(t) = P_0 + P_w \sin(wt) + P_{2w}\sin(2wt + \pi/2) \quad (4.11)$$

This is the thermal power that drives the expansion of the tip volume due to Joule heating, and under an AC voltage of frequency *w*, this shows three different components: a constant heating, a thermal oscillation at the drive frequency w and thermal oscillation at twice the drive frequency 2w. If we now assume the heated region as thermal system, we can estimate the associated change in temperature as:

$$\Delta T(t) = H_{th}(w) \cdot P(t) \quad (4.12)$$

where H_{th} (w) is the thermal transfer function that correlates the change in temperature with the dissipated power, and is defined as:

$$H_{th}(w) = \frac{1}{G + iwC} \quad (4.13)$$

Where G is the thermal conductance to the environment and C is the effective heat capacity. From this temperature change, the thermal expansion of the tip in the z direction, can be estimated as:

$$\Delta z_{thermomechanical}(t) = \alpha L_0 \Delta T(t) = \frac{\alpha L_0}{G + iwC} \cdot P(t) \quad (4.14)$$

where α is the linear thermal expansion coefficient and L_0 is a characteristic thickness/length of the heated volume of the tip. Substituting Equation 4.12 and 4.13 into 4.14, we obtain a local surface thermal induced deformation that can be split into harmonics as:

$$\Delta z_{th}|_w = \alpha L_0 H_{th}(w) \cdot P_W \sin(wt) \sim \frac{2\,V_{DC}V_{AC}}{R_1}\sin(wt) \quad (4.15)$$

$$\Delta z_{th}|_{2w} = \alpha L_0 H_{th}(w) \cdot P_{2W} \sin\left(2wt + \frac{\pi}{2}\right) \sim \frac{V_{AC}^2}{2R_1} \sin\left(2wt + \frac{\pi}{2}\right) \quad (4.16)$$

With this deviation, the second harmonic frequency is double that of the first harmonic, as expected. Additionally, notice that the first harmonic produces sin(*wt*) and the second harmonic produces cos(*2wt*) frequency. Considering this, the second harmonic signal is 90 degrees out of phase with respect to the first harmonic.

Figure 4.8 shows the graphic correlation between power dissipation at a simple resistance as a function of AC and DC voltages which leads to the thermal driving force inducing a thermoelastic deformation of the surface. As depicted in the graph and the last set of equations, if we are only applying an ac voltage, the Joule heating will lead to a thermomechanical response only at the second harmonic with respect to the driving AC voltage, that is proportional to the square of the driving AC voltage. However, if a DC voltage is present, an electromechanical signal at the same excitation frequency of the ac voltage emerges which shows a linear dependence with both, the AC and the DC voltages. Thus, AFM is a useful tool for measuring effects like joule heating, because current can also impact the deflection of the cantilever through the heating within the constricted region between the tip and surface and therefore thermal expansion which can be detected by the cantilever's deflection signal. The result of this relationship is that if bias is driven through the circuit at one frequency, the cantilever will be driven at twice that frequency.

We have developed here the hypothesis that the current passing through a tip-surface junction under an applied voltage can induce a thermomechanical deformation that will be detectable as a cantilever vibration by AFM. However, when an AC voltage is applied

to a surface using the conductive tip of a cantilever, other electro-mechanical responses in can emerge as previously reported[96] and featured in **Figure 4.9**, showcasing how the first and second harmonic amplitude calculations of this multiple signal sources are defined. If we consider the equation for the first harmonic response, we observe the effect of piezoelectric responses as well as electrostatic interactions and thus it shows dependence on the following variables: piezoelectric coefficient of the material (d), amplitude of driving bias (V_0), spring constant of the cantilever (k_{cant}), and the cantilever-sample capacitance (C_{cant}). In the second harmonic equation, the signal emerges from sample electrostriction, Joule heating and also electrostatic tip sample coupling, thus depending in the following variables: electrostrictive coefficient (M), joule heat transduction coefficient (B), capacitor electrical resistance (R), and amplitude of capacitor current (I_0). While one cannot rule out other sources of mechanical deformation signal upon the application of an AC voltage, electrostrictive and electrostatic interactions are minimized when using a top electrode and measuring a conductive material, while Joule heating is maximized due to the higher current densities passing through the tip-sample junction on conductive setups. Thus, this creates a new way to measure AC current at high frequency that normal transimpedance amplifiers are unable to measure.

4.3.2 Half-Resonance Band Excitation for Thermomechanical Measurements

Joule heating, a heating effect that is a by-product of current flow through resistor capacitors (i.e tip and conductive surface) can derive from various locations – within the tip, at the tip/surface contact, and underneath the surface contact. Under an AC voltage, it emerges primarily as a thermomechanical induced signal at twice the drive frequency. To

maximize the AFM sensitivity to such a signal, one can use a method identified as half-resonance band excitation (HBE). The strategy is to use band excitation (BE) to send a band of frequencies to the cantilever at half of a resonance frequency of the cantilever (typically the fundamental eigenmode), so that the second harmonic of the response falls within the resonance band and is naturally amplified by the cantilever resonance, where the signal can then be measured.[96] In BE, this signal is sent to the AFM tip as a "chirp", and the method was developed and commonly used to measure the phase and amplitude in piezo force microscopy (PFM)[100]; while scanning in contact mode, the contact area of the AFM tip is constantly changing, and utilizing BE can allow the user to track better the shifts of the contact resonance peak by defining a width for the band of frequencies (instead of a single frequency) to drive the tip and thus capture the whole resonance peak.

Therefore, in BE, a Fast Fourier Transform (FFT) approach is used to convert this harmonic waveform as a function of time to a function of frequency. To take an FFT of the data, recall the equation for a Discrete Fourier Transform (DFT)[124]:

$$\widehat{f_k} = \sum_{j=0}^{n=1} f_j e^{-i2\pi jk/n} \quad (4.17)$$

where $\widehat{f_k}$ is the Fourier transform coefficient, f_j is the experimental function (i.e. one of many voltage v. time plots), and n is the number of data points in each f_j . The fundamental frequency equation for which the DFT is built on is the following:

$$\omega_n = e^{-2\pi i/n} \; ; i = \sqrt{-1} \quad (4.18)$$

Consequently, data vector f_j is multiplied by each row in the matrix using the $\widehat{f_k}$ equation to solve for the Fourier coefficient. For this data, the FFT is used, which is a simplified approach to DFT for large volumes of data.

$$DFT = \sigma(n^2)\,; FFT = \sigma(nlog(n)) \quad (4.19)$$

As shown in **Figure 4.10**, the waveform constructed from **Figure 4.7d** is transformed to drive at half-resonance ($\frac{1}{2}\omega$) while measuring on resonance (ω), then to drive and measure on resonance.

4.3.3 Results and Discussion

A series of AFM experiments are designed using the half-resonance band excitation (HBE) technique to explore the relationship of Joule heating with the second harmonic mechanical signal. To demonstrate the proof of concept of thermomechanical measurements with an AFM tip, the following two environments are constructed:

1. Ohmic resistance: Metal to Metal – Pt Coated AFM tip on Ni electrode
2. Schottky contact: Metal to Semiconductor - Uncoated dopped Si AFM tip on Ni electrode

It is achieved by setting up a circuit using a conductive AFM tip on top of an electrode connected to a resistor box. For the first environment, a Pt-Ir coated AFM tip or Budget Sensors Multi 75E-G tip is used on a nickel electrode. For the second environment, the metal-semiconductor contact is created by putting in contact a semiconductor tip made of highly dopped Si with a nickel electrode, leading to a Schottky barrier and rectifying contact. For this set-up, an excitation waveform is sent to the tip, after which the first and second harmonic signals are measured, alongside current flow through the circuit using a DC current and measure using an external current amplifier connected to the sample. As featured in **Figure 4.7d**, the waveform alternates between applying a DC voltage and measuring current with applying an AC voltage on top of the DC voltage over time and

then measure dynamic mechanical response. The user defines the DC voltage, AC voltage, and number of steps in the waveform (or voltage steps) prior to beginning the experiment. Finally, a resistor box is included in the circuit to easily alter the total current passing through the circuit. Ideally with less resistance, more current can pass through the circuit and allow for more joule heating to occur and thus demonstrate the thermomechanical nature of the signal through its relation to P_1.

4.3.4 Nanoscale Thermomechanical Measurements on a Metallic Electrode

The first environment can be described as an ohmic contact between two metals, the metallic tip and electrode, connected in series with a resistance from the resistor box. The circuit is depicted in **Figure 4.11a**. In this case, the current passing through the circuit is:

$$I_{total} = \frac{V_{AC}(t) + V_{DC}}{R_1 + R_2} \quad (4.20)$$

Note that the experimentally measured current is captured by applying only a DC voltage, and thus:

$$I_{DC} = \frac{V_{DC}}{R_1 + R_2} \quad (4.21)$$

In any case, the total current through the circuit can be modulated by selecting different resistances from the resistor box, while we consider the tip sample contact resistance R_1 as constant. In this case, the thermal driving force will be the power dissipated *only* at the tip-surface resistance, since the power dissipated in the resistor box is not contributing to the mechanical measurements. Thus, we only care about the component:

$$P_1 = \left(\frac{V_{AC}(t) + V_{DC}}{R_1 + R_2}\right)^2 \times R_1 \quad (4.22)$$

$$P(t) = \frac{R_1}{[R_1 + R_2]^2} \cdot \left[\left(V_{DC}^2 - \frac{V_{AC}^2}{2}\right) + 2V_{DC}V_{AC}\sin(\omega t) - \frac{V_{AC}^2}{2}\cos(2\omega t)\right] \quad (4.23)$$

By now following the same equations development as in Section 4.3.1, in this case, we end up with the thermomechanical responses for the first environment expressed by:

$$\Delta z_{th}|_w \sim \frac{R_1}{[R_1+R_2]^2} \cdot 2\, V_{DC} V_{AC} \cdot \sin(wt) = \frac{R_1}{[R_1+R_2]^2} \cdot 2\, I_{DC} V_{AC} \cdot \sin(wt) \quad (4.24)$$

$$\Delta z_{th}|_{2w} \sim \frac{R_1}{[R_1+R_2]^2} \cdot V_{AC}^2 \cdot \sin\left(2wt + \frac{\pi}{2}\right) \quad (4.25)$$

Since the external resistance R_2 modulates the total current passing through the circuit, the total thermomechanical response can be modulated by changing the resistance from the box. Demonstrated in **Figure 4.11** is the snapshot of the data collected prior to FFT analysis. As mentioned in the experimental setup, 2D maps showing the first and second harmonic are shown alongside the driving waveform and current flow. As current flows through the tip-surface junction, that amplitude signal increases in the first harmonic while the second harmonic signal stays constant throughout.

The results from the ohmic contact first environment, a coated AFM tip on a nickel electrode, are demonstrated in **Figure 4.12**. For an ohmic contact, significant joule heating should be occurring at the tip/surface junction. A linear relationship between the DC voltage and DC current is observed in the I-V curves shown in **Figure 4.12a** as expected from an Ohmic resistance. The first harmonic signal shown in **Figure 4.12b** follows suit with a linear response between the first harmonic amplitude and DC voltage. For an ohmic contact, it would be expected that the first harmonic signal would showcase a linear relationship with the DC current. Additionally, the slope of the current changes with the external resistance applied in the circuit, which follows suit of the ratio between current and resistance outlined in Equation 4.2. As more resistance is added to the circuit, less heating is produced at the tip which creates smaller amplitude under the same applied

AC voltage. Finally, as expected from Equation 4.25 the second harmonic signal is independent of the V_{DC}.

4.3.5 Nanoscale Thermomechanical Measurements on a Diode-like Contact

For the second environment, an uncoated silicon tip is placed on a bare nickel electrode, creating a Schottky barrier contact. Recall, a Schottky barrier occurs between a semiconductor and metal contact, where the potential energy of electrons formed at the metal-semiconductor junction must overcome the barrier to move from the valence band to the conductive band.[125] Additionally, the work function, or the minimum energy required to remove an electron, of the semiconductor must be smaller than that of the metal. This schematic is demonstrated in **Figure 4.13** highlighting the following concepts – Schottky barrier height, Fermi level, conduction band, and valence band.

To solve for the Schottky barrier height, consider the isolated metal work function equation:

$$\Phi_M = E_0 - E_F \quad (4.26)$$

Where E_0 is the vacuum energy, or minimum energy required for electrons to free themselves. E_F is the energy at the Fermi level. Likewise, the isolated semiconductor work equation is the following:

$$\Phi_s = \chi + (E_c + E_F)\,; \chi = E_0 - E_c \quad (4.27)$$

Which includes the energy at the conduction band or E_c and electron affinity χ.

Therefore, both equations combine to solve for the Schottky barrier height of the electrons:

$$\Phi_{Bn} = \Phi_M - \chi \quad (4.28)$$

To help visualize this environment in comparison to what is observed experimentally, a basic physics model is constructed that considers a n-silicon tip and nickel cap junction. Seen in **Figure 4.13**, the following modeling results are plotted – Schottky barrier, parasitic resistance, limit of the resistor box (R_b), and the total output of all signals previously mentioned. Only DC voltage is considered for this model, not AC voltage.

When observing general trends in the model, the Schottky line abruptly begins to increase in current at an angle under a certain applied DC voltage (around 0.5 V for this model). The angle of this line simulates the resistance given from the resistor box in the circuit which must be accounted for in the current flow at the Schottky junction. The parasitic line is simply representative of the excess current produced at the junction. This is accounted for before the Schottky barrier is overcome and becomes the dominating driving force of current produced. The V/Rb limit is the current produced through the circuit from flowing through the resistor box, which is adjusted externally by the user. Lastly, the total line is simply the addition of all previous lines to showcase an average current output simulated at the nickel-silicon tip Schottky junction.

The equations used to calculate each variable at the junction in the model will be derived. To derive an equation for the Schottky barrier in parallel with parasitic resistance, both in series with a resistor box, consider the DC voltage:

$$V_{DC} = I_{total} \times R_b + V_1 \quad (4.29)$$

And therefore, the total current flow in the circuit:

$$I_{\text{total}} = I_{\text{Schottky}}(V_{\text{device}}) + V_{\text{device}} / R_1 \quad (4.30)$$

Where $I_{Schottky}$ is the current produced from overcoming the Schottky barrier. To solve for $I_{Schottky}$, consider the role of thermionic emission from the occurrence of joule heating at the tip-surface junction. Thermionic emission is the emission of electrons when thermal energy of a hot electrode overcomes the material's work function. Solving for Schottky current:

$$I_{Schottky} = I_0 \left[\exp(V_1 / (nV_{th})) - 1\right] \quad (4.31)$$

Where saturation current (I_0) is:

$$I_0 = AA^*T^2 \exp(-\varphi_B / (k_B T)) \quad (4.32)$$

And thermal voltage (V_{th}) is:

$$V_{th} = k_B T / q \quad (4.33)$$

The values used for these equations are identified in **Table 4.2** and parameters like contact area, absolute temperature, and ideality factor can be adjusted for better fitting to the experimental environment in this case. To derive the power or joule heating produced at the tip/surface junction, simply substitute variables previously derived in the first case:

$$P_1 = (I_{Schottky})^2 \times R_1 \; ; \; R_1 = \frac{V_{DC}}{I_{Schottky}} \quad (4.34)$$

Parasitic parallel resistance is represented by leakage current through surface states, bulk defects, or alternative conduction mechanisms. It appears in parallel with Schottky and tunnel barriers, following Ohm's law parasitic current is:

$$I_{parasitic} = V_1 / R_p \quad (4.35)$$

Lastly, to consider the limit of the resistor box (I_{max}):

$$I_{max} = V_{DC} / R_b \quad (4.36)$$

After deriving these equations for the following parameters – Schottky barrier, parasitic resistance, and limit of the resistor box, the physics model can be constructed. The circuit equation for the model can be derived as the following:

$$f(V_1) = (V_{AC} + V_{DC}) - (I_{total} \text{ x } R_2 \text{ x } V_1) - V_1 = 0. \quad (4.37)$$

This equation can be further simplified with the Newton—Raphson method. This method approximates the function by applying tangent lines near guess values, that then allow the next root of the function to be identified. This approximation improves along the curve like so:

$$V_1^{(k+1)} = V_1^{(k)} - f / (df/dV_1) \quad (4.38)$$

Where f is $f(V_1)$ and k is the iteration number.

There are some assumptions to be made on behalf of the model for simplification. Firstly, tunneling is not considered since it is not a significant driving force for current flow at the Schottky tip-surface junction for this system. The Schottky barrier height is assumed constant and non-bias dependent. Image force, or when an electron approaches a dielectric layer to induce positive charge on the interface causing conduction and valence band bending, lowering for Schottky emission is also neglected. The Schottky barrier height is also considered uniform and does not account for barrier height inhomogeneities or patches. Lastly, space charge effects and series resistance in the bulk semiconductor are lumped into R_b. In summary, for a Schottky barrier, the current changes as a function of DC voltage in a non-linear manner. However, if we substitute the Schottky voltage in the equations for the calculation of the dissipated power developed in Section 4.3.1, we

end up obtaining thermomechanical responses at the tip sample junction that still satisfy the following relationships for the first and second harmonics:

$$\Delta z_{th}|_w \sim I_{DC} V_{AC} \cdot \sin(wt) \quad (4.39)$$

$$\Delta z_{th}|_{2w} \sim \frac{dI_{DC}}{dV} \cdot V_{AC}^2 \cdot \sin\left(2wt + \frac{\pi}{2}\right) \quad (4.40)$$

Figure 4.14 shows the experimental results for the conductive and thermomechanical measurements done for the second environment where a Schottky barrier is created between an uncoated semiconductor silicon tip on a metallic electrode. When recalling the physics model previously simulated, the I-V curve is mirrored since the rectifying behavior is happening in the opposite current direction, however the angled barrier that is observed at a certain DC voltage value is still observed. This highlights that what is shown experimentally agrees with theory and a Schottky barrier is demonstrated for this environment. The first and second harmonic signals are different for this environment in comparison to the ohmic contact, because these signals are dependent on the resistance and power at the tip surface junction (i.e. R_1, P_1). As the DC voltage bias goes into the negative direction, current increase is identically observed in both the I-V and first harmonic signal plots. The I-V and first harmonic signals show similarities because an increase in the thermomechanical driving force shows an increase in the first harmonic signal. If current is flowing through at this point, overcoming the Schottky barrier, it should follow trend with the change in current. The second harmonic signal shows an increase with an increase in current, indicating a local effect like joule heating to occur. If joule heating is occurring at this DC voltage value, it would be expected to see a different response in the cantilever oscillation due to expansion in the tip or tip/surface junction.

4.4 Nanoscale Conductivity Behavior in TaOx

HBE has previously been shown effective for measuring leakage current in nano-capacitors, therefore, there is potential that conductive filaments in memristive materials like tantalum oxide (TaOx) can be revealed as well.[126] Ion migration driving resistive switching in TaOx is induced by the voltage sent by the AFM tip to the sample surface. When ions migrate to form conductive filaments in TaOx, what type of heating occurs at the surface junction and might it play a role in how to predict its switching behavior?

Understanding sensitive measurements like joule heating through a more accurate perspective of AFM tip geometry, is a perfect example of considerations required for expanding the materials discovery landscape for memristors. While tip effects play a role during scanning, the interaction between the tip and material surface can also drive results. It is helpful to better understanding the interaction between each component, especially in the realm of lower signal (e.g. joule heating). Since conductive filaments are relatively randomized and difficult to pinpoint, improving the way we measure them via AFM can help refine the parameters required to switch them. The nature of how conductive filaments form and rupture change as a result to their environment – current flow, pathway availability between electrodes, temperature, local heating, etc. How they are switched and measured (i.e. AFM tip) influences the behavior for how they switch and what by-products are formed as a result. Combining the approach of COMSOL and AFM experiments help reinforce each other to develop a robust model of a complex system, while also recognizing the gaps in calibration required for acquiring data experimentally.

4.4.1 Results and Discussion

Once thermomechanical measurements with an AFM tip have been demonstrated, we proceed to apply these measurements to a memristor material, to try to depict the changes in current during the resistive switching behavior via the associated thermomechanical response. To this end, a sample stack is synthesized for the AFM experiments utilizing a memristor material and dielectric material that can be accessed separately and together, to understand trends in switching for these materials. The two harmonic signals are captured on a time scale, but are analyzed separately in the frequency domain.[96] The resistive switching material used in these experiments is TaOx and the sample configuration is described in **Figure 4.15.** The voltage to activate the TaOx layer is applied through the top electrodes deposited on the TaOx layer, which is accessed with the AFM tip, and the current is measured from the middle gate electrode. The equations for this case should be the same as those derived for case 2:

$$P_1 = (I_{Memristor})^2 \times R_1 \; ; \; R_1 = \frac{V_{DC}}{I_{Memristor}} \quad (4.41)$$

Where $I_{Memristor}$ is dependent on the contact area between the combined tip and electrode (i.e. metal) and TaOx layer (i.e. semiconductor):

$$I_{\text{Memristor}} = I_0 \left[\exp(V_1 / (nV_{\text{th}})) - 1\right] \quad (4.42)$$

It should be noted that although a resistive switching material is used, tantalum dioxide (TaOx), the material is not being switched between a high resistance state (HRS) and low resistance state (LRS), instead being stimulated by a sweeping voltage. For conductive filaments to form and rupture, allowing TaOx to transition between HRS and LRS, a series of pulses must be sent to the material at a setting voltage and reading

voltage. The setting voltage is voltage applied in which the resistance state is maintained without external stimuli, followed by a reading voltage that is close to zero for measuring the resistance. The waveform being sent to the material in this experiment is the same for the other two cases and shown in **Figure 4.7d**, where the material is constantly exposed to stimuli, alternating between DC voltage and DC+AC voltage (i.e., when the AC voltage signal is sent through the circuit, DC voltage is still present). Instead of forming conductive filaments, it is theorized that ionic mobility is maintained through the TaOx layer underneath the electrode during the experiment.

Figure 4.16 shows the experimental results of the current measurements and thermomechanical response on both, BE on-resonance and HBE measurements. When comparing these results to the physics model of the Schottky barrier, the I-V looks almost identical, showing that although this environment is not simulating a Schottky barrier, the TaOx capacitor still shows some rectifying behavior. As the current increases in the I-V curve, the second harmonic signal increases as well for some lower resistance values and is steady at higher resistance values. It seems that the impact of the user setting on the resistor box has a larger influence on the second harmonic signal for this case. This helps identify the range of current flow in the circuit that can pass through to cause effects like joule heating in materials that have resistive switching behavior. The first harmonic signal shows a linear decrease in signal with no current flow. However, it has a sudden increase in signal when current increases, seen in both the I-V and second harmonic signal. This could be explained by that when the first harmonic signal is decreasing, the repulsive forces at the tip/surface contact are decreasing, until there is a sudden increase

in current. Overcoming a barrier like conductive filament formation where this current increase is seen could be the reason. Possibly, joule heating is happening at the junction like observed in the previous environment but localized in a different location. Since mobile ions are moving through the TaOx layer under excitation, trying to build conductive filaments, joule heating could be more predominate under the metallic cap. It can be theorized that the barrier observed in this environment is similar to what is observed in the Schottky junction case. On the other hand, the semiconductor and metal contact for this environment is different. For the previous case, the semiconductor contact was the tip and the metal contact was the electrode. For this case, it is predicted that the metallic tip and metallic cap act as a joint contact against the semiconductor material that is TaOx. This could also explain why the I-V curve for this environment is different than the Schottky barrier case, the orientation of the semiconductor/metal contact is different. Like what was derived in the equations for these environments, it is expected that the surface area for this environment is different as well, influencing the value of current and power at the tip/surface junction.

In addition to this analysis, SEM images were captured for all tips used for these environments and shown in **Figure 4.17**. Qualitatively, fewer containments are seen on the tip from the ohmic contact environment and more contaminants are seen for the other two cases. For the case where the magnitude of the second harmonic signal was greatest (i.e. first environment with ohmic contact), greater heating could have occurred leaving behind less residue after the experiment. Overall, deformation to the tip is evident,

indicating significant local effects were occurring at the tip-surface junction during the HBE measurements.

4.5 Relationship to Principles

This work exemplifies the first principle, highlighting the coupling between synthesis and application in material functionality. Identifying the many unknowns for applications of memristors leads one to understand the synthesis of instrumentation utilized to study these materials (i.e. AFM) and how it can be improved in the way it measures local phenomena like the tip geometry at the tip/surface junction and other effects such as joule heating. Likewise, the location of the laser position on the cantilever and other calibration maneuvers that users set, alters the outcome of how tip oscillation is measured, seen in the work done through COMSOL simulations and AFM experiments.

For the second principle, showing how the dynamic nature of materials causes them to evolve under their operation and characterization, showcases how local effects like joule heating influences current flow in memristors. Additionally, phenomena like Schottky barrier can form between a simple tip and electrode junction. With all these observations in mind, the third principle shows its importance for the need of correlated techniques in a materials discovery workflow. Evident ties between simulations in COMSOL and experiments in the AFM show the desire for a well-defined understanding of tip geometry, tip movement, and its influence on material characterization. The selection of the AFM mode used to study the behavior of a material is also crucial, shown in the utilization of half-resonance band excitation for measuring joule heating effects in the second harmonic signal.

CHAPTER FIVE

RECOMMENDATIONS FOR FUTURE MATERIAL PIONEERING

As stated throughout this work, three underlying principles guide an optimal materials discovery workflow. For each principle, a recommendation is provided that is influenced from the previous investigations into perovskites, antiwear tribofilms, and memristors. In the first principle, it states that the connection between synthesis and application can be traveled in both directions in solving a scientific question. Material functionality is rooted in how the material is created and what it is used for. Making alterations to synthesis techniques for perovskites impacts defect formation that is detrimental for photovoltaics but beneficial for memory devices. Calcium additives in antiwear tribofilms can aid in reducing friction for transmission lubricants. Lastly, improving AFM cantilever dynamics through simulations can reveal unique functionality insights into complex materials like memristors. Overall, the recommendation for this insight is to consider if a scientific discovery is more related to synthesis or application and allow that to be the direction of workflow at the start. Looking closely at what ties synthesis and application together provides valuable information.

The second principle examines how materials are dynamic entities and therefore evolve during their use and often while being characterized. The redistribution of potassium is evident in the hybrid-prepared perovskite films, maintained even after long periods of sun exposure. Other ions show less movement, highlighting that potassium is a leading ion to passivate defects at the perovskite and substrate interface. For tribofilms, FFM shows how calcium improved friction reduction in treated areas and the Nano-IR

highlights how low friction areas have higher counts of phosphate-like bands, distinguishing them from untreated areas. Joule heating findings for memristor materials are demonstrated through a unique approach of AFM. Considering all these works, it is recommended to consider how materials change through which they are characterized. Questions such as – is this an attribute of the material or a result of what is exposed to by instrumentation? Can this characterization tool aid in revealing additional functionality? are highly encouraged.

The final principle focuses on how the combination of characterization methods is required to transform material application from the laboratory to commercialization. The collection of analysis by XRD, ToF-SIMS, and c-AFM uncovers an important role of ionic distribution influenced by the synthesis methods of the perovskite substrate layer. The ToF-SIMS and Nano-IR results of antiwear tribofilms showcases calcium distribution throughout the film during its growth and how its presence changes the frictional properties of the lubricant on both single asperity and block-on-ring environments. Connecting finite element models and AFM experiments to calibrate tip geometry on materials is crucial for understanding local sensitive behavior such as joule heating. A recommendation for this principle is to consider cross-referencing the results of material characterization with another tool to confirm that the phenomena observed is in fact telling the full story of the material's capabilities and application.

REFERENCES

(1) Metcalf, I.; Sidhik, S.; Zhang, H.; Agrawal, A.; Persaud, J.; Hou, J.; Even, J.; Mohite, A. D. Synergy of 3D and 2D Perovskites for Durable, Efficient Solar Cells and Beyond. *Chemical Reviews* **2023**, *123* (15), 9565-9652. DOI: 10.1021/acs.chemrev.3c00214.

(2) Khan, A. M.; Ahmed, J.; Liu, S.; Martin, T.; Berkebile, S.; Chung, Y.-W.; Wang, Q. J. Formation of Wear-Protective Tribofilms on Different Steel Surfaces During Lubricated Sliding. *Tribology Letters* **2023**, *71* (2), 63. DOI: 10.1007/s11249-023-01735-2.

(3) Strukov, D. B.; Snider, G. S.; Stewart, D. R.; Williams, R. S. The missing memristor found. *Nature* **2008**, *453* (7191), 80-83. DOI: 10.1038/nature06932.

(4) Hysmith, H.; Park, S. Y.; Yang, J.; Ievlev, A. V.; Liu, Y.; Zhu, K.; Sumpter, B. G.; Berry, J.; Ahmadi, M.; Ovchinnikova, O. S. The Role of SnO2 Processing on Ionic Distribution in Double-Cation–Double Halide Perovskites. *ACS Applied Materials & Interfaces* **2023**, *15* (30), 36856-36865. DOI: 10.1021/acsami.3c03520.

(5) Lorenz, M.; Pawlicki, A. A.; Hysmith, H. E.; Cogen, K.; Thaker, H.; Ovchinnikova, O. S. Direct Multimodal Nanoscale Visualization of Early Phosphorus-Based Antiwear Tribofilm Formation. *ACS Applied Materials & Interfaces* **2022**, *14* (30), 35157-35166. DOI: 10.1021/acsami.1c16761.

(6) Fu, Z.; Xu, M.; Sheng, Y.; Yan, Z.; Meng, J.; Tong, C.; Li, D.; Wan, Z.; Ming, Y.; Mei, A.; et al. Encapsulation of Printable Mesoscopic Perovskite Solar Cells Enables High Temperature and Long-Term Outdoor Stability. *Advanced Functional Materials*

2019, *29* (16), 1809129. DOI: https://doi.org/10.1002/adfm.201809129 (acccessed 2024/11/04).

(7) Ma, S.; Yuan, G.; Zhang, Y.; Yang, N.; Li, Y.; Chen, Q. Development of encapsulation strategies towards the commercialization of perovskite solar cells. *Energy & Environmental Science* **2022**, *15* (1), 13-55, 10.1039/D1EE02882K. DOI: 10.1039/D1EE02882K.

(8) Wang, Y.; Lv, Z.; Chen, J.; Wang, Z.; Zhou, Y.; Zhou, L.; Chen, X.; Han, S.-T. Photonic Synapses Based on Inorganic Perovskite Quantum Dots for Neuromorphic Computing. *Advanced Materials* **2018**, *30* (38), 1802883. DOI: https://doi.org/10.1002/adma.201802883 (acccessed 2024/11/04).

(9) Vasilopoulou, M.; Mohd Yusoff, A. R. b.; Chai, Y.; Kourtis, M.-A.; Matsushima, T.; Gasparini, N.; Du, R.; Gao, F.; Nazeeruddin, M. K.; Anthopoulos, T. D.; et al. Neuromorphic computing based on halide perovskites. *Nature Electronics* **2023**, *6* (12), 949-962. DOI: 10.1038/s41928-023-01082-z.

(10) Khemnani, M.; Tripathi, B.; Thakkar, P.; Gosai, J.; Jain, M.; Chandra, P.; Solanki, A. Investigating the Role of Interfacial Layer for Resistive Switching in a Hybrid Dion-Jacobson Perovskite-Based Memristor. *ACS Applied Electronic Materials* **2023**, *5* (9), 5249-5256. DOI: 10.1021/acsaelm.3c01038.

(11) Nguyen-Tri, P.; Ghassemi, P.; Carriere, P.; Nanda, S.; Assadi, A. A.; Nguyen, D. D. Recent Applications of Advanced Atomic Force Microscopy in Polymer Science: A Review. In *Polymers*, 2020; Vol. 12.

(12) Chen, H.; Qin, Z.; He, M.; Liu, Y.; Wu, Z. Application of Electrochemical Atomic Force Microscopy (EC-AFM) in the Corrosion Study of Metallic Materials. In *Materials*, 2020; Vol. 13.

(13) Fletcher, J. S.; Conlan, X. A.; Jones, E. A.; Biddulph, G.; Lockyer, N. P.; Vickerman, J. C. TOF-SIMS Analysis Using C60. Effect of Impact Energy on Yield and Damage. *Analytical Chemistry* **2006**, *78* (6), 1827-1831. DOI: 10.1021/ac051624w.

(14) Welzel, T.; Mändl, S.; Ellmer, K. Cluster ion formation during sputtering processes: a complementary investigation by ToF-SIMS and plasma ion mass spectrometry. *Journal of Physics D: Applied Physics* **2014**, *47* (6), 065204. DOI: 10.1088/0022-3727/47/6/065204.

(15) Belianinov, A.; Ievlev, A. V.; Lorenz, M.; Borodinov, N.; Doughty, B.; Kalinin, S. V.; Fernández, F. M.; Ovchinnikova, O. S. Correlated Materials Characterization via Multimodal Chemical and Functional Imaging. *ACS Nano* **2018**, *12* (12), 11798-11818. DOI: 10.1021/acsnano.8b07292.

(16) Liu, Y.; Lorenz, M.; Ievlev, A. V.; Ovchinnikova, O. S. Secondary Ion Mass Spectrometry (SIMS) for Chemical Characterization of Metal Halide Perovskites. *Advanced Functional Materials* **2020**, *30* (35), 2002201. DOI: https://doi.org/10.1002/adfm.202002201 (acccessed 2024/11/04).

(17) Kalinin, S. V.; Ziatdinov, M.; Ahmadi, M.; Ghosh, A.; Roccapriore, K.; Liu, Y.; Vasudevan, R. K. Designing workflows for materials characterization. *Applied Physics Reviews* **2024**, *11* (1), 011314. DOI: 10.1063/5.0169961 (acccessed 9/18/2024).

(18) Jin, Y.; Kumar, P. V. Bayesian optimisation for efficient material discovery: a mini review. *Nanoscale* **2023**, *15* (26), 10975-10984, 10.1039/D2NR07147A. DOI: 10.1039/D2NR07147A.

(19) Szymanski, N. J.; Rendy, B.; Fei, Y.; Kumar, R. E.; He, T.; Milsted, D.; McDermott, M. J.; Gallant, M.; Cubuk, E. D.; Merchant, A.; et al. An autonomous laboratory for the accelerated synthesis of novel materials. *Nature* **2023**, *624* (7990), 86-91. DOI: 10.1038/s41586-023-06734-w.

(20) Hysmith, H.; Foadian, E.; Padhy, S. P.; Kalinin, S. V.; Moore, R. G.; Ovchinnikova, O. S.; Ahmadi, M. The future of self-driving laboratories: from human in the loop interactive AI to gamification. *Digital Discovery* **2024**, *3* (4), 621-636, 10.1039/D4DD00040D. DOI: 10.1039/D4DD00040D.

(21) Delgado-Licona, F.; Abolhasani, M. Research Acceleration in Self-Driving Labs: Technological Roadmap toward Accelerated Materials and Molecular Discovery. *Advanced Intelligent Systems* **2023**, *5* (4), 2200331. DOI: https://doi.org/10.1002/aisy.202200331 (acccessed 2024/10/09).

(22) Shimizu, R.; Kobayashi, S.; Watanabe, Y.; Ando, Y.; Hitosugi, T. Autonomous materials synthesis by machine learning and robotics. *APL Materials* **2020**, *8* (11), 111110. DOI: 10.1063/5.0020370 (acccessed 10/9/2024).

(23) MacLeod, B. P.; Parlane, F. G. L.; Morrissey, T. D.; Häse, F.; Roch, L. M.; Dettelbach, K. E.; Moreira, R.; Yunker, L. P. E.; Rooney, M. B.; Deeth, J. R.; et al. Self-driving laboratory for accelerated discovery of thin-film materials. *Science Advances 6* (20), eaaz8867. DOI: 10.1126/sciadv.aaz8867 (acccessed 2024/10/09).

(24) Seifrid, M.; Pollice, R.; Aguilar-Granda, A.; Morgan Chan, Z.; Hotta, K.; Ser, C. T.; Vestfrid, J.; Wu, T. C.; Aspuru-Guzik, A. Autonomous Chemical Experiments: Challenges and Perspectives on Establishing a Self-Driving Lab. *Accounts of Chemical Research* **2022**, *55* (17), 2454-2466. DOI: 10.1021/acs.accounts.2c00220.

(25) MacLeod, B. P.; Parlane, F. G. L.; Berlinguette, C. P. How to build an effective self-driving laboratory. *MRS Bulletin* **2023**, *48* (2), 173-178. DOI: 10.1557/s43577-023-00476-w.

(26) Maffettone, P. M.; Friederich, P.; Baird, S. G.; Blaiszik, B.; Brown, K. A.; Campbell, S. I.; Cohen, O. A.; Davis, R. L.; Foster, I. T.; Haghmoradi, N.; et al. What is missing in autonomous discovery: open challenges for the community. *Digital Discovery* **2023**, *2* (6), 1644-1659, 10.1039/D3DD00143A. DOI: 10.1039/D3DD00143A.

(27) Stein, H. S.; Gregoire, J. M. Progress and prospects for accelerating materials science with automated and autonomous workflows. *Chemical Science* **2019**, *10* (42), 9640-9649, 10.1039/C9SC03766G. DOI: 10.1039/C9SC03766G.

(28) Blaiszik, B.; Chard, K.; Pruyne, J.; Ananthakrishnan, R.; Tuecke, S.; Foster, I. The Materials Data Facility: Data Services to Advance Materials Science Research. *JOM* **2016**, *68* (8), 2045-2052. DOI: 10.1007/s11837-016-2001-3.

(29) Pendleton, I. M.; Cattabriga, G.; Li, Z.; Najeeb, M. A.; Friedler, S. A.; Norquist, A. J.; Chan, E. M.; Schrier, J. Experiment Specification, Capture and Laboratory Automation Technology (ESCALATE): a software pipeline for automated chemical experimentation and data management. *MRS Communications* **2019**, *9* (3), 846-859. DOI: 10.1557/mrc.2019.72.

(30) Er-raji, O.; Rustam, L.; Kore, B. P.; Glunz, S. W.; Schulze, P. S. C. Insights into Perovskite Film Formation Using the Hybrid Evaporation/Spin-Coating Route: An In Situ XRD Study. *ACS Applied Energy Materials* **2023**, *6* (11), 6183-6193. DOI: 10.1021/acsaem.3c00698.

(31) Magazzù, A.; Marcuello, C. Investigation of Soft Matter Nanomechanics by Atomic Force Microscopy and Optical Tweezers: A Comprehensive Review. In *Nanomaterials*, 2023; Vol. 13.

(32) Lanza, M. A Review on Resistive Switching in High-k Dielectrics: A Nanoscale Point of View Using Conductive Atomic Force Microscope. In *Materials*, 2014; Vol. 7, pp 2155-2182.

(33) Ievlev, A. V.; Brown, C.; Burch, M. J.; Agar, J. C.; Velarde, G. A.; Martin, L. W.; Maksymovych, P.; Kalinin, S. V.; Ovchinnikova, O. S. Chemical Phenomena of Atomic Force Microscopy Scanning. *Analytical Chemistry* **2018**, *90* (5), 3475-3481. DOI: 10.1021/acs.analchem.7b05225.

(34) McKinney, W. *Python for data analysis: data wrangling with Pandas, NumPy, and IPython*; O'Reilly Media Inc., 2012.

(35) Hahn, D. T. V. a. B. H. *Essential MATLAB for engineers and scientists*; Academic Press, 2022.

(36) Dulac-Arnold, G.; Levine, N.; Mankowitz, D. J.; Li, J.; Paduraru, C.; Gowal, S.; Hester, T. Challenges of real-world reinforcement learning: definitions, benchmarks and analysis. *Machine Learning* **2021**, *110* (9), 2419-2468. DOI: 10.1007/s10994-021-05961-4.

(37) Ziatdinov, M. A.; Liu, Y.; Morozovska, A. N.; Eliseev, E. A.; Zhang, X.; Takeuchi, I.; Kalinin, S. V. Hypothesis Learning in Automated Experiment: Application to Combinatorial Materials Libraries. *Advanced Materials* **2022**, *34* (20), 2201345. DOI: https://doi.org/10.1002/adma.202201345 (acccessed 2024/10/09).

(38) Ziatdinov, M.; Liu, Y.; Kelley, K.; Vasudevan, R.; Kalinin, S. V. Bayesian Active Learning for Scanning Probe Microscopy: From Gaussian Processes to Hypothesis Learning. *ACS Nano* **2022**, *16* (9), 13492-13512. DOI: 10.1021/acsnano.2c05303.

(39) Snapp, K. L.; Brown, K. A. Driving school for self-driving labs. *Digital Discovery* **2023**, *2* (5), 1620-1629, 10.1039/D3DD00150D. DOI: 10.1039/D3DD00150D.

(40) Wang, H.; Fu, T.; Du, Y.; Gao, W.; Huang, K.; Liu, Z.; Chandak, P.; Liu, S.; Van Katwyk, P.; Deac, A.; et al. Scientific discovery in the age of artificial intelligence. *Nature* **2023**, *620* (7972), 47-60. DOI: 10.1038/s41586-023-06221-2.

(41) Huynh, K. K.; Pham, S. T.; Tieu, K. A.; Wan, S. Tribocatalysis Induced Carbon-Based Tribofilms—An Emerging Tribological Approach for Sustainable Lubrications. In *Lubricants*, 2023; Vol. 11.

(42) Ramadan, A. J.; Oliver, R. D. J.; Johnston, M. B.; Snaith, H. J. Methylammonium-free wide-bandgap metal halide perovskites for tandem photovoltaics. *Nature Reviews Materials* **2023**, *8* (12), 822-838. DOI: 10.1038/s41578-023-00610-9.

(43) Goulding, A. N., J. F. Leung, and R.W. Neu. Communicating Materials Systems Knowledge through Processing-Structure-Properties Performance (PSPP) Maps. *Journal of Materials Education* **2018**, *40* (1-2), 1-18.

(44) Gosvami, N. N.; Ma, J.; Carpick, R. W. An In Situ Method for Simultaneous Friction Measurements and Imaging of Interfacial Tribochemical Film Growth in Lubricated Contacts. *Tribology Letters* **2018**, *66* (4), 154. DOI: 10.1007/s11249-018-1112-0.

(45) Sun, Z.; Chen, X.; He, Y.; Li, J.; Wang, J.; Yan, H.; Zhang, Y. Toward Efficiency Limits of Crystalline Silicon Solar Cells: Recent Progress in High-Efficiency Silicon Heterojunction Solar Cells. *Advanced Energy Materials* **2022**, *12* (23), 2200015. DOI: https://doi.org/10.1002/aenm.202200015 (acccessed 2024/09/18).

(46) Wei, T.; Lu, Y.; Zhang, F.; Tang, J.; Gao, B.; Yu, P.; Qian, H.; Wu, H. Three-Dimensional Reconstruction of Conductive Filaments in HfOx-Based Memristor. *Advanced Materials* **2023**, *35* (10), 2209925. DOI: https://doi.org/10.1002/adma.202209925 (acccessed 2024/11/04).

(47) Bhalla, A. S.; Guo, R.; Roy, R. The perovskite structure—a review of its role in ceramic science and technology. *Materials Research Innovations* **2000**, *4* (1), 3-26. DOI: 10.1007/s100190000062.

(48) Weber, D. Das Perowskitsystem CH3NH3 [Pb,Sn1-nX3] (X = Cl, Br, I) / The Perovskite System CH3NH3[PbnSn1-nX3] (X = C1, Br, I). **1979**, *34* (7), 939-941. DOI: doi:10.1515/znb-1979-0712 (acccessed 2024-09-18).

(49) Chen, Y.; Sun, Y.; Peng, J.; Tang, J.; Zheng, K.; Liang, Z. 2D Ruddlesden–Popper Perovskites for Optoelectronics. *Advanced Materials* **2018**, *30* (2), 1703487. DOI: https://doi.org/10.1002/adma.201703487 (acccessed 2024/09/18).

(50) Grancini, G.; Nazeeruddin, M. K. Dimensional tailoring of hybrid perovskites for photovoltaics. *Nature Reviews Materials* **2019**, *4* (1), 4-22. DOI: 10.1038/s41578-018-0065-0.

(51) Cheng, X.; Yang, S.; Cao, B.; Tao, X.; Chen, Z. Single Crystal Perovskite Solar Cells: Development and Perspectives. *Advanced Functional Materials* **2020**, *30* (4), 1905021. DOI: https://doi.org/10.1002/adfm.201905021 (acccessed 2024/09/18).

(52) Saki, Z.; Byranvand, M. M.; Taghavinia, N.; Kedia, M.; Saliba, M. Solution-processed perovskite thin-films: the journey from lab- to large-scale solar cells. *Energy & Environmental Science* **2021**, *14* (11), 5690-5722, 10.1039/D1EE02018H. DOI: 10.1039/D1EE02018H.

(53) Green, M. A.; Ho-Baillie, A. Perovskite Solar Cells: The Birth of a New Era in Photovoltaics. *ACS Energy Letters* **2017**, *2* (4), 822-830. DOI: 10.1021/acsenergylett.7b00137.

(54) Krishna, A.; Gottis, S.; Nazeeruddin, M. K.; Sauvage, F. Mixed Dimensional 2D/3D Hybrid Perovskite Absorbers: The Future of Perovskite Solar Cells? *Advanced Functional Materials* **2019**, *29* (8), 1806482. DOI: https://doi.org/10.1002/adfm.201806482 (acccessed 2024/09/18).

(55) Saidaminov, M. I.; Abdelhady, A. L.; Murali, B.; Alarousu, E.; Burlakov, V. M.; Peng, W.; Dursun, I.; Wang, L.; He, Y.; Maculan, G.; et al. High-quality bulk hybrid perovskite single crystals within minutes by inverse temperature crystallization. *Nature Communications* **2015**, *6* (1), 7586. DOI: 10.1038/ncomms8586.

(56) Ameri, T.; Dennler, G.; Lungenschmied, C.; Brabec, C. J. Organic tandem solar cells: A review. *Energy & Environmental Science* **2009**, *2* (4), 347-363, 10.1039/B817952B. DOI: 10.1039/B817952B.

(57) Chen, C.; Chen, J.; Han, H.; Chao, L.; Hu, J.; Niu, T.; Dong, H.; Yang, S.; Xia, Y.; Chen, Y.; et al. Perovskite solar cells based on screen-printed thin films. *Nature* **2022**, *612* (7939), 266-271. DOI: 10.1038/s41586-022-05346-0.

(58) Liu, X.; Cao, L.; Guo, Z.; Li, Y.; Gao, W.; Zhou, L. A Review of Perovskite Photovoltaic Materials' Synthesis and Applications via Chemical Vapor Deposition Method. In *Materials*, 2019; Vol. 12.

(59) Sanchez, S. L.; Tang, Y.; Hu, B.; Yang, J.; Ahmadi, M. Understanding the ligand-assisted reprecipitation of CsPbBr₃ nanocrystals via high-throughput robotic synthesis approach. *Matter* **2023**, *6* (9), 2900-2918. DOI: 10.1016/j.matt.2023.05.023 (acccessed 2024/09/18).

(60) Baker, F. Highest Efficiency Perovskite Solar Cells. *Ossila* **2025**.

(61) Milot, R. L.; Eperon, G. E.; Snaith, H. J.; Johnston, M. B.; Herz, L. M. Temperature-Dependent Charge-Carrier Dynamics in CH3NH3PbI3 Perovskite Thin Films. *Advanced Functional Materials* **2015**, *25* (39), 6218-6227. DOI: https://doi.org/10.1002/adfm.201502340 (acccessed 2024/09/18).

(62) Tai, Q.; You, P.; Sang, H.; Liu, Z.; Hu, C.; Chan, H. L. W.; Yan, F. Efficient and stable perovskite solar cells prepared in ambient air irrespective of the humidity. *Nature Communications* **2016**, *7* (1), 11105. DOI: 10.1038/ncomms11105.

(63) Ball, J. M.; Petrozza, A. Defects in perovskite-halides and their effects in solar cells. *Nature Energy* **2016**, *1* (11), 16149. DOI: 10.1038/nenergy.2016.149.

(64) Gosvami, N. N.; Bares, J. A.; Mangolini, F.; Konicek, A. R.; Yablon, D. G.; Carpick, R. W. Mechanisms of antiwear tribofilm growth revealed in situ by single-asperity sliding contacts. *Science* **2015**, *348* (6230), 102-106. DOI: 10.1126/science.1258788 (acccessed 2024/09/18).

(65) Demartini, M.; Ferrari, M.; Govindan, K.; Tonelli, F. The transition to electric vehicles and a net zero economy: A model based on circular economy, stakeholder theory, and system thinking approach. *Journal of Cleaner Production* **2023**, *410*, 137031. DOI: https://doi.org/10.1016/j.jclepro.2023.137031.

(66) Philippon, D.; de Barros-Bouchet, M. I.; Mogne, T. L.; Gresser, E.; Martin, J. M. Experimental simulation of phosphites additives tribochemical reactions by gas phase lubrication. *Tribology - Materials, Surfaces & Interfaces* **2007**, *1* (3), 113-123. DOI: 10.1179/175158408X273586 (acccessed 2024/09/18).

(67) What is Transmission Fluid and What Does it Do? Universal Technical Institute: 2020.

(68) Minfray, C.; Martin, J. M.; De Barros, M. I.; Mogne, T. L.; Kersting, R.; Hagenhoff, B. Chemistry of ZDDP Tribofilm by ToF-SIMS. *Tribology Letters* **2004**, *17* (3), 351-357. DOI: 10.1023/B:TRIL.0000044483.68571.49.

(69) Philippon, D.; De Barros-Bouchet, M. I.; Le Mogne, T.; Lerasle, O.; Bouffet, A.; Martin, J. M. Role of nascent metallic surfaces on the tribochemistry of phosphite

lubricant additives. *Tribology International* **2011**, *44* (6), 684-691. DOI: https://doi.org/10.1016/j.triboint.2009.12.014.

(70) Zou, X.; Xu, S.; Chen, X.; Yan, L.; Han, Y. Breaking the von Neumann bottleneck: architecture-level processing-in-memory technology. *Science China Information Sciences* **2021**, *64* (6), 160404. DOI: 10.1007/s11432-020-3227-1.

(71) Markov, I. L. Limits on fundamental limits to computation. *Nature* **2014**, *512* (7513), 147-154. DOI: 10.1038/nature13570.

(72) Chua, L. Memristor-The missing circuit element. *IEEE Transactions on Circuit Theory* **1971**, *18* (5), 507-519. DOI: 10.1109/TCT.1971.1083337.

(73) Thomas, A. Memristor-based neural networks. *Journal of Physics D: Applied Physics* **2013**, *46* (9), 093001. DOI: 10.1088/0022-3727/46/9/093001.

(74) Xu, C.; Dong, X.; Jouppi, N. P.; Xie, Y. Design implications of memristor-based RRAM cross-point structures. In *2011 Design, Automation & Test in Europe*, 14-18 March 2011, 2011; pp 1-6. DOI: 10.1109/DATE.2011.5763125.

(75) Valov, I.; Tsuruoka, T. Effects of moisture and redox reactions in VCM and ECM resistive switching memories. *Journal of Physics D: Applied Physics* **2018**, *51* (41), 413001. DOI: 10.1088/1361-6463/aad581.

(76) Memristors. IntechOpen: Rijeka, 2020.

(77) Mohanty, S. K.; Panda, D.; Reddy, K. P. K.; Lee, P.-T.; Wu, C.-H.; Chang, K.-M. Uniform resistive switching and highly stable synaptic characteristics of HfOx sandwiched TaOx-based memristor for neuromorphic system. *Ceramics International*

2023, *49* (11, Part A), 16909-16917. DOI: https://doi.org/10.1016/j.ceramint.2023.02.052.

(78) Jacobs-Gedrim, R. B.; Hughart, D. R.; Vizkelethy, G.; Vaandrager, B. L.; Swanson, S. E.; Taggart, J. L.; Barnaby, H.; Marinella, M. *Effect of Radiation on the Classification Accuracy of a Neural Network Trained on Analog TaOx Resistive Memory Arrays*; Sandia National Lab.(SNL-NM), Albuquerque, NM (United States), 2018.

(79) Bao, K.; Meng, J.; Poplawsky, J. D.; Skowronski, M. Electrical conductivity of TaOx as function of composition and temperature. *Journal of Non-Crystalline Solids* **2023**, *617*, 122495. DOI: https://doi.org/10.1016/j.jnoncrysol.2023.122495.

(80) Jiang, L.; Jin, Y.; Zhao, Y.; Meng, J.; Zhang, J.; Chen, X.; Wu, X.; Xiao, Y.; Tao, Z.; Jiang, B.; et al. An Efficient Design of TaOx-Based Memristor by Inserting an Ultrathin Al2O3 Layer with High Stability for Neuromorphic Computing and Logic Operation. *Advanced Physics Research* **2023**, *2* (5), 2200086. DOI: https://doi.org/10.1002/apxr.202200086 (acccessed 2024/11/04).

(81) Zhao, J. L.; Teo, K. L.; Zheng, K.; Sun, X. W. Color tunable electroluminescence and resistance switching from a ZnO-nanorod–TaOx–p-GaN heterojunction. *Nanotechnology* **2016**, *27* (11), 115204. DOI: 10.1088/0957-4484/27/11/115204.

(82) Ren, S.-G.; Xue, Y.-B.; Zhang, Y.; Zuo, W.-B.; Li, Y.; Miao, X.-S. High-temperature tolerant TaOX/HfO2 self-rectifying memristor array with robust retention and ultra-low switching energy. *Applied Physics Letters* **2024**, *124* (3), 033501. DOI: 10.1063/5.0190308 (acccessed 11/4/2024).

(83) Binnig, G.; Quate, C. F.; Gerber, C. Atomic Force Microscope. *Physical Review Letters* **1986**, *56* (9), 930-933. DOI: 10.1103/PhysRevLett.56.930.

(84) Goldsbury, C. S.; Scheuring, S.; Kreplak, L. Introduction to Atomic Force Microscopy (AFM) in Biology. *Current Protocols in Protein Science* **2009**, *58* (1), 17.17.11-17.17.19. DOI: https://doi.org/10.1002/0471140864.ps1707s58 (acccessed 2024/09/19).

(85) Cappella, B.; Dietler, G. Force-distance curves by atomic force microscopy. *Surface Science Reports* **1999**, *34* (1), 1-104. DOI: https://doi.org/10.1016/S0167-5729(99)00003-5.

(86) Sader, J. E.; Larson, I.; Mulvaney, P.; White, L. R. Method for the calibration of atomic force microscope cantilevers. *Review of Scientific Instruments* **1995**, *66* (7), 3789-3798.

(87) Sedin, D. L.; Rowlen, K. L. Influence of tip size on AFM roughness measurements. *Applied Surface Science* **2001**, *182* (1), 40-48. DOI: https://doi.org/10.1016/S0169-4332(01)00432-9.

(88) Ted Limpoco, F.; Beck, D. E. How to Choose the Right AFM Probe for Your Experiment. *Microscopy Today* **2023**, *31* (4), 22-27. DOI: 10.1093/mictod/qaad055 (acccessed 10/10/2024).

(89) Higgins, M.; Proksch, R.; Sader, J. E.; Polcik, M.; Mc Endoo, S.; Cleveland, J.; Jarvis, S. Noninvasive determination of optical lever sensitivity in atomic force microscopy. *Review of Scientific Instruments* **2006**, *77* (1).

(90) Ogletree, D. F.; Carpick, R. W.; Salmeron, M. Calibration of frictional forces in atomic force microscopy. *Review of Scientific Instruments* **1996**, *67* (9), 3298-3306. DOI: 10.1063/1.1147411 (acccessed 10/10/2024).

(91) Cannara, R. J.; Eglin, M.; Carpick, R. W. Lateral force calibration in atomic force microscopy: A new lateral force calibration method and general guidelines for optimization. *Review of Scientific Instruments* **2006**, *77* (5), 053701. DOI: 10.1063/1.2198768 (acccessed 10/10/2024).

(92) Bhushan, B.; Fuchs, H. *Applied scanning probe methods II*; Springer, 2006.

(93) Stark, R. W.; Heckl, W. M. Higher harmonics imaging in tapping-mode atomic-force microscopy. *Review of Scientific Instruments* **2003**, *74* (12), 5111-5114. DOI: 10.1063/1.1626008 (acccessed 1/16/2026).

(94) Mullin, N.; Vasilev, C.; Tucker, J. D.; Hunter, C. N.; Weber, C. H. M.; Hobbs, J. K. "Torsional tapping" atomic force microscopy using T-shaped cantilevers. *Applied Physics Letters* **2009**, *94* (17). DOI: 10.1063/1.3126047 (acccessed 1/16/2026).

(95) Rabe, U.; Turner, J.; Arnold, W. Analysis of the high-frequency response of atomic force microscope cantilevers. *Applied Physics A: Materials Science & Processing* **1998**, *66* (7).

(96) Kim, Y.; Kumar, A.; Tselev, A.; Kravchenko, II; Han, H.; Vrejoiu, I.; Lee, W.; Hesse, D.; Alexe, M.; Kalinin, S. V.; et al. Nonlinear phenomena in multiferroic nanocapacitors: joule heating and electromechanical effects. *ACS Nano* **2011**, *5* (11), 9104-9112. DOI: 10.1021/nn203342v From NLM.

(97) Harnagea, C.; Pignolet, A.; Alexe, M.; Hesse, D. Higher-order electromechanical response of thin films by contact resonance piezoresponse force microscopy. *IEEE Transactions on Ultrasonics, Ferroelectrics, and Frequency Control* **2006**, *53* (12), 2309-2322. DOI: 10.1109/TUFFC.2006.179.

(98) Instruments, Z. Principles of lock-in detection and the state of the art. *White Paper* **2023**.

(99) Research, A. Contact Resonance Viscoelastic Mapping Mode. *Oxford Instruments* **2014**.

(100) Jesse, S.; Kalinin, S. V.; Proksch, R.; Baddorf, A. P.; Rodriguez, B. J. The band excitation method in scanning probe microscopy for rapid mapping of energy dissipation on the nanoscale. *Nanotechnology* **2007**, *18* (43), 435503. DOI: 10.1088/0957-4484/18/43/435503.

(101) Kalinin, S. V.; Rar, A.; Jesse, S. A decade of piezoresponse force microscopy: progress, challenges, and opportunities. *IEEE Transactions on Ultrasonics, Ferroelectrics, and Frequency Control* **2006**, *53* (12), 2226-2252. DOI: 10.1109/TUFFC.2006.169.

(102) Butt, H.-J. Measuring electrostatic, van der Waals, and hydration forces in electrolyte solutions with an atomic force microscope. *Biophysical Journal* **1991**, *60* (6), 1438-1444. DOI: 10.1016/S0006-3495(91)82180-4 (acccessed 2024/10/10).

(103) Ono, L. K.; Qi, Y. Surface and Interface Aspects of Organometal Halide Perovskite Materials and Solar Cells. *The Journal of Physical Chemistry Letters* **2016**, *7* (22), 4764-4794. DOI: 10.1021/acs.jpclett.6b01951.

(104) Kopycinska-Müller, M.; Geiss, R. H.; Hurley, D. C. Contact mechanics and tip shape in AFM-based nanomechanical measurements. *Ultramicroscopy* **2006**, *106* (6), 466-474. DOI: https://doi.org/10.1016/j.ultramic.2005.12.006.

(105) Xiao, X.; Qian, L. Investigation of Humidity-Dependent Capillary Force. *Langmuir* **2000**, *16* (21), 8153-8158. DOI: 10.1021/la000770o.

(106) Melitz, W.; Shen, J.; Kummel, A. C.; Lee, S. Kelvin probe force microscopy and its application. *Surface Science Reports* **2011**, *66* (1), 1-27. DOI: https://doi.org/10.1016/j.surfrep.2010.10.001.

(107) Grove, T.; Masters, M.; Miers, R. Determining dielectric constants using a parallel plate capacitor. *American journal of physics* **2005**, *73* (1), 52-56.

(108) Domon, B.; Aebersold, R. Mass Spectrometry and Protein Analysis. *Science* **2006**, *312* (5771), 212-217. DOI: 10.1126/science.1124619 (acccessed 2024/09/19).

(109) Mahoney, C. M. Cluster secondary ion mass spectrometry of polymers and related materials. *Mass Spectrometry Reviews* **2010**, *29* (2), 247-293. DOI: https://doi.org/10.1002/mas.20233 (acccessed 2024/09/19).

(110) Benninghoven, A. Chemical Analysis of Inorganic and Organic Surfaces and Thin Films by Static Time-of-Flight Secondary Ion Mass Spectrometry (TOF-SIMS). *Angewandte Chemie International Edition in English* **1994**, *33* (10), 1023-1043. DOI: https://doi.org/10.1002/anie.199410231 (acccessed 2024/09/19).

(111) Wang, P.; Wang, J.; Zhang, X.; Wang, H.; Cui, X.; Yuan, S.; Lu, H.; Tu, L.; Zhan, Y.; Zheng, L. Boosting the performance of perovskite solar cells through a novel active

passivation method. *Journal of Materials Chemistry A* **2018**, *6* (32), 15853-15858, 10.1039/C8TA05593A. DOI: 10.1039/C8TA05593A.

(112) Sundara Raj, D. K. M.; Madhu, G. M.; Biju, V. X-ray diffraction line profile analysis of nanostructured nickel oxide: Shape factor and convolution of crystallite size and microstrain contributions. *Physica E: Low-dimensional Systems and Nanostructures* **2016**, *85*. DOI: 10.1016/j.physe.2016.08.035.

(113) Chen, B.; Li, T.; Dong, Q.; Mosconi, E.; Song, J.; Chen, Z.; Deng, Y.; Liu, Y.; Ducharme, S.; Gruverman, A.; et al. Large electrostrictive response in lead halide perovskites. *Nature Materials* **2018**, *17* (11), 1020-1026. DOI: 10.1038/s41563-018-0170-x.

(114) Oka, D.; Hirose, Y.; Matsui, F.; Kamisaka, H.; Oguchi, T.; Maejima, N.; Nishikawa, H.; Muro, T.; Hayashi, K.; Hasegawa, T. Strain Engineering for Anion Arrangement in Perovskite Oxynitrides. *ACS Nano* **2017**, *11* (4), 3860-3866. DOI: 10.1021/acsnano.7b00144.

(115) Travis, W.; Glover, E. N. K.; Bronstein, H.; Scanlon, D. O.; Palgrave, R. G. On the application of the tolerance factor to inorganic and hybrid halide perovskites: a revised system. *Chemical Science* **2016**, *7* (7), 4548-4556, 10.1039/C5SC04845A. DOI: 10.1039/C5SC04845A.

(116) Lin, L.; Yang, L.; Du, G.; Li, X.; Li, Y.-n.; Deng, J.; Wei, K.; Zhang, J. Light soaking effects in perovskite solar cells: mechanism, impacts, and elimination. *ACS Applied Energy Materials* **2023**, *6* (20), 10303-10318.

(117) Thiesbrummel, J.; Milić, J. V.; Deibel, C.; Garnett, E. C.; Tao, S.; Kirchartz, T.; Guerrero, A.; Cameron, P.; Tress, W.; Saiful Islam, M. Ion migration in perovskite solar cells. *Nature Reviews Chemistry* **2026**, 1-17.

(118) Rodbuntum, S.; Sukgorn, N.; Chanlek, N.; Nakajima, H.; Rujisamphan, N.; Ruankham, P.; Wongratanaphisan, D.; Kaewprajak, A.; Kumnorkaew, P. Dual interfacial tin-oxide layer with chloride salt for high-performance and durable perovskite solar cells. *ACS Applied Energy Materials* **2023**, *6* (20), 10364-10375.

(119) Lee, D.-K.; Fykouras, K.; Kodalle, T.; Moral, R. F.; Schwartz, C. P.; Tamura, N.; Lawler, K. V.; Leppert, L.; Sutter-Fella, C. M. Strain engineering: Reduction of microstrain at the perovskite surface via alkali metal chloride treatment enhances stability. *ACS Energy Letters* **2025**, *10* (2), 1039-1049.

(120) Ramazanov, S.; Orudzhev, F.; Gajiev, G.; Holcman, V.; Matos, R. S.; da Fonseca Filho, H. D.; Ţălu, Ş.; Selimov, D. Local electrical characteristic of memristor structure in a high-resistance state obtained using electrostatic force microscopy: Fractal and multifractal dynamics of surface. *Applied Surface Science* **2024**, *647*, 158863. DOI: https://doi.org/10.1016/j.apsusc.2023.158863.

(121) Labuda, A.; Proksch, R. Quantitative measurements of electromechanical response with a combined optical beam and interferometric atomic force microscope. *Applied Physics Letters* **2015**, *106* (25).

(122) Labuda, A.; Hohlbauch, S.; Kocun, M.; Limpoco, F. T.; Kirchhofer, N.; Ohler, B.; Hurley, D. Tapping mode AFM imaging in liquids with bluedrive photothermal excitation. Oxford University Press: 2018.

(123) Duhamel, P.; Vetterli, M. Fast Fourier transforms: a tutorial review and a state of the art. *Signal processing* **1990**, *19* (4), 259-299.

(124) Sundararajan, D. *The discrete Fourier transform: theory, algorithms and applications*; World Scientific, 2001.

(125) Sharma, B. *Metal-semiconductor Schottky barrier junctions and their applications*; Springer Science & Business Media, 2013.

(126) Strukov, D. B.; Alibart, F.; Stanley Williams, R. Thermophoresis/diffusion as a plausible mechanism for unipolar resistive switching in metal–oxide–metal memristors. *Applied Physics A* **2012**, *107* (3), 509-518. DOI: 10.1007/s00339-012-6902-x.

APPENDIX

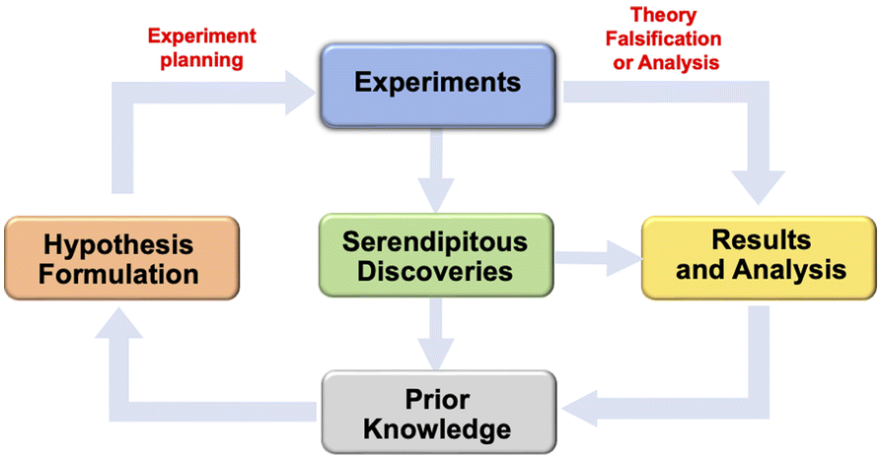


Figure 1.1: The scientific reward system shown in a diagram using prior knowledge, hypothesis formulation, experiments, results and analysis with serendipitous discoveries. Each step opens multiple pathways towards scientific discovery and can be revisited in the cycle.

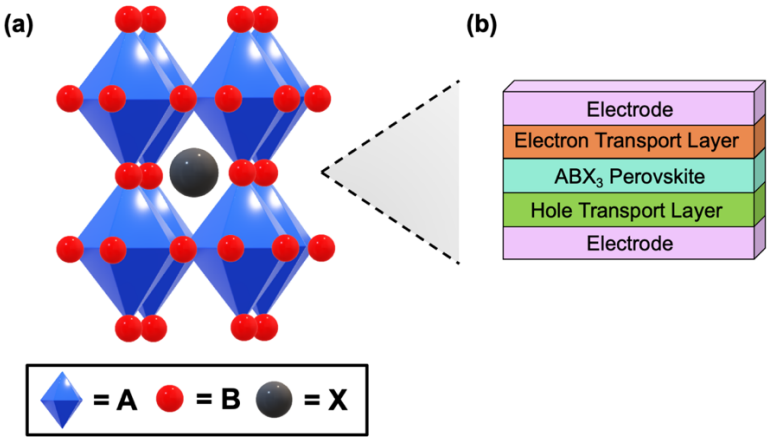


Figure 1.2: (a) 3D model showing the ABX_3 perovskite structure highlighting the positions of the A, B, and X ions. (b) An example of a perovskite thin film where the perovskite layer is sandwiched between a hole transport layer (HTL) and electron transport layer (ETL) in which electrodes are attached to send current through the film. An example of commonly used HT'Ls and ETL's are PEDOT:PSS and SnO_2 respectively.

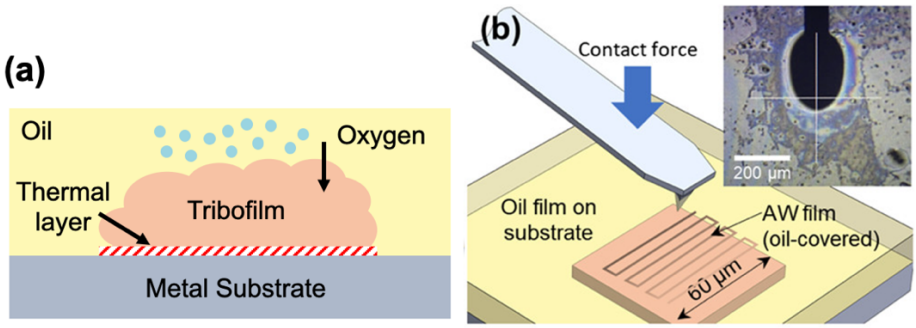


Figure 1.3: A schematic walkthrough of forming tribofilms through friction force contact via an atomic force microscope (AFM). (a) Diagram showing formation of tribofilm from thermal layer and oxygen exposure. (b) An AFM tip applies a contact force to the oil film growing the tribofilm during scanning, (b inset) optical AFM image showing tip in contact with oil.

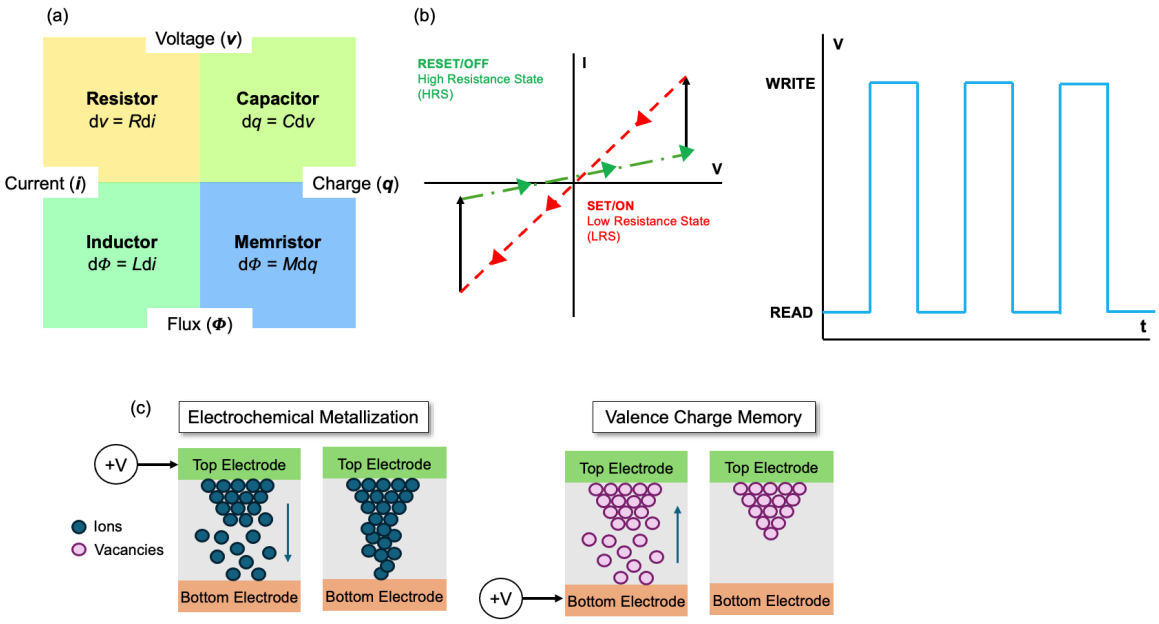


Figure 1.4: (a) A diagram showing the relationship of resistance, capacitance, induction, and memristive behavior with the respective components that make-up of a circuit. (b) An example of the butterfly curve of a memristor material switching between a high resistance state and low resistance state. Additionally, this switching is driven by a voltage waveform that pulses between a write and read voltage to verify if a resistance is maintained after removing the external stimuli. (c) A schematic showing the differences between two types of resistive switching: electrochemical metallization and valence charge memory.

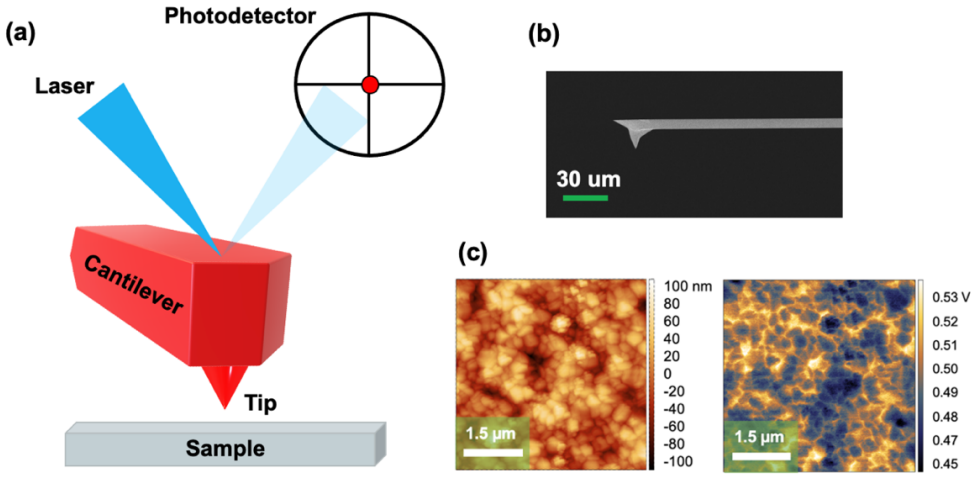


Figure 1.5: (a) A 3D model displaying the concept of an atomic force microscope (AFM). (b) A scanning electron microscope (SEM) image of an AFM tip. (c) Example images from AFM showing topography (left) and contact potential (right) in a metal-halide perovskite thin film.

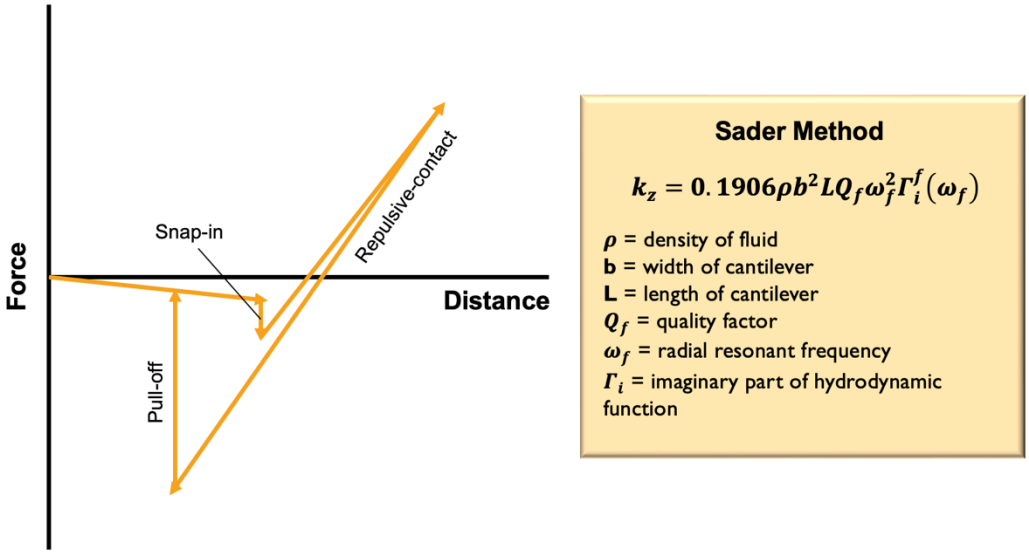


Figure 1.6: A graph showing the concept of a force-distance curve taken when calibrating and AFM tip. The Sader Method is a popular method for calculating a more accurate spring constant value for an AFM tip.

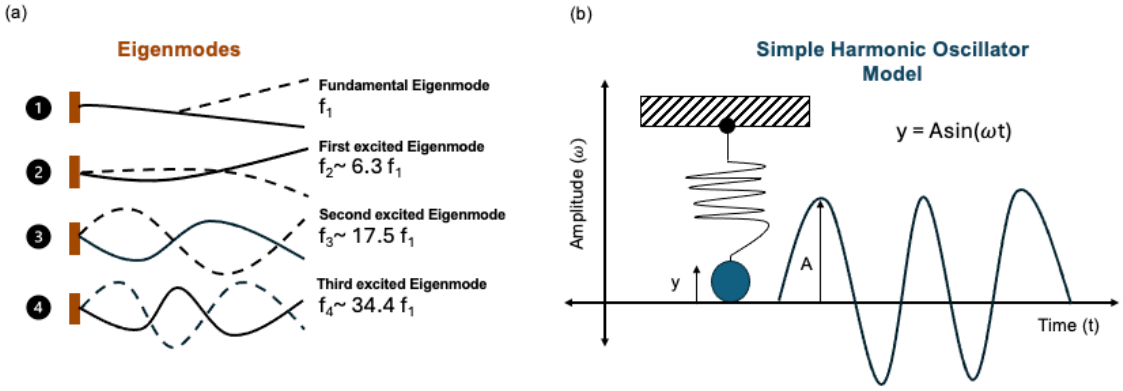


Figure 1.7: (a) A diagram that represents the four eigenmodes achieved by oscillation of a cantilever at different frequencies. The solid line and dashed line represent to different paths of movement. (b) The simple harmonic oscillator model demonstrating changes in amplitude over time to a spring attached to a ball on when end and fixed surface on the other.

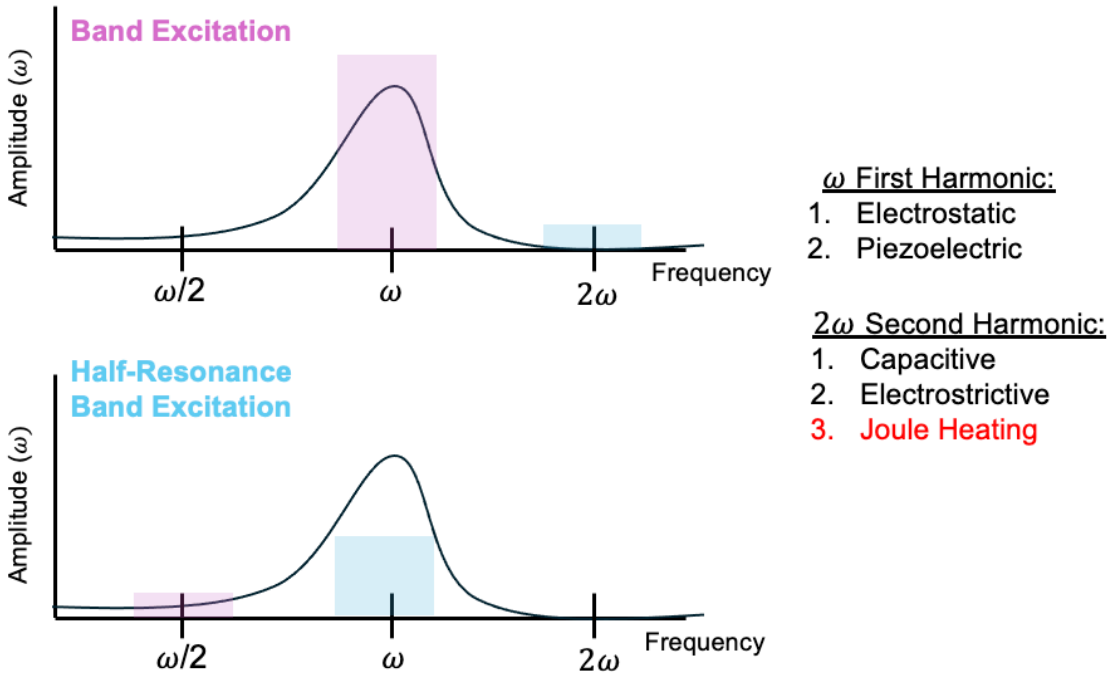


Figure 1.8: Plots showing the differences between band excitation and half-resonance band excitation methods. The first harmonic signal (ω) shows the changes in electrostatics and piezoelectricity at the tip/surface junction. Meanwhile, the second harmonic signal (2ω) demonstrates the capacitive, electrostrictive, and joule heating effects. For the band excitation method, frequency is driven and measured on the first harmonic which amplifies the signal at ω. To amplify the second harmonic frequency or 2ω in half-resonance band excitation, the driving frequency is halved which shift the amplification to the measurement window of ω.

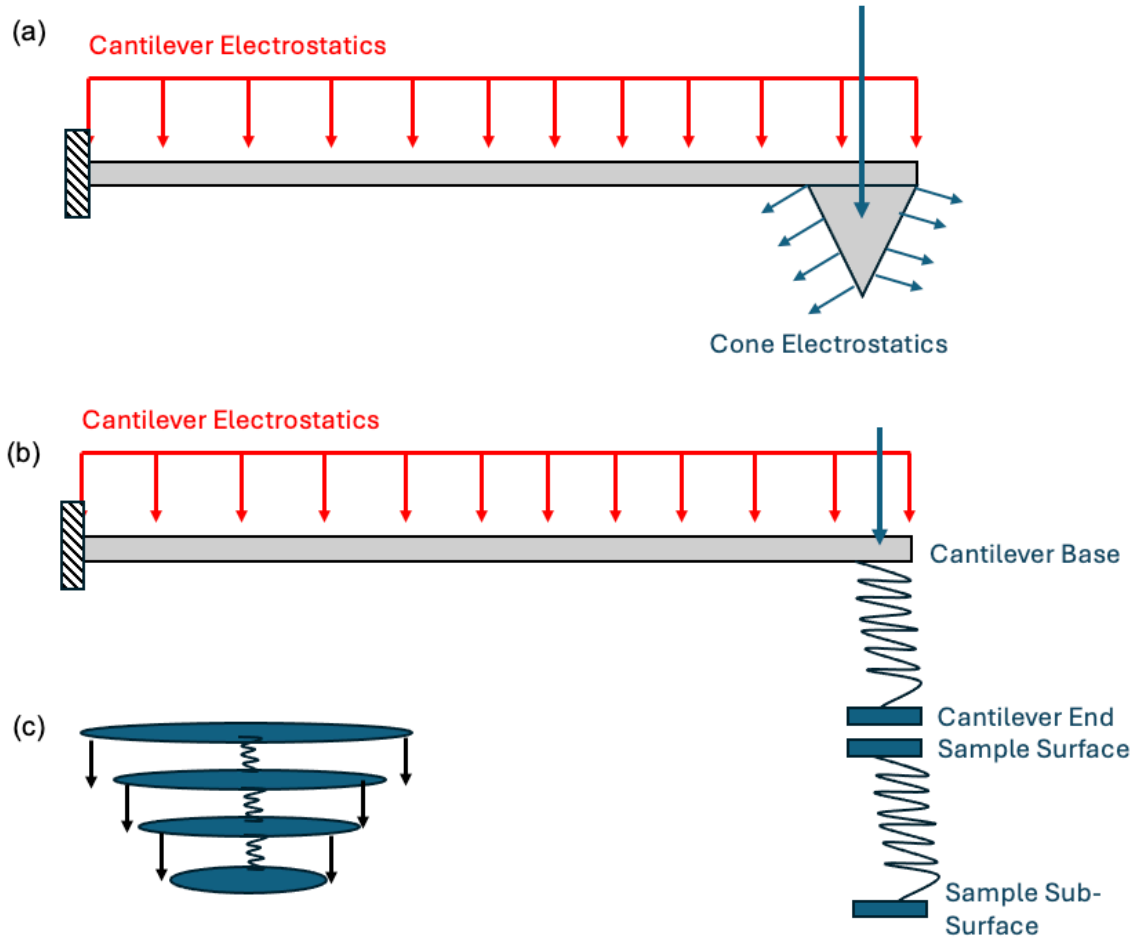


Figure 1.9: (a) A standard schematic showing the distribution of forces acting on a cantilever and cone or tip through electrostatics. (b) An alternative schematic for viewing electrostatics on a cantilever with the perspective of the tip acting as a parallel plate capacitor joined by springs. This schematic also considers the force pushing against the tip from the material surface and how that effects the tip/surface junction. (c) A close-up drawing of what can be considered for electrostatic movement of the AFM cone or tip.

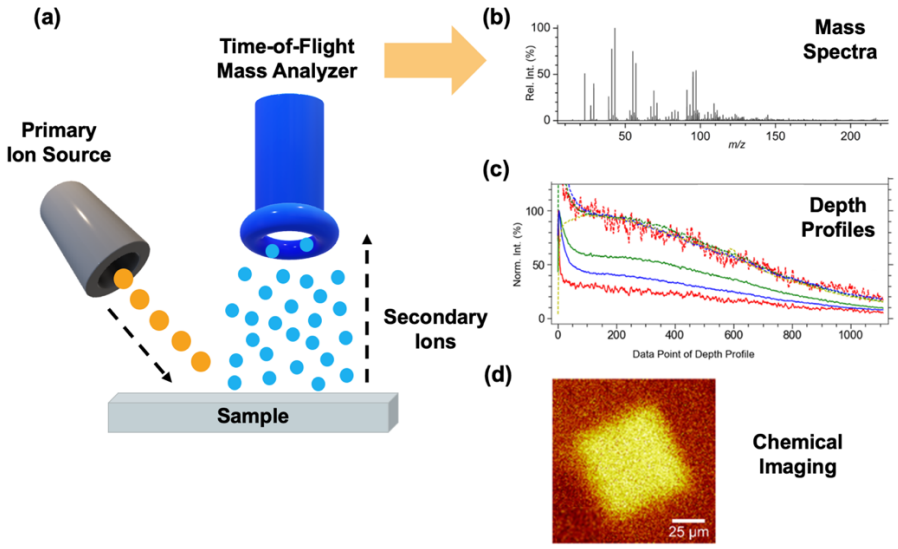


Figure 1.10: (a) A 3D ToF-SIMS model showing how through a primary ion source, secondary ions are sent to a ToF mass analyzer to study the (b) mass spectra, (c) depth profile, and (d) chemical image of a given sample in positive or negative ion mode.

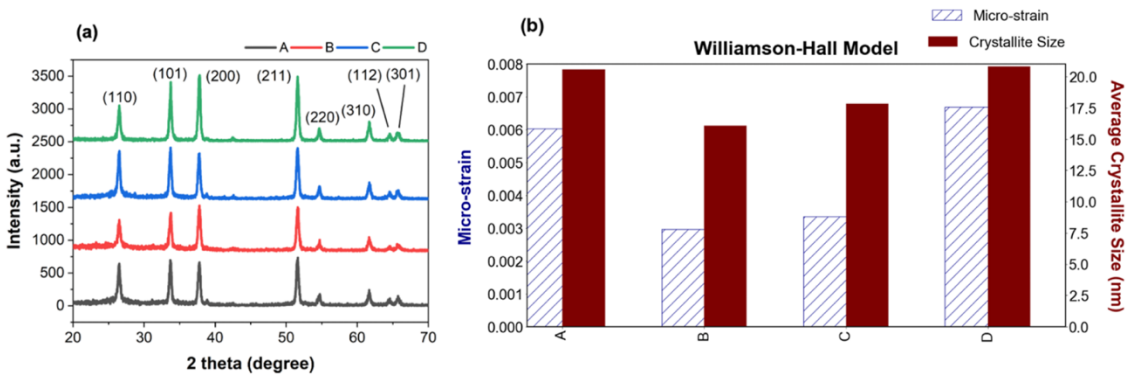


Figure 2.1: (a) X-ray diffraction patterns (XRD) of bare tin oxide substrates of films A-D. (b) A bar graph featuring the results of the Williamson-Hall plot analysis with the micro-strain (striped) and average crystallite size (solid).

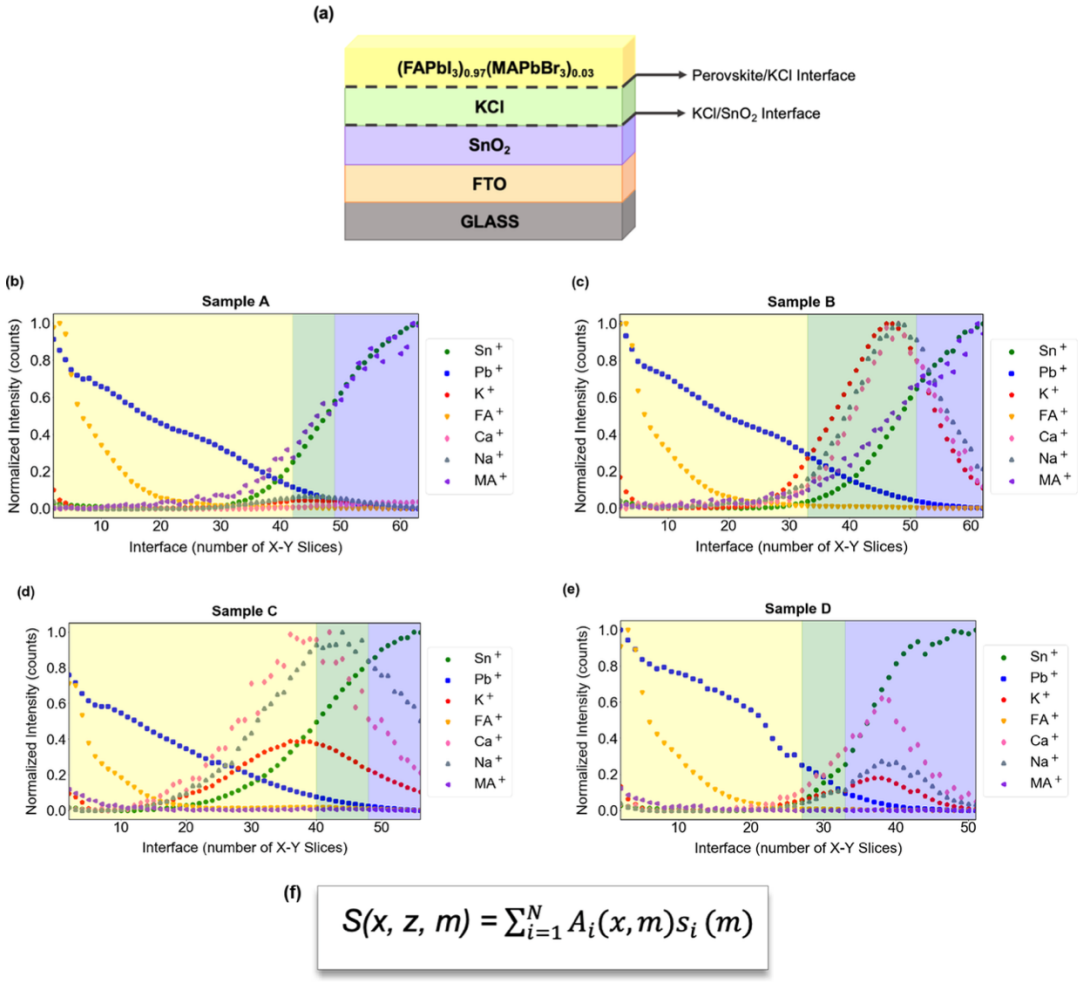


Figure 2.2: (a) A schematic of the film, showing two interfacial regions of interest: perovskite/potassium chloride (KCl) interface and KCl/tin oxide (SnO_2) interface. (b-e) Depth profiles of all films in positive ion mode, showing ion distribution throughout each of the color indicated layers: perovskite (yellow), KCl (green), and SnO_2 (blue). (f) Non-negative Matrix Factorization (NMF) equation used to derive mass spectrometry components for each film layer.

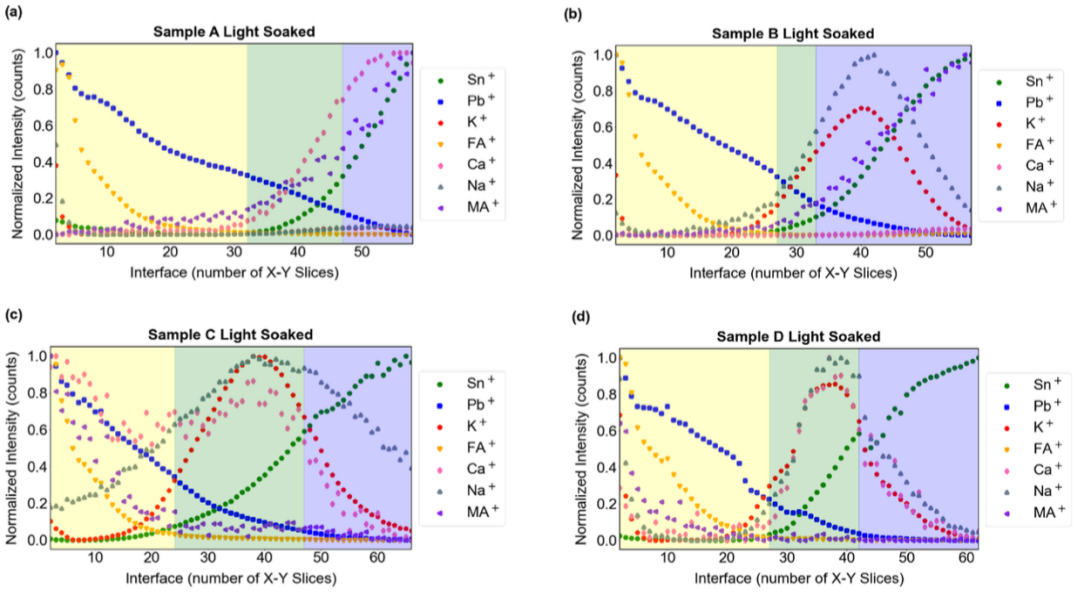


Figure 2.3: (a-d) Depth profiles of light-soaked films showing ion distribution at each interface in positive ion mode. Each color regions represents a layer: perovskite (yellow), potassium chloride (green), and tin oxide (blue).

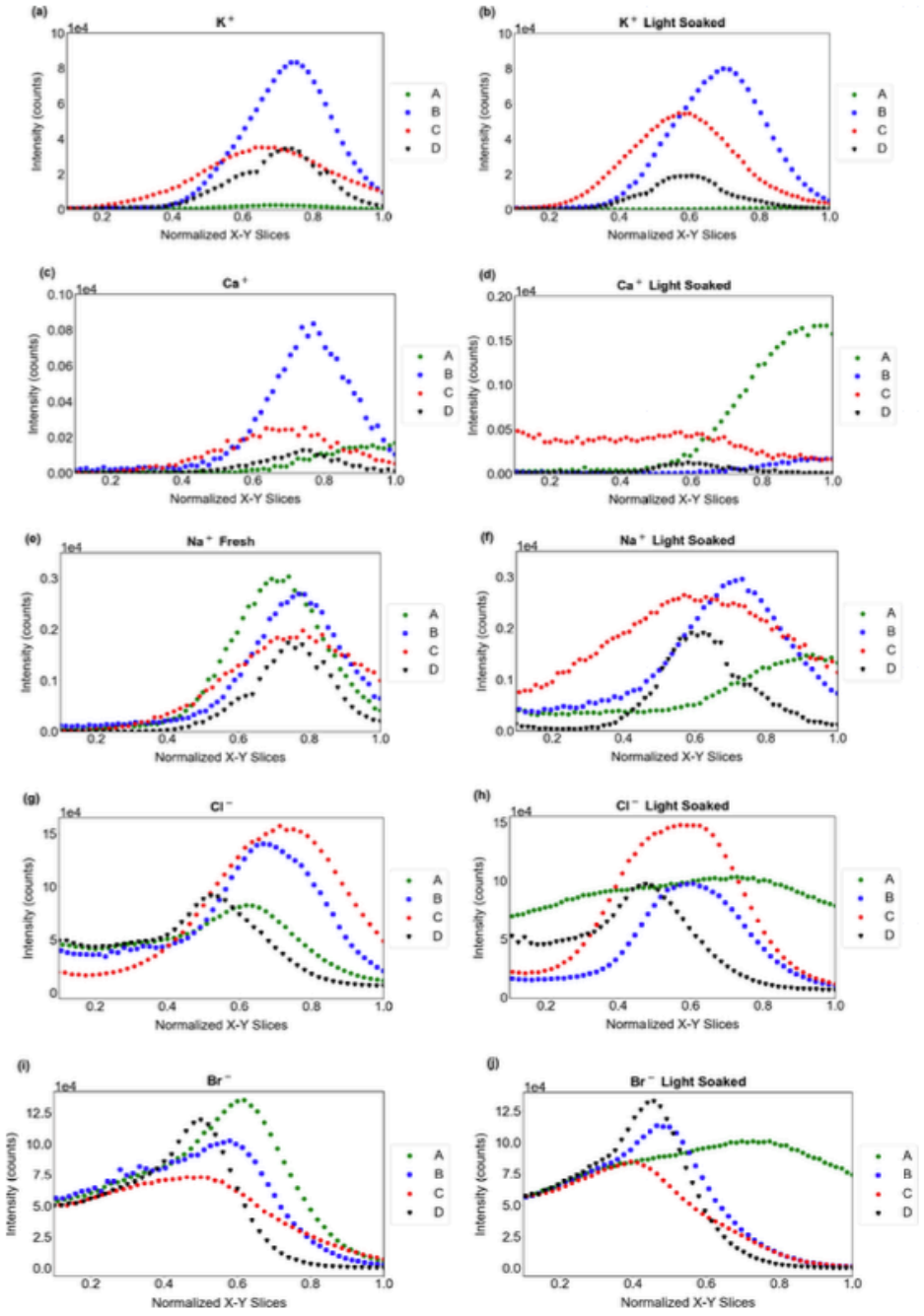


Figure 2.4: (a-j) Depth profiles of individual ions (potassium (K^+), calcium (Ca^+), sodium (Na^+), chlorine (Cl^-), and bromine (Br^-)) in both positive and negative ion modes, comparing films before and after light soaking. All plots are normalized to compare directly with one another, regardless of the intensity of counts.

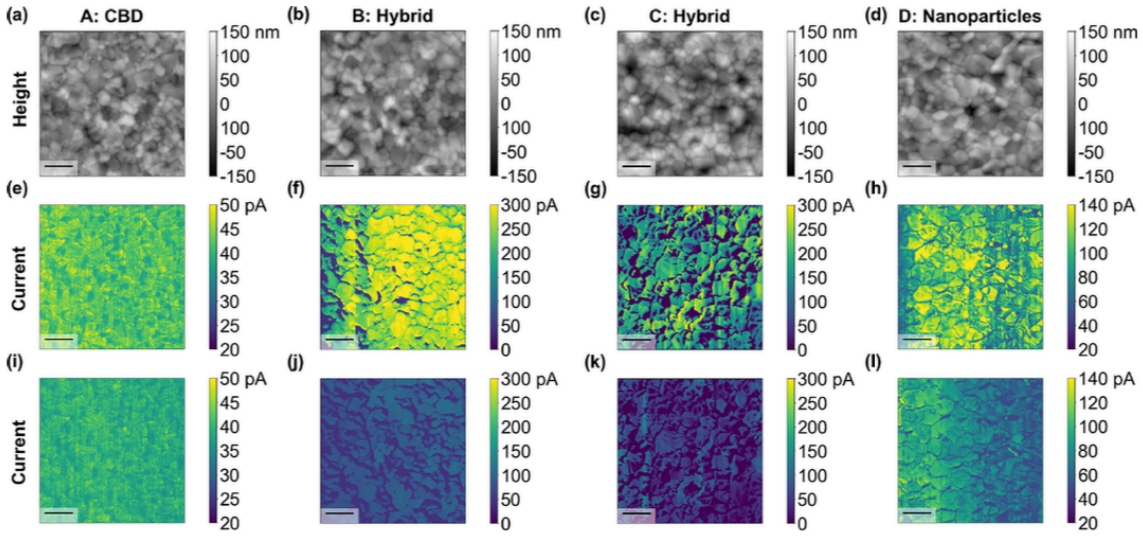


Figure 2.5: (a-d) Height images of all films demonstrating their surface morphology and their corresponding current maps under illumination (e-h) and in dark (i-l). The scale bar is 2 microns, and the duration of each scan is 12 minutes, switching the optical light on and off in-between scans.

Table 3.1: A Summary of Methods used for Antiwear Tribofilms

	AFM Single Asperity Generated Film				**Block-on-Ring Generated Film**			
	AFM Topography	Friction Force Microscopy	Nano-IR	ToF-SIMS	AFM Topography	Friction Force Microscopy	Nano-IR	ToF-SIMS
DOHP	X	X	X					X
DOHP + Ca	X	X	X	X				X

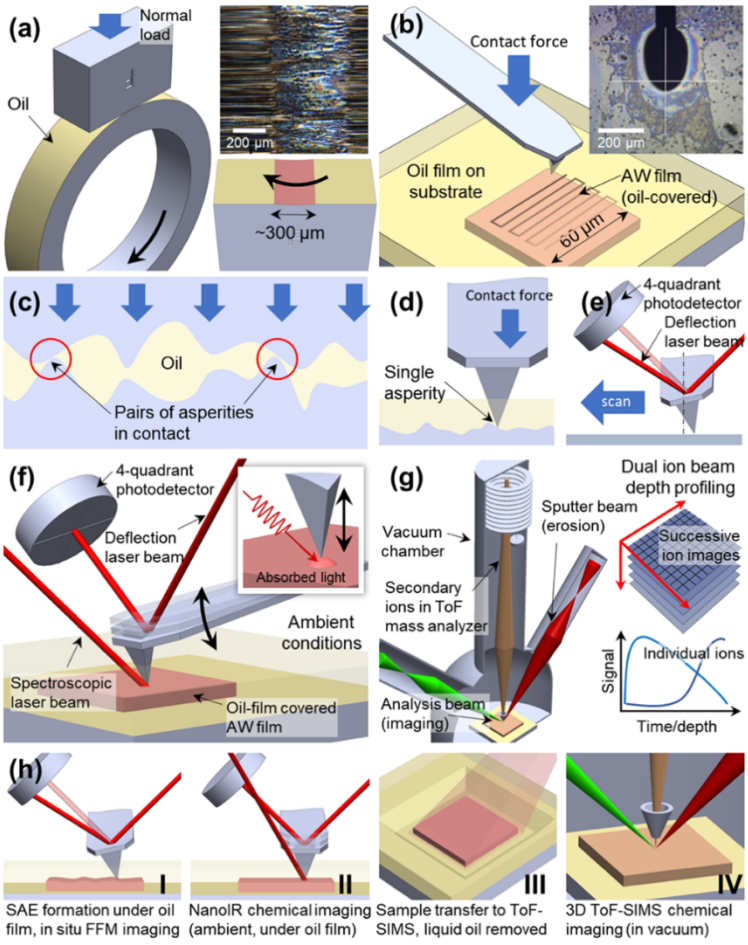


Figure 3.1: Schematics that showcase all the instrumentation methods used to study the antiwear tribofilms. (a) The block-on-ring (BoR) test used to generate a tribofilm simulating industry conditions. (b) The atomic force microscope (AFM) friction force microscopy (FFM) method to raster scan in the same area to form the tribofilm. Additionally, an image capture shows the AFM tip submersed in oil. (c) Visual aid that shows how the tribofilm is created across the BoR. (d) A schematic featuring how the force applied by the AFM tip while scanning generates a tribofilm. (e) The AFM Nano-IR probe scanning across the film to measure topography, friction, and IR wavelengths simultaneously. (f) A more in-depth diagram showing the functionality of the Nano-IR experiment set-up. (g) The time-of-flight secondary ionization mass spectrometer (ToF-SIMS) used for depth profiling. (h) Series of steps conducted to develop the tribofilm and then measure in the ToF-SIMS.

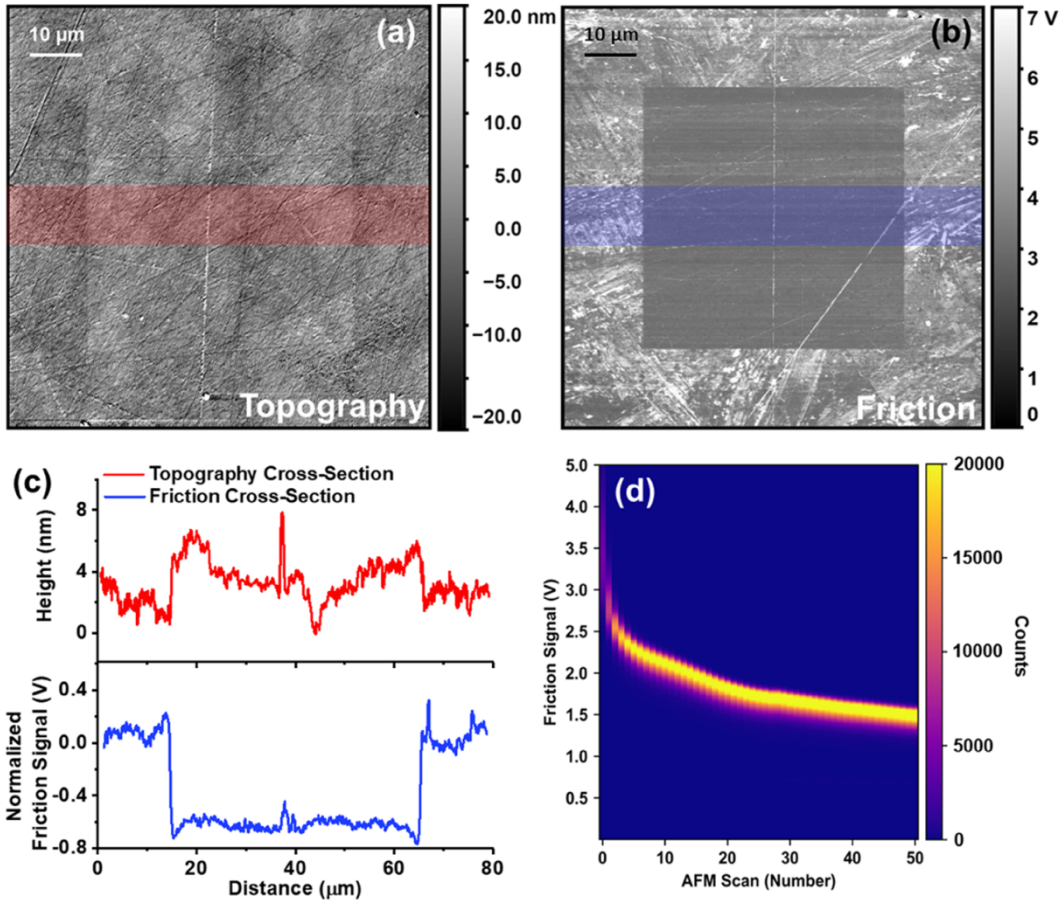


Figure 3.2: The height (a) and friction (b) image of the antiwear (AW) tribofilm formed on a steel surface in the atomic force microscope (AFM), friction force microscopy (FFM) measurement. The tribofilm formed is DOHP and calcium in base oil. (c) Plots of the corresponding cross-sectional regions are shown for topography or height (red) and friction (blue) to show the transition across regions of oil-treated surface and non-treated. (d) An additional plot is provided to demonstrate the magnitude of the friction signal, as a function of scans for all points in the 50x50 microns scanning area.

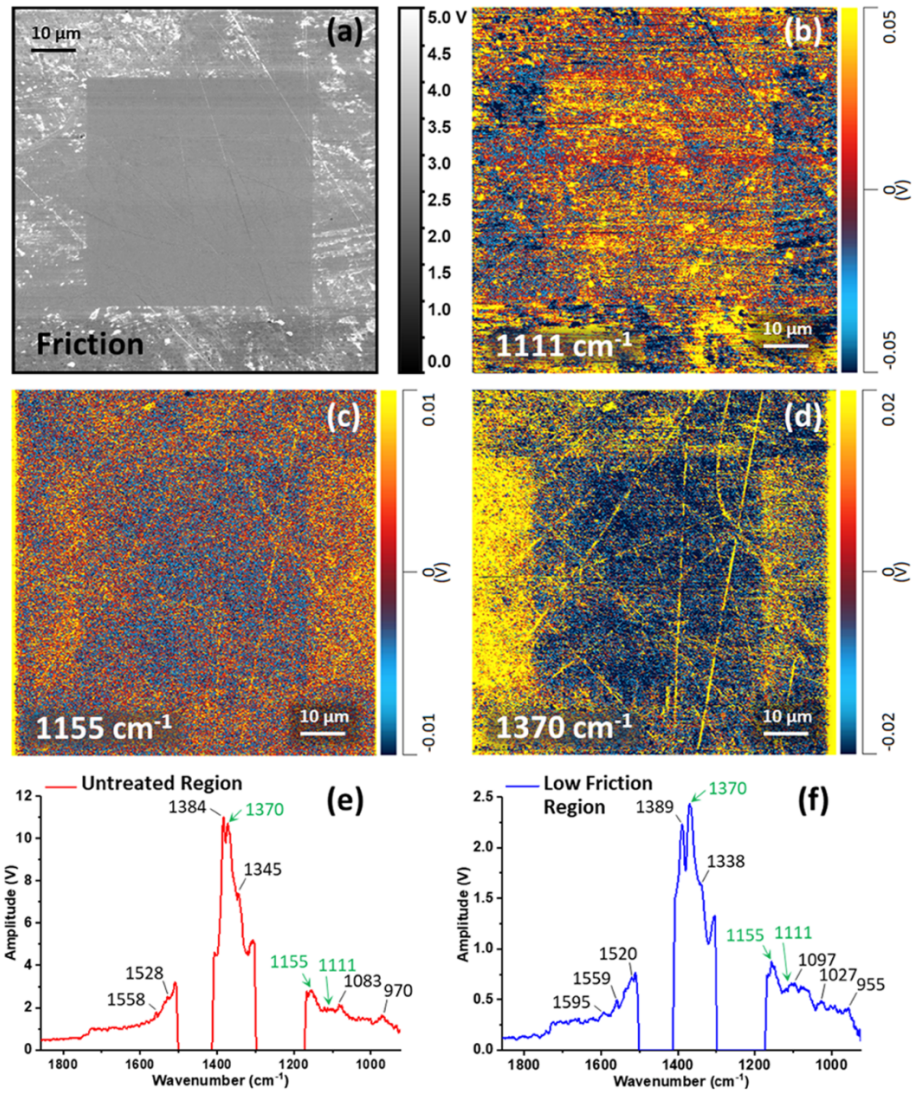


Figure 3.3: An *in situ* analysis of AW film formed under FFM in the AFM Nano-IR for DOHP with calcium in base oil. All films featured are not the same film, since the timescale of degradation is small. A friction map (a) and chemical maps are shown to emphasize the following absorption wavenumbers (b) 1111 cm^{-1} (c) 1155 cm^{-1} and (d) 1370 cm^{-1}. Absorption spectra is shown in multiple wavenumber ranges for the untreated (e) and treated (f) regions of the film. The spectra plots are smoothed with the five-point Savitzky-Golay method and averaged every 20 points.

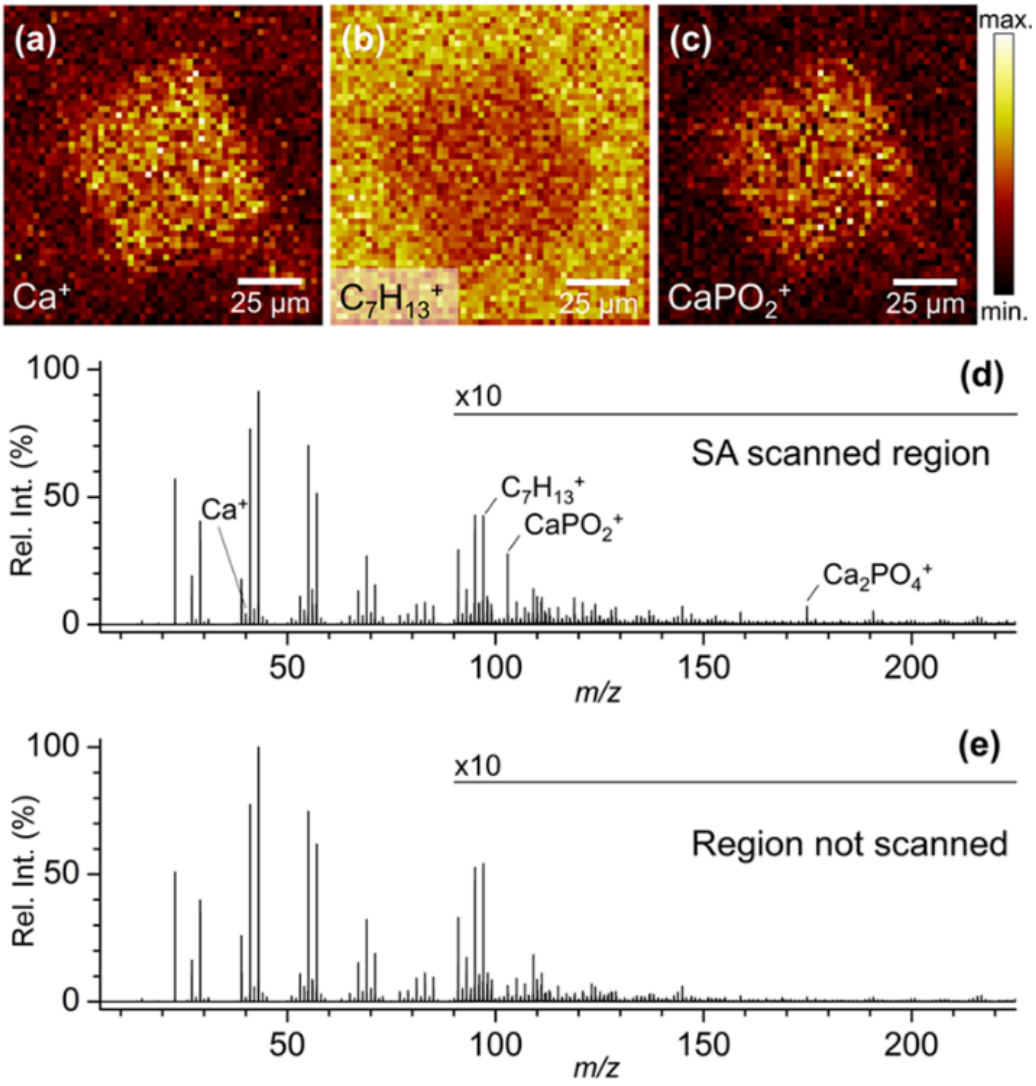


Figure 3.4: A ToF-SIMS surface image collected on the single asperity (SA) area on stainless steel for DOHP and calcium additives in base oil, after rinsing remaining oil with hexane. (a-c) Positive ion maps show the distribution of calcium (Ca^+), $C_7H_{13}^+$, and $CaPO_2^+$. Mass spectra that is normalized and averaged is shown highlighting many ions of interest for the SA region (d) and surrounding area (e).

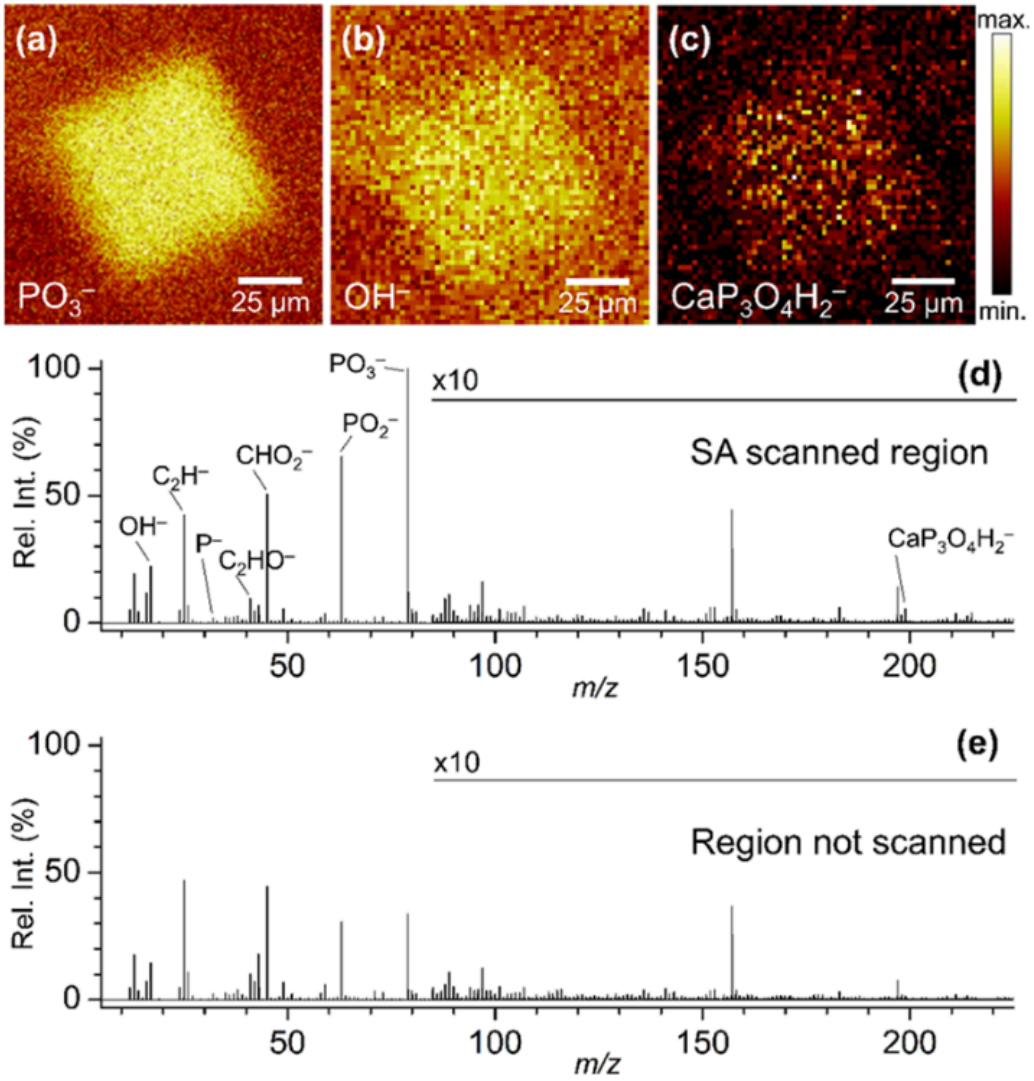


Figure 3.5: A ToF-SIMS surface image collected on the single asperity (SA) area on stainless steel for DOHP and calcium additives in base oil, after rinsing remaining oil with hexane. (a-c) Negative ion maps show the distribution of phosphite (PO_3^-), hydroxide (OH^-), and $CaP_3O_4H_2^-$. Mass spectra that is normalized and averaged is shown highlighting many ions of interest for the SA region (d) and surrounding area (e).

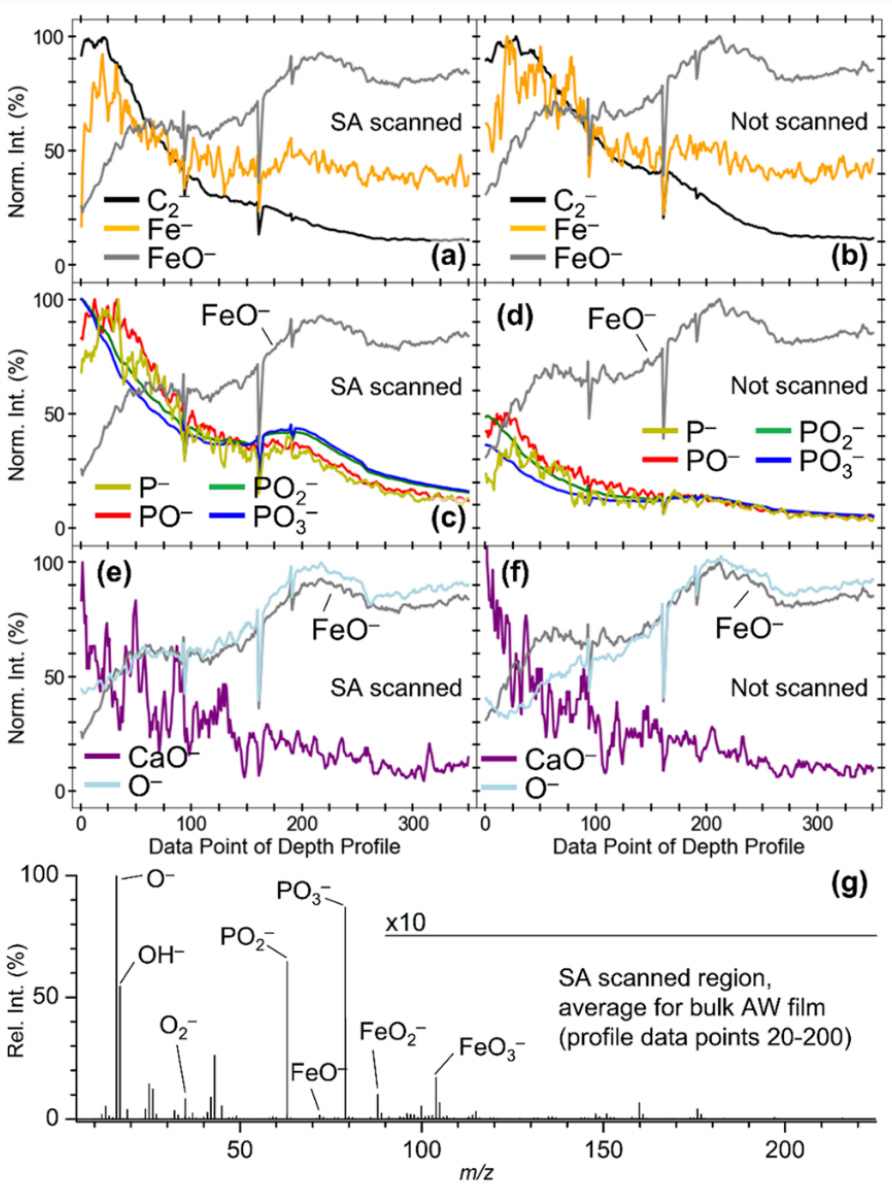


Figure 3.6: ToF-SIMS depth profiling plots for the SA AW films formed in DOHP and calcium additives in base oil, after rinsing with solvent. (a, c, e) Demonstrate the treated regions and (b, d, f) non-treated regions for comparison. Profiles are normalized in scaling by their ions of interest: (a, b), (c, d), and (e, f). (g) An averaged mass spectra is shown for the bulk AW film inside the SA region. Spectral intensities in (a) and (d) have been corrected for instrument sensitivity.

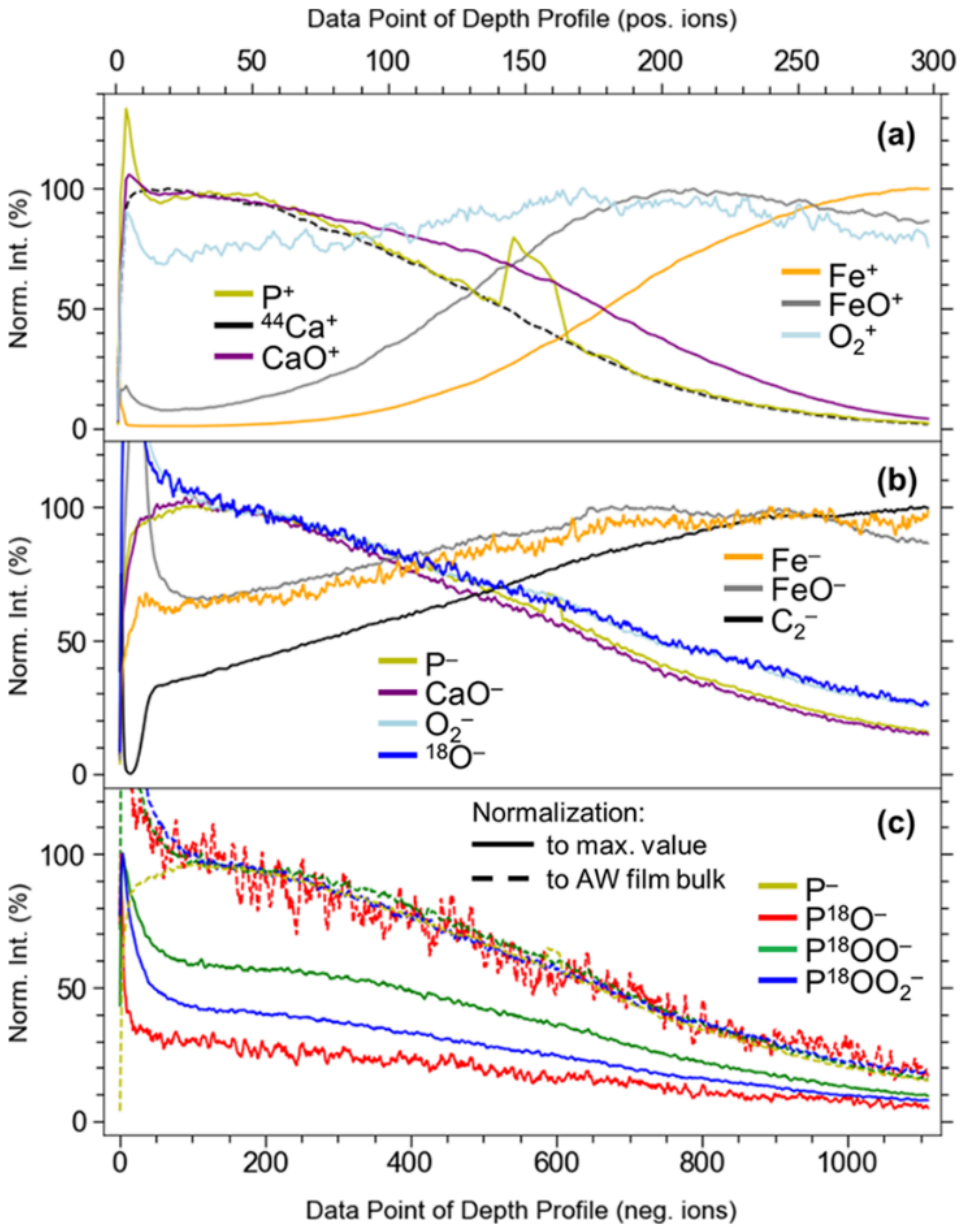


Figure 3.7: ToF-SIMS depth profiles for the block on ring (BoR) with DOHP and calcium additives in base oil, combining two separate experiments of (a) positive (b, c) and negative ions. Each plot is normalized to the maximum intensity in the bulk AW film, omitting intensity spikes in the top surface layer.

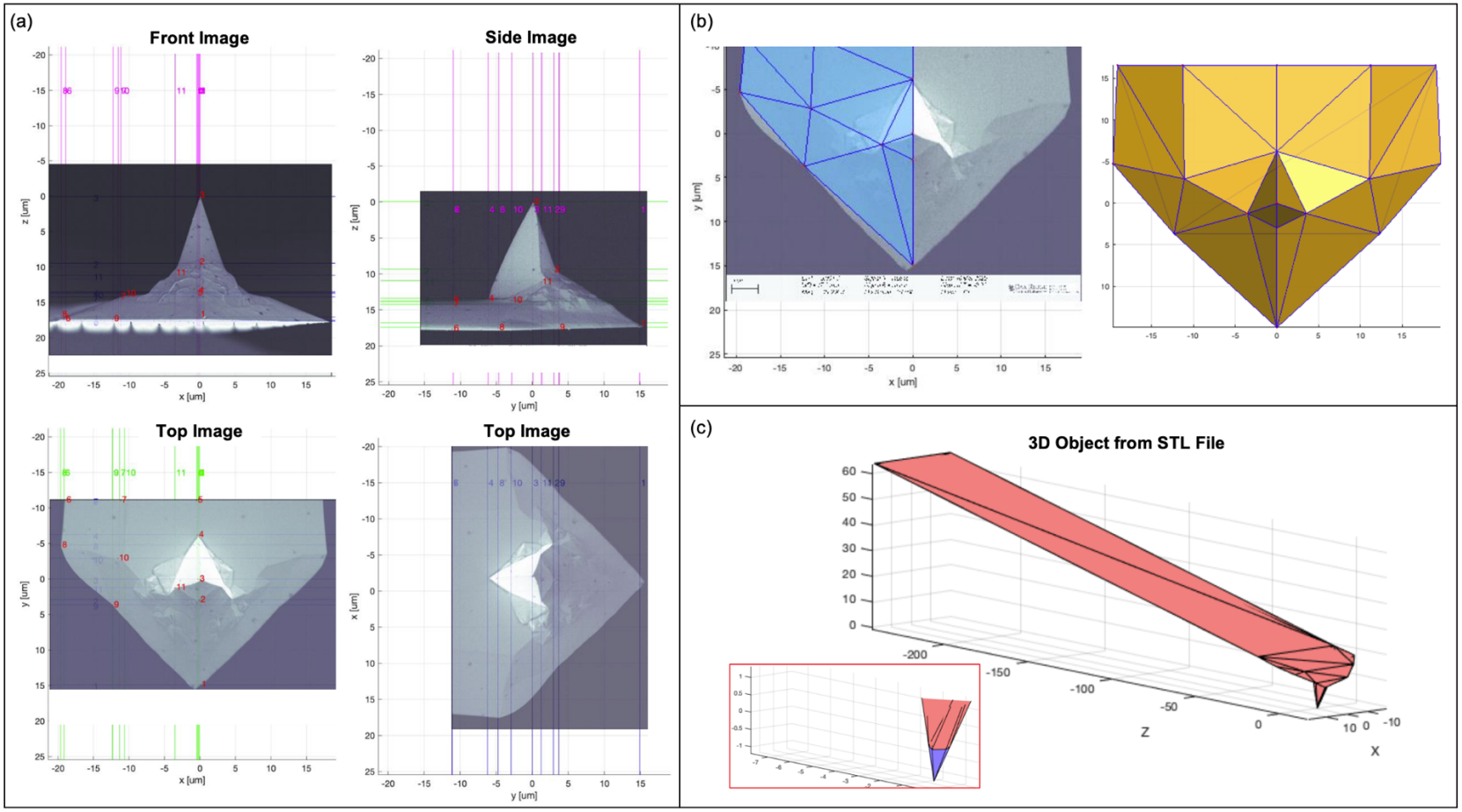


Figure 4.1: (a) The series of SEM images used to capture the geometry of the AFM tip, loaded into the MATLAB interface for users to select locations of vertices. (b) The triangular face selection phase and resulting geometry built of the AFM tip. (c) The last step in the process, truncating the AFM tip and producing a computer aided design (CAD) model for COMSOL. A Budget Sensors Multi 75E-G tip is used for this example.

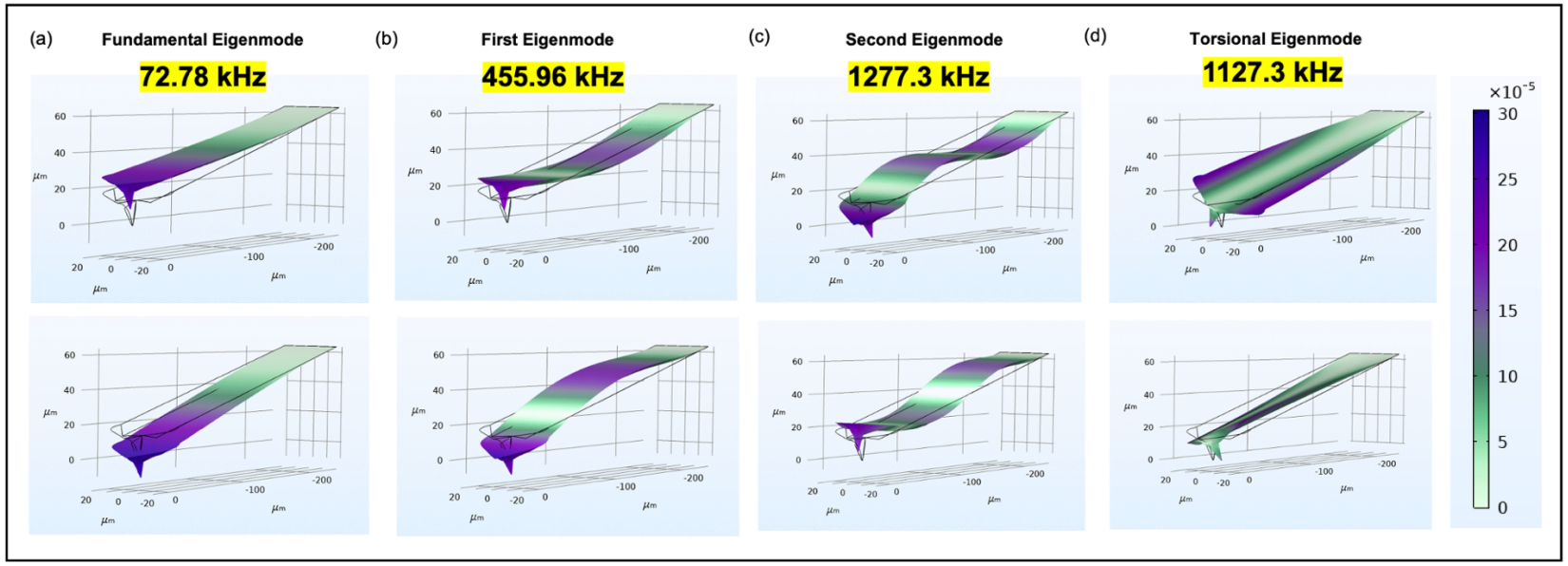


Figure 4.2: COMSOL 3D simulation of mechanical bending modes of a Budget Sensors Multi75E-G AFM Probe, with nominal geometric parameters of 225 mm length, 28 mm width and 3 mm thick, and a force constant of 3 N/m. The images show the bending modes corresponding to the two limit deformations in up and down direction for the resonances associated to the (a) fundamental eigenmode, (b) first eigenmode and (c) second eigenmode. Additionally, a (d) torsional eigenmode is shown with its deformation in the left and right direction. The color bar of the 3D COMSOL model represents the maximum amplitude of oscillation of each point of the cantilever surface under the resonant mechanical deformation. The areas in white correspond to nodes of the bending modes, that is, quasistatic areas of the cantilever that suffer no z-displacement during the oscillation at the resonance. The resonance frequencies highlighted in yellow associated to each mode were calculated from the model during the eigenfrequency study in COMSOL.

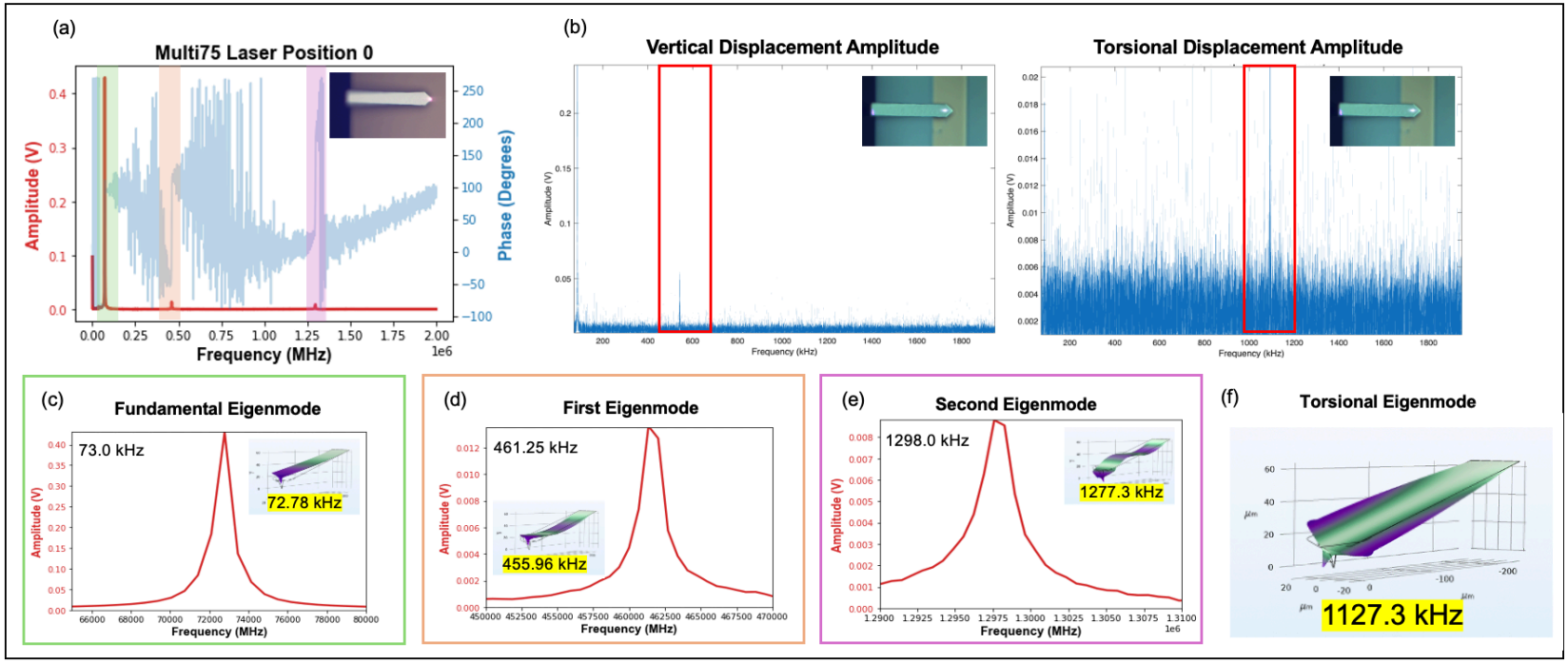


Figure 4.3: (a) Plot of experimental data of cantilever oscillation amplitude as a function of frequency captured at laser position 0 (outermost tip location) highlighting the amplitude of the resonance peak as a function of frequency for fundamental eigenmode (c), first eigenmode (d), and second eigenmode (e), all captured with tip out of contact. (a-inset) Camera capture of laser position 0 on a Budget Sensors Multi75E-G tip. (c-f insets) Corresponding cantilever bending modes associated to each resonance obtained from the COMSOL modeling. Yellow highlighted frequencies were calculated from the model during the eigenfrequency study in COMSOL and are compared with the experimental ones for each mode. (b) Comparison of experimental data of cantilever oscillation amplitude as a function of the excitation frequency in the vertical (left) and lateral (right) directions. The peak observed in the lateral displacement amplitude corresponds to the mechanical bending mode shown in (f) depicting a torsional bending of the cantilever. Note that placing the BlueDrive laser spot off-centered favors the thermo-mechanical excitation of torsional modes.

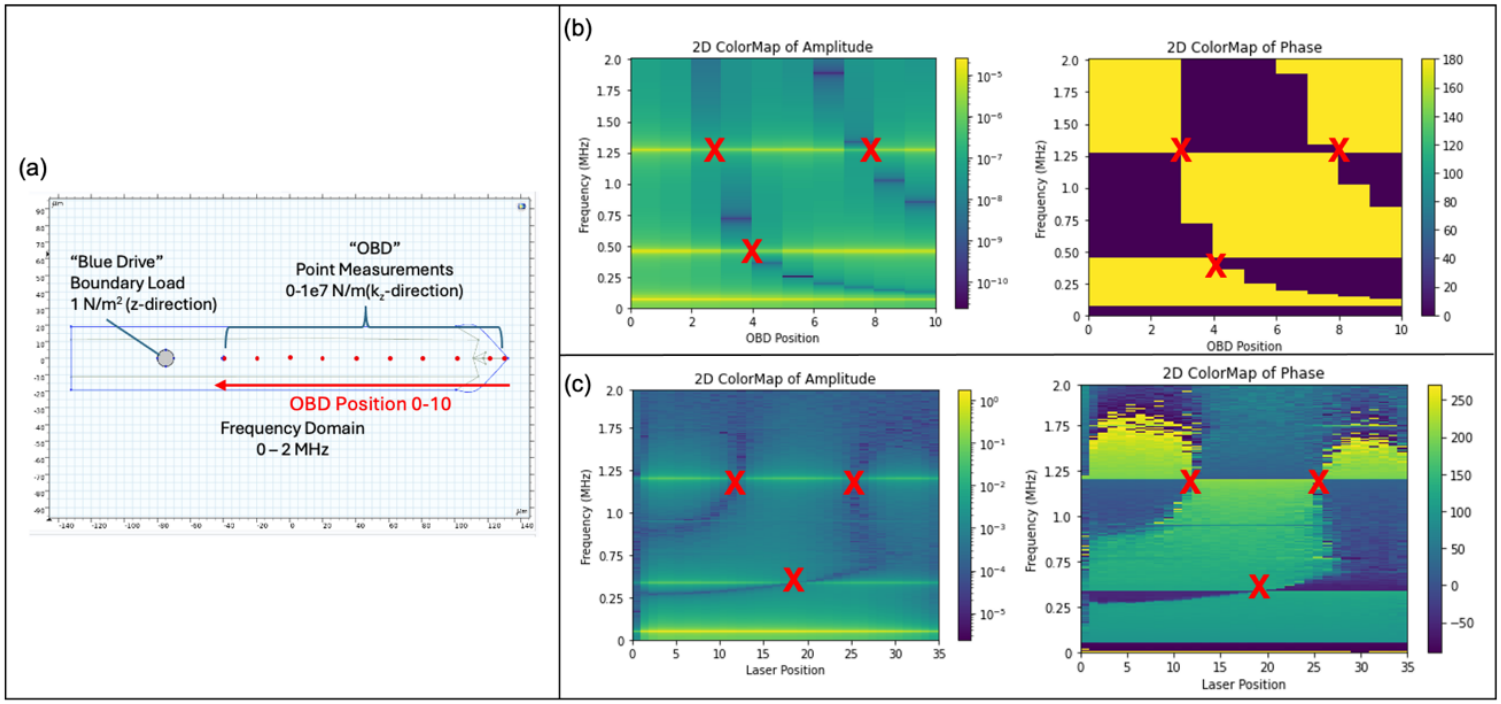


Figure 4.4: By changing the laser spot along the x-axis of a cantilever one can experimentally measure the amplitude and phase of the mechanical oscillation and compare with the data of the mechanical bending modes of a 3D cantilever structure simulated by a COMSOL. (a) Schematic showing the parameters for the parametric sweep in COMSOL to obtain a set of data to compare with experiment. Note that the laser spot here is moved from the free end towards the base of the cantilever, being the position 0 the one closer to the free end (b) 2D colormaps of amplitude and phase of the cantilever mechanical bending along the x-axis of the cantilever, for a Multi75E-G tip obtained from COMSOL simulation of a free oscillating cantilever, using $k_z = 0$ N/m (free end cantilever). (c) Experimental measurement of amplitude and oscillation of the cantilever in the vertical direction measured in an AFM by changing the laser position along the x-axis of the cantilever for a Multi75E-G tip out of contact. Note that in this case, the laser is moved from the base of the cantilever towards the free end, being the position 0 the one more distant from the free end. The red X identifies the position of the nodes of the mechanical bending modes for the different resonant modes.

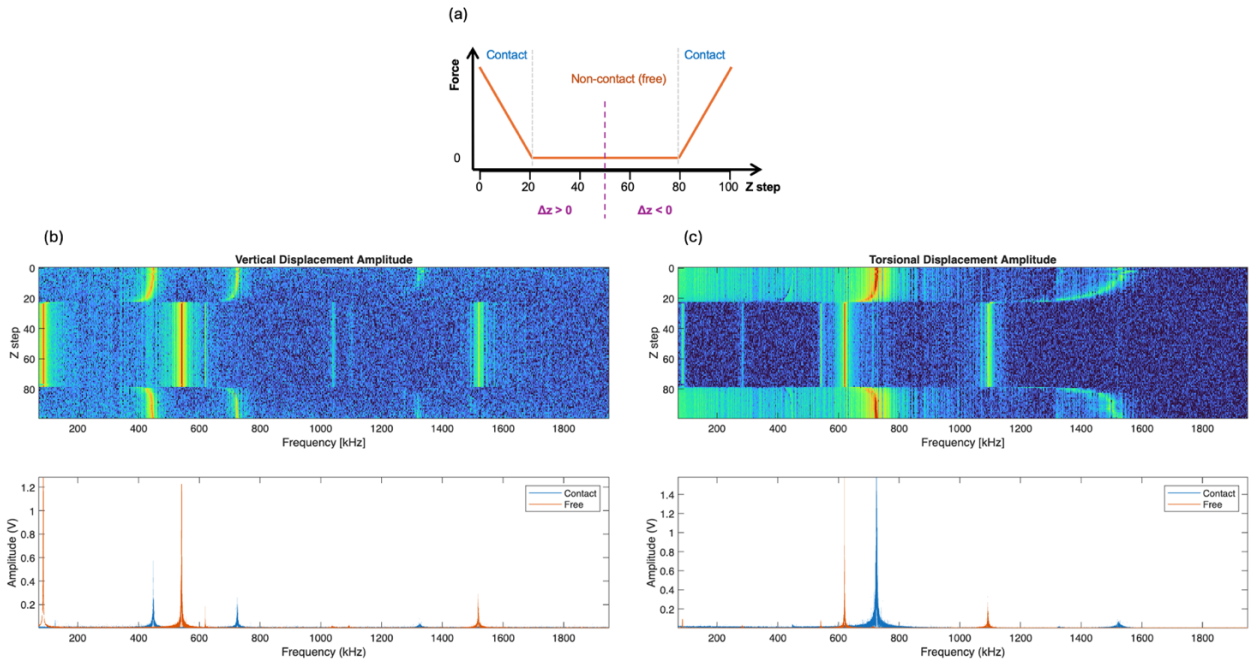


Figure 4.5: Frequency spectroscopy of the cantilever at a single laser spot as a function of the tip-sample distance in the z-axis. All measurements were conducted using a BlueDrive thermal excitation on a Multi75E-G tip. Seen in (a) the z-scan starts from a tip in contact with the surface under a force setpoint of 3V and increases the z-step until the cantilever enters the non-contact mode and resonates with a free end away from the surface. Then, the z steps are decreased back and the cantilever approaches the surface until it enters back the contact mode. At each z step the system measures the cantilever oscillation amplitude as a function of frequency in the range from 100 kHz to 2 MHz and tracks the different resonant bending modes. The spectra for the torsional and vertical displacement signals are then fitted by a SHO function. The top panel of (b-c) shows the vertical or torsional displacement amplitudes at each respective frequency peak obtained from the SHO fittings. The bottom panel of (b-c) depicts two sections of the upper graph, one corresponding to a z step where the tip was in contact with the sample (blue line) and the other one depicts the free resonances spectra of the tip while it is out of contact and away from the surface (orange line). Note that the intensity of the vertical bending signal is much higher relative to the torsional one.

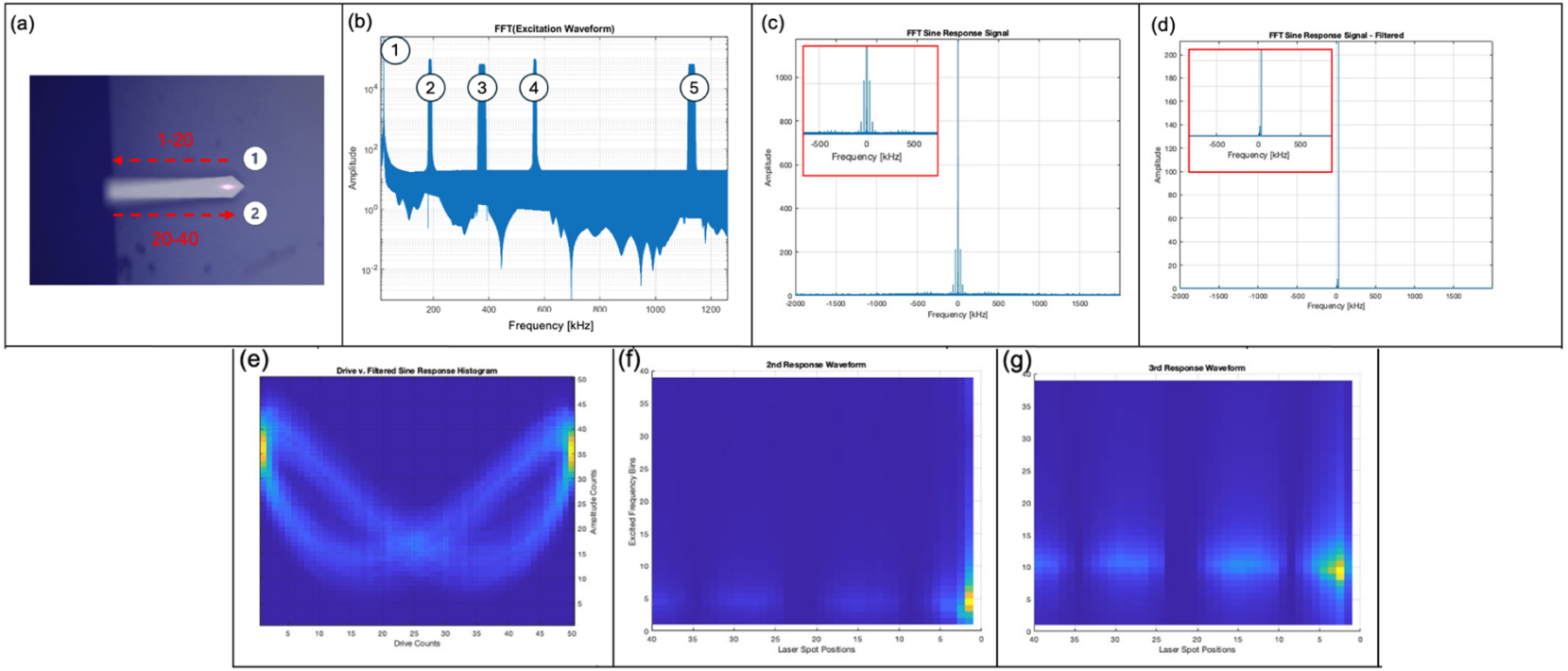


Figure 4.6: All measurements were conducted in contact with excitation to a Multi75-EG tip, and 1.0 Mohm resistor in series. (a) An image capture showing the first and second half of laser positions (#1 – 40) across the cantilever, position 1 located at the tip. (b) A plot showing the Fast Fourier transform (FFT) excitation waveform sent to the tip. Peak ranges 1-5 are as follows – sine waveform (15 kHz), band excitation (BE) waveform (179.5 – 194.5 kHz), BE waveform (359 – 389 kHz), BE waveform (557.5 – 572.5 kHz), BE waveform (1115 – 1145 kHz). (c) A plot showing the FFT of the sine response signal with frequency as a function of amplitude across the full frequency range (0 – 2 MHz). (d) A plot demonstrating the filtering process where only peaks excited at the sine waveform and its double in both positive and negative are captured. (e) A histogram featuring the filtered sine response as a function of drive signal, showing max counts for each position. (f-g) 2D maps showing the response waveform of each excited waveform region as a function of laser position.

Table 4.1: Comparing Contact Resonance Experimentally and through Modelling.

	Experiment	**1D Model**
First Vertical Eigenmode	450 kHz	405 kHz
Second Vertical Eigenmode	725 kHz	-
Third Vertical Eigenmode	1325 kHz	1133 kHz
First Torsional Eigenmode	725 kHz	673 kHz
Second Torsional Eigenmode	1525 kHz	1228 kHz

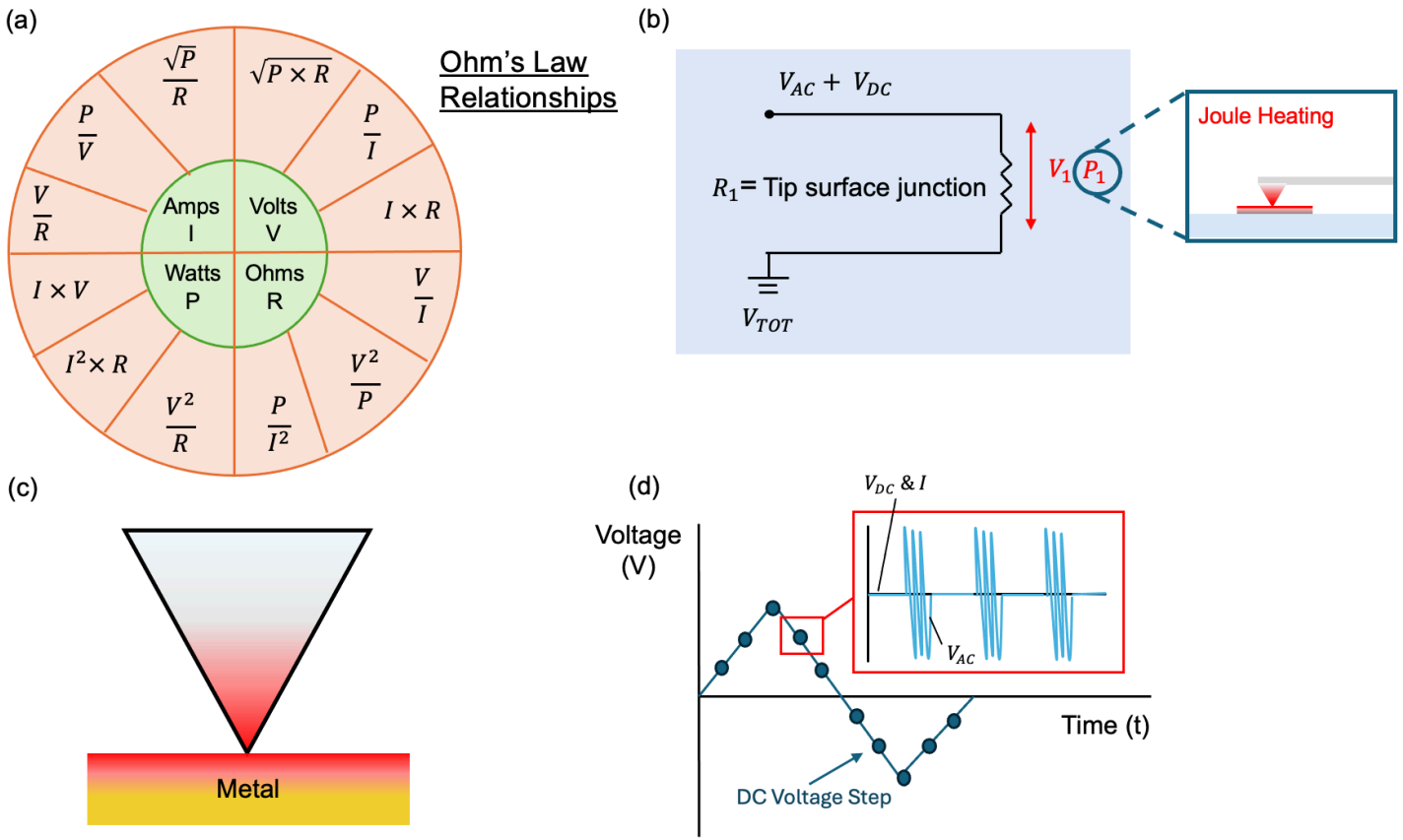


Figure 4.7: (a) A diagram of Ohm's Law relationships of current (I), voltage (V), power (P), and resistance (R). (b) A schematic of the experimental HBE setup showing the total circuit, highlighting the variables to be solved for (red). Joule heating occurs across the tip-surface junction and is equivalent toP_1. (c) A drawing showing where local heating (red gradient) can occur at the tip-surface junction. (d) The voltage waveform sent to the tip as a function of time highlighting the following parameters that can be adjusted by the user – DC voltage (V_{DC}), AC voltage (V_{AC}), and DC voltage step.

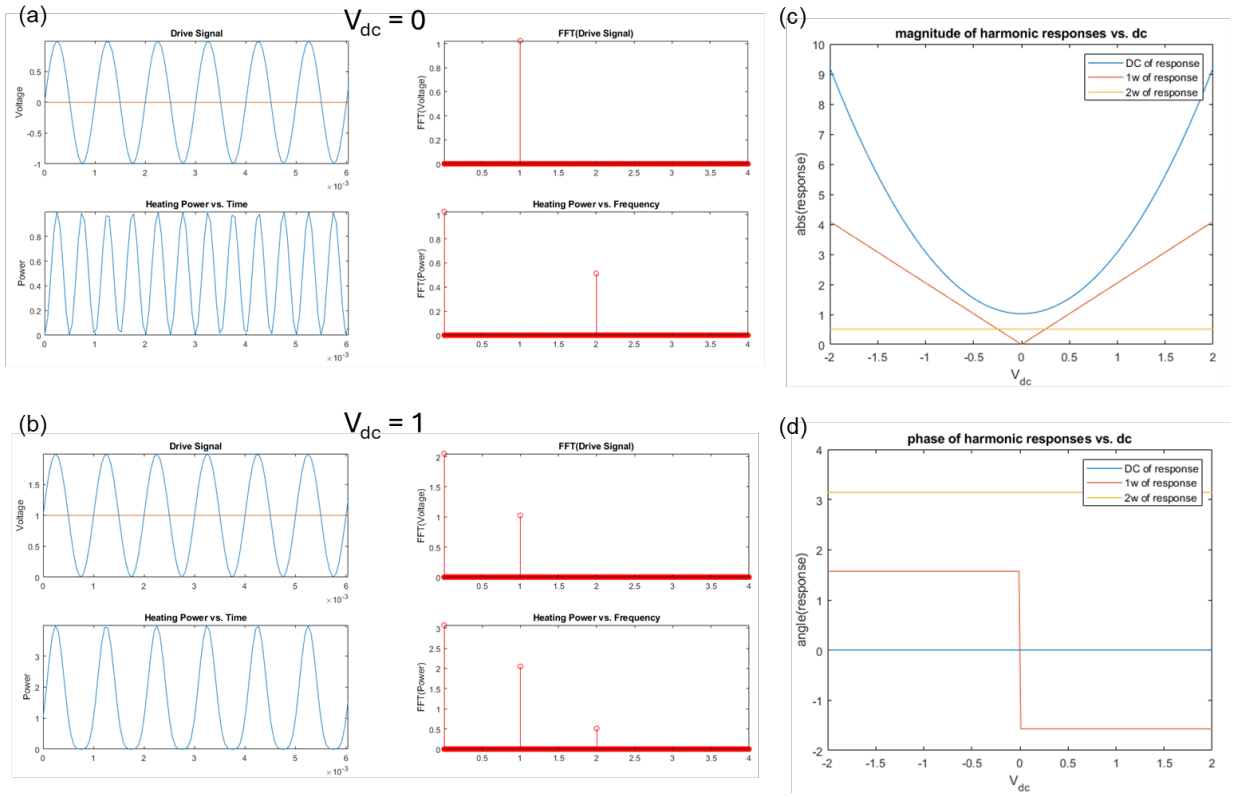


Figure 4.8: (a) Plots the time dependence of a Vac voltage (top left) and its associated Fourier transform in the frequency domain (top right), and the associated power dissipated on a resistance under such an applied voltage in both, time and frequency domain. If no Vdc voltage is applied, the thermal driving force due to Joule heating of the dissipated power at the tip -sample junction has only a 2w component. However, when a Vdc voltage is included as shown in (b), the power dissipated can be split into two components, at the w and 2w harmonics. (c) Evolution of the magnitude of the different harmonics of the power dissipated as a function the Vdc and associated phase shown in (d).

(a)

$$A_{PR,\omega} = \left(d + \frac{C_{cant}'}{k_{cant}}\right) V_0$$

d = piezoelectric coefficient of ferro film
V_0 = amplitude of driving bias
K_{cant} = spring constant of cantilever
C_{cant} = cantilever-sample capacitance

$$A_{PR,2\omega} = MV_0^2 + \beta\frac{RI_0^2}{2} + \frac{C_{cant}'}{4k_{cant}}V_0^2$$

M = electrostrictive coefficient
B = Joule heat transduction coefficient
R = capacitor electrical resistance
I_0 = amplitude of capacitor current

(b)

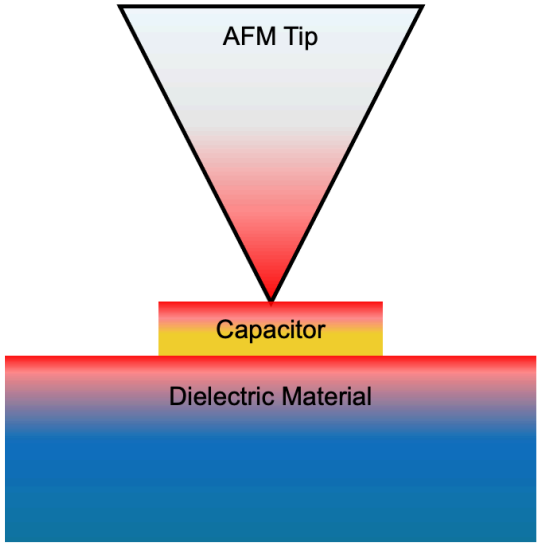


Figure 4.9: The half-resonance band excitation method derived from a work involving conductive AFM of metallic caps on BFO. (a) Equations for the first and second harmonic amplitudes and the variables considered for the origin of the signal measured. (b) A schematic showing potential heating locations (red gradient) located between the tip and capacitor, as well as potential heating occurring beneath the electrode.

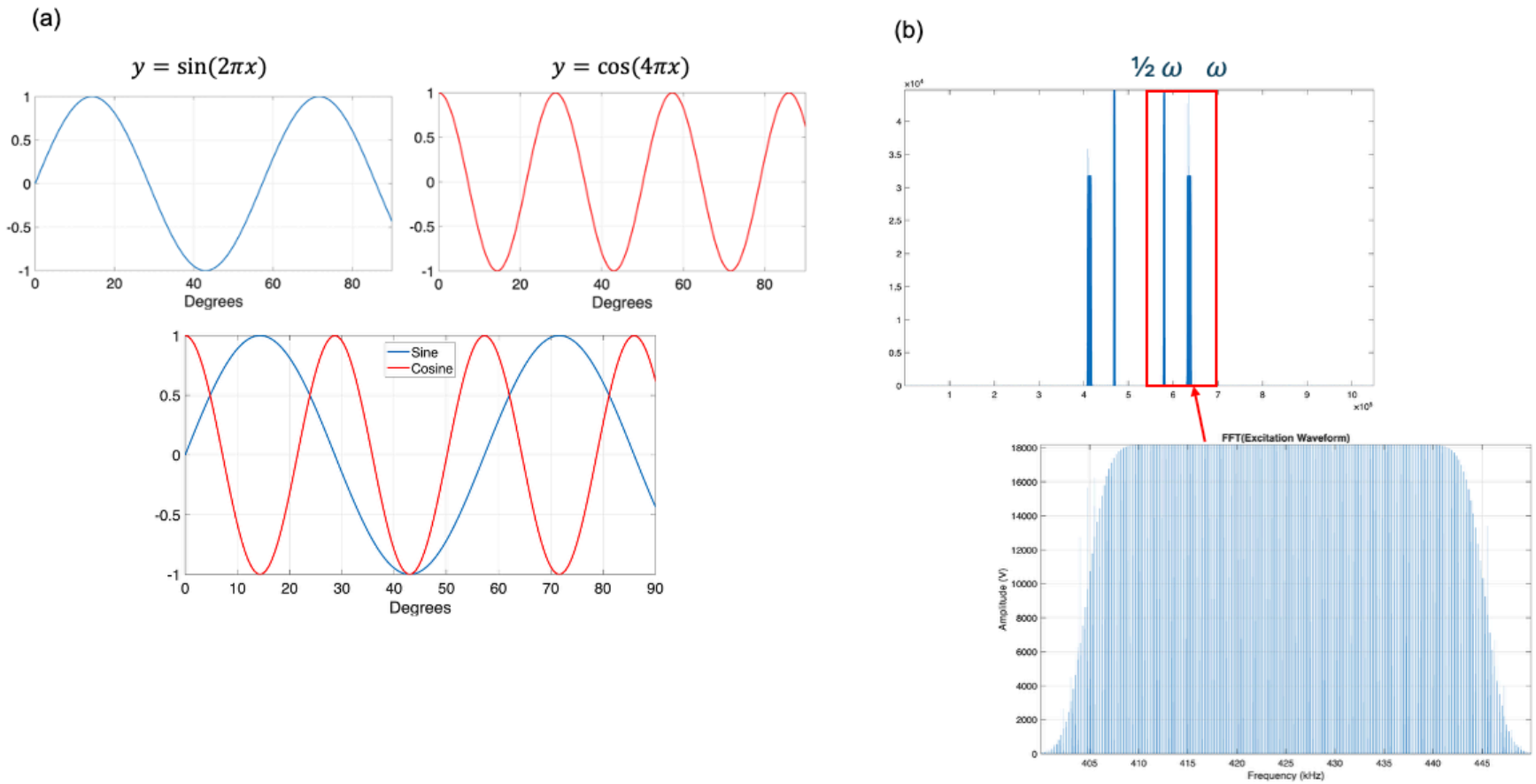


Figure 4.10: (a) A series of plots showing the sine and cosine frequency produced by the first and second harmonic amplitudes. The overlay plot shows a phase difference between the two of 90 degrees. (b) An FFT calculation of the excitation waveform showing the half-resonance and on resonance peaks alongside an inset graph that zooms into on the resonance peak.

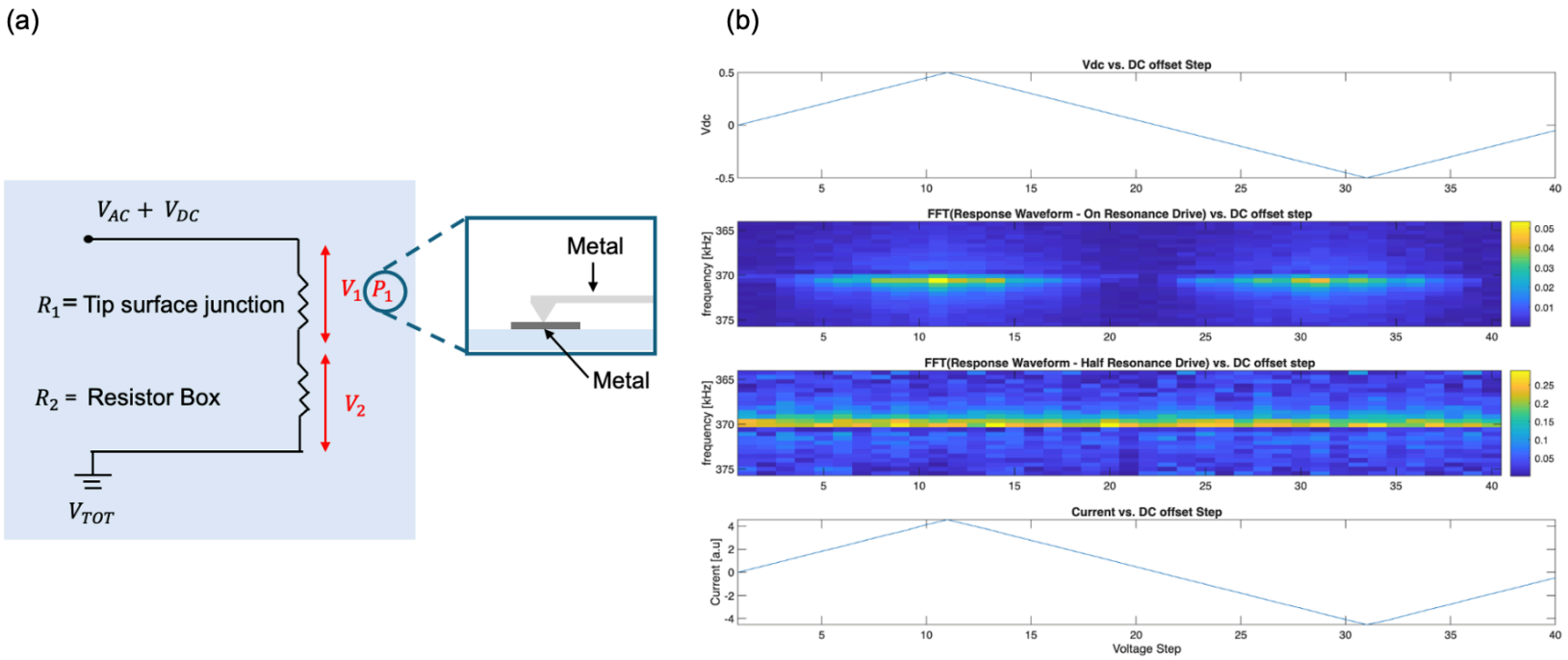


Figure 4.11: (a) A snapshot example of the measurements taken from the half-resonance band excitation experiment for the first case of ohmic resistance, metallic tip and metallic electrode. The top plot feature the DC voltage sent through the tip-surface junction as a function of voltage step. The following 2D maps feature the first harmonic signal (response waveform on resonance drive) and the second harmonic signal (response waveform on half resonance drive) as a function of frequency and voltage step. The color bar for these maps indicates the magnitude of amplitude measured. The bottom plot shows the current measured as a function of voltage step. (b) A schematic of the experiment set-up highlighting the circuit of interest, showing where the joule heating (P_1) is being measured for at the tip-surface junction.

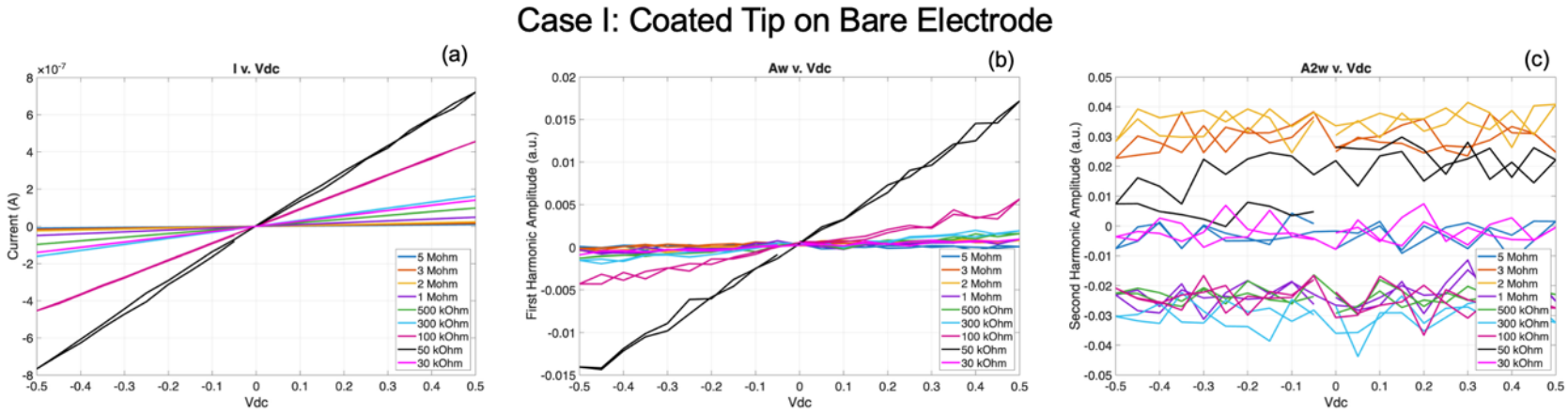


Figure 4.12: The following plots demonstrate the relationships found in half-resonance band excitation of a coated AFM tip on nickel electrode for each respective resistor box resistance: (a) current (I) and DC voltage (Vdc), (b) first-harmonic amplitude (Aw) and Vdc, (c) second-harmonic amplitude (A2w) and Vdc,

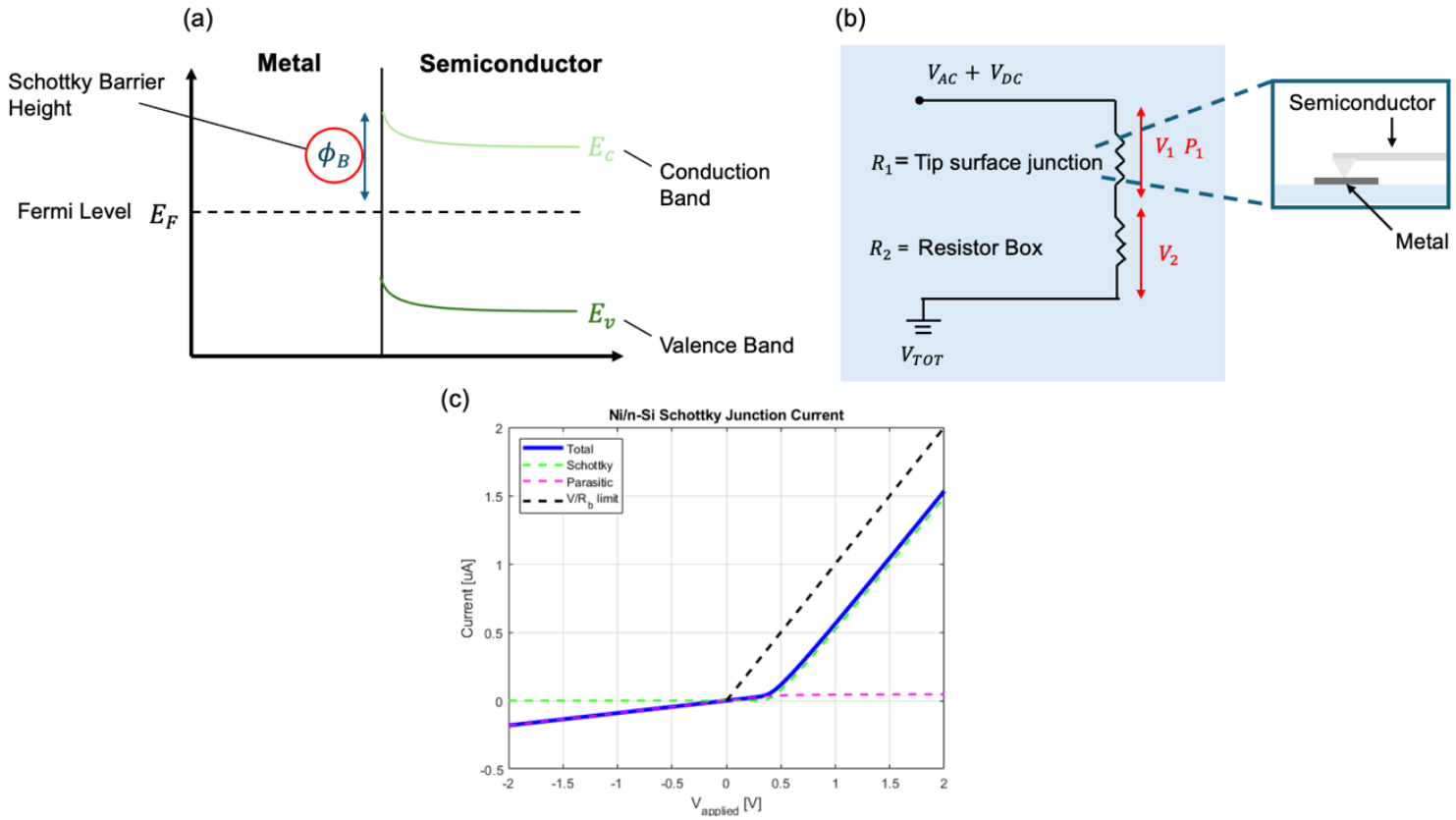


Figure 4.13: (a) A schematic showing a Schottky barrier formed between a metal and semiconductor. (b) A drawing of the circuit formed in the experiments for each environment, showing the tip acting as a semicondcutor and electrode acting as the metal for the Schottky junction environment. (c) A plot of the physics model for a Ni/n-Si Schottky junction used to help interpret results recorded from the AFM experiments.

Table 4.2: Parameters for Schottky Barrier Physics Model

Constants	**Geometric Parameters**	**Material Parameters**	**Resistance Parameters**
Effective Richardson constant (A^*) = 1.12×10^6 A/(m²·K²) for n-Si	Contact diameter (d) = 50-200 nm	Schottky Barrier height (φ_B) = 0.67 eV for Ni/n-Si	Series resistance R_b = 10^5-10^7 Ω
Boltzmann constant (k_B) = 1.381×10^{-23} J/K	Contact area (A) = 2×10^{-15} to 3×10^{-14} m²	Ideality factor (n) = 1.05-1.2 typical for high doping	Parasitic resistance R_p = 10^7-10^{10} Ω
Elementary charge (q) = 1.602×10^{-19} C		Absolute Temperature = 300 k for room temperature	

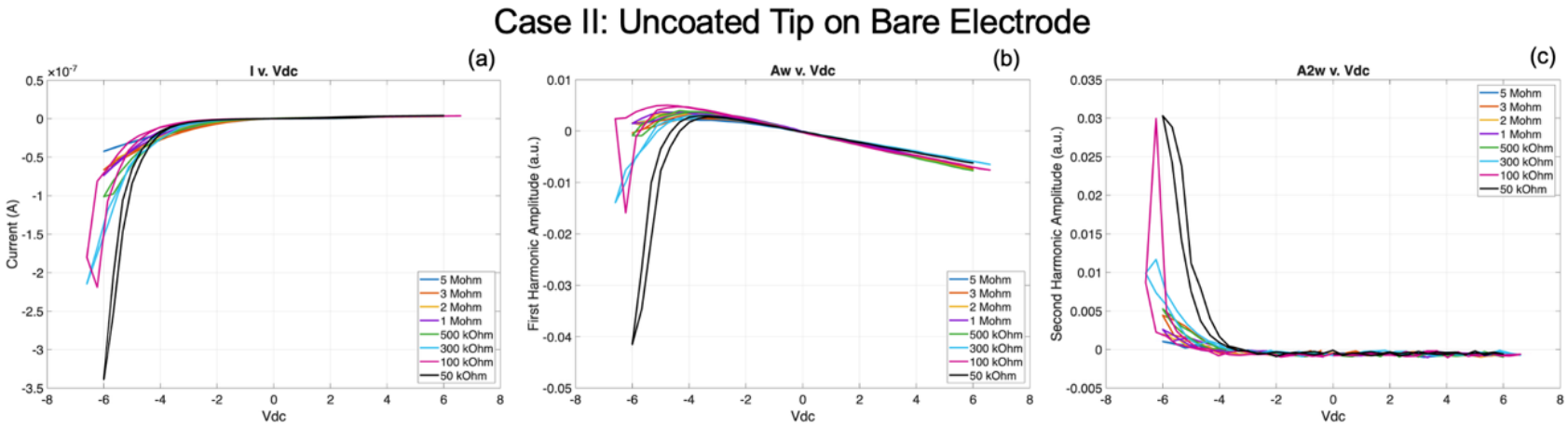


Figure 4.14: The following plots demonstrate the relationships found in half-resonance band excitation of an ucoated AFM tip on nickel electrode for each respective resistor box resistance: (a) current (I) and DC voltage (Vdc), (b) first-harmonic amplitude (Aw) as a function of Vdc, (c) second-harmonic amplitude (A2w) as a function of Vdc.

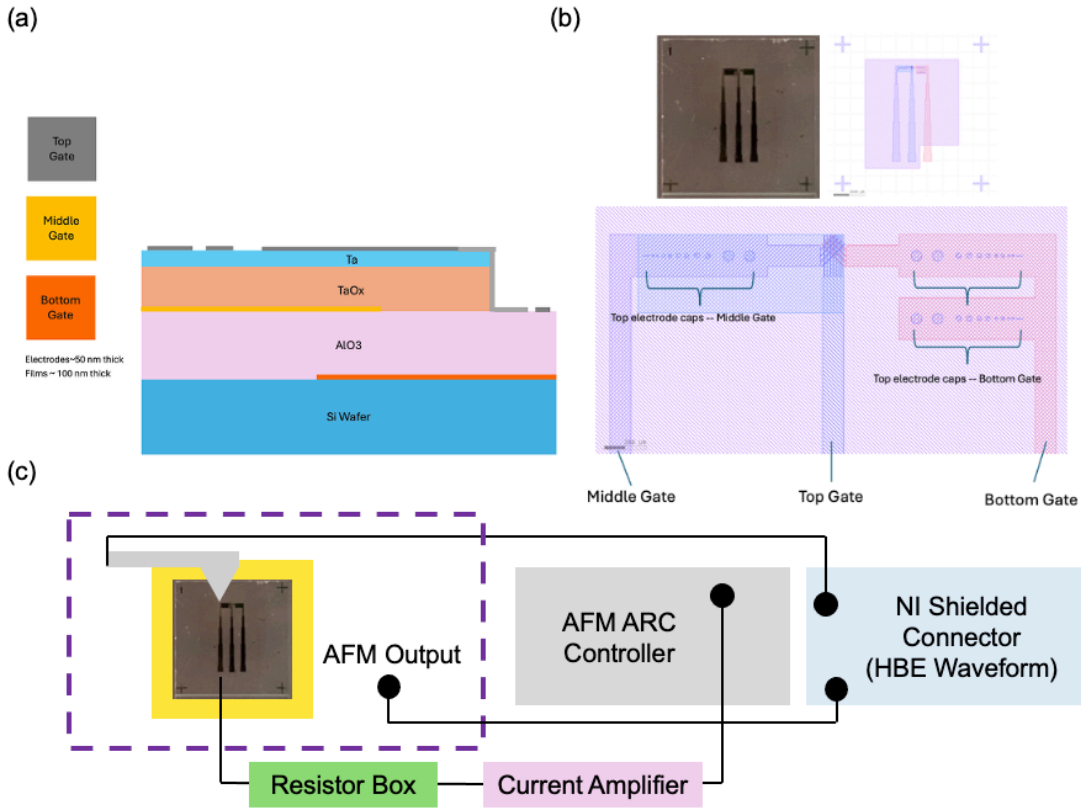


Figure 4.15: (a) A schematic of the sample stack used for AFM experiments – coated tip on bare electrode, uncoated tip on bare electrode, and coated tip on cap on TaOx. (b) A schematic showing a top-down view of the sample. The bare electrode measurements were taken on the top gate region. The TaOx measurements were located on the top electrode caps in the middle gate region, where only TaOx could be accessed. (c) A diagram of experimental setup for the TaOx case showing the components of the resistor box, AFM controller, and source of HBE waveform. For other cases, the setup is the same, however the outgoing line to the resistor box is connected to the top gate instead of the middle gate.

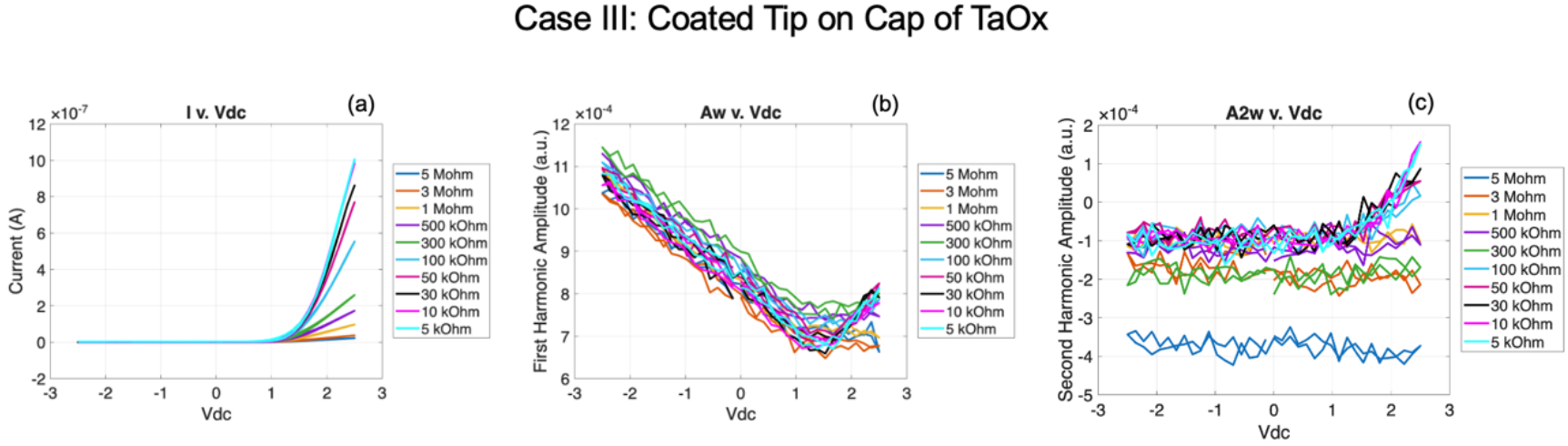


Figure 4.16: The following plots demonstrate the relationships found in half-resonance band excitation of a coated AFM tip on nickel cap of tantalum oxide (TaOx) for each respective resistor box resistance: (a) current (I) and DC voltage (Vdc), (b) first-harmonic amplitude (Aw) as a function of Vdc, (c) second-harmonic amplitude (A2w) as a function of Vdc,

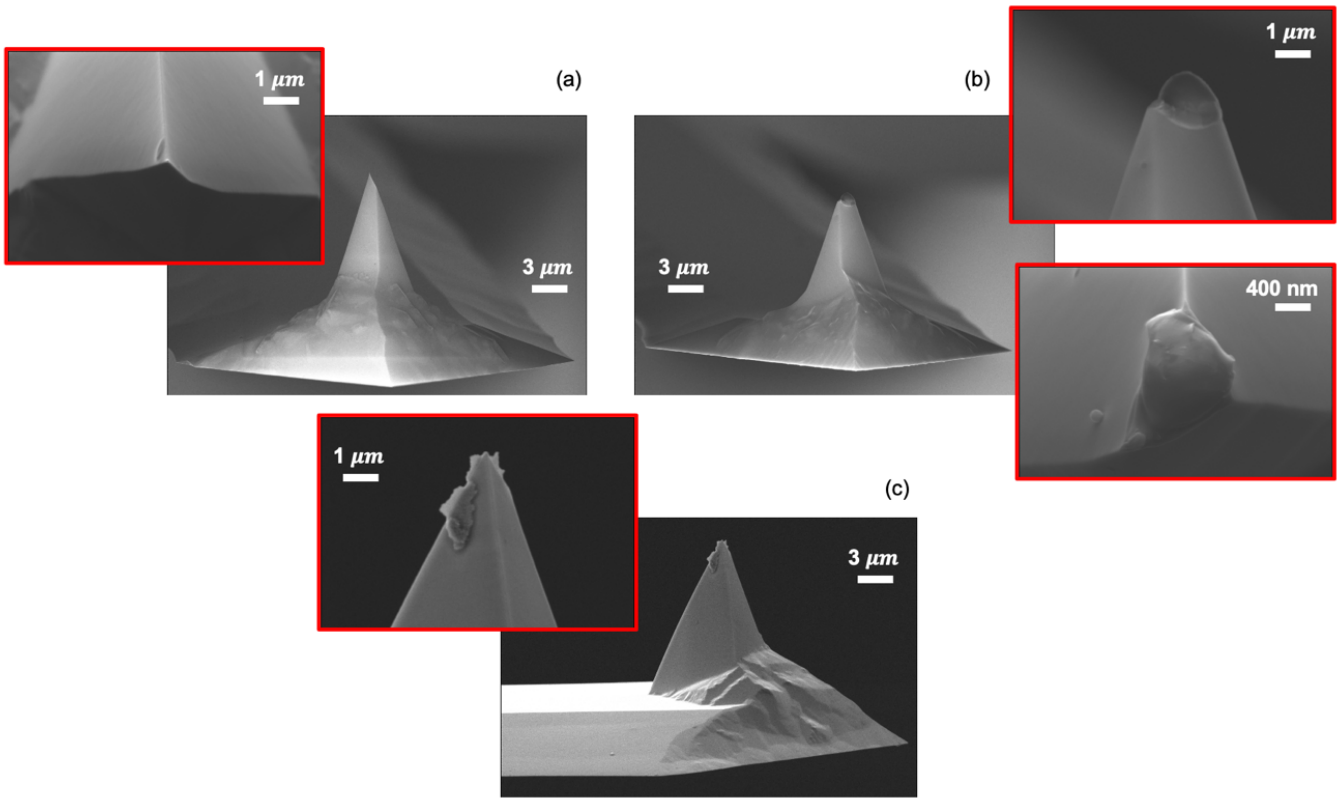


Figure 4.17: A series of SEM images that qualitatively show alterations to the AFM tip after measurements. (a) Pt AFM tip on bare electrode (b) Uncoated Si tip on bare electrode (c) Pt AFM on cap of TaOx.

VITA

Holland Hysmith Swicegood graduated in 2019 with her B.S. in Chemical Engineering from Tennessee Technological University with a Distinction of the Major in undergraduate research. Prior to her graduate education, she embarked on many internships to further develop her passion for science. She participated in the Higher Education Research Experience (HERE) and Science Undergraduate Laboratory Internship (SULI) programs at Oak Ridge National Laboratory to expand her background in the materials science sphere. Additionally, she completed a Research Undergraduate Internship (REU) at Penn State University in their Chemistry and Materials Science departments. In Fall of 2020, she began her graduate education at the University of Tennessee Knoxville to obtain a Ph.D. in Energy Science and Engineering from the UT-ORII program, partnered with Oak Ridge National Laboratory. Holland resides in the Knoxville area with her husband Dallas and two cats, Opal and Shar.